Air quality estimations at local scale accounting for indoor and outdoor pollutants emissions

Yunyi Wang

École des Ponts
ParisTech

THÈSE DE DOCTORAT
de l'École des Ponts ParisTech

Estimations de la qualité de l'air à l'échelle locale en tenant compte des émissions de polluants intérieurs et extérieurs

École doctorale N°531, Ecole Doctorale - Sciences, Ingénierie et Environnement (SIE)

Sciences et Techniques de l'Environnement

Thèse préparée au sein du laboratoire CEREA

Thèse soutenue le 30 Mai, 2023, par
Yunyi WANG

Composition du jury:

Isabelle Calmet Professeur, École Centrale de Nantes	*Rapporteur*
Jean-François Léon Chargé de recherche, Université Paul Sabatier Toulouse III	*Rapporteur*
Yongfeng Qu Maître de conférences, Centre Borelli	*Examinateur*
Henri Wortham Professeur, Université d'Aix-Marseille	*Examinateur*
Karine Sartelet Directrice de recherche, CEREA ENPC	*Directrice de thèse*
Cédric Flageul Maître de conférences, Institut Pprime, Université de Poitiers	*Co-directeur de thèse*
Arièle Deffosez Ingénieure de recherche, EDF–R&D/MFEE	*Co-encadrante de thèse*

ABSTRACT

As many people are exposed to high concentrations of air pollutants in urban areas, it is important to understand the sources and formation processes. Modeling is an effective tool for this. This thesis focuses on understanding the physical and chemical processes influencing indoor and outdoor air quality at the local scale through modeling.

In a first step, the air quality in an urban street is modeled with the computational fluid dynamics (CFD) tool code_saturne, coupled with the atmospheric chemistry and aerosol dynamics module SSH-aerosol. The canyon street is modeled in 2D, and the study covers a period of 12 hours. The simulated NO_2 and PM_{10} concentrations compare well with experimental measurements when atmospheric chemistry and aerosol dynamics are taken into account. However, the concentration of black carbon is underestimated, probably partly due to the underestimation of non-exhaust emissions. The concentrations of secondary PM compounds are strongly influenced by aerosol dynamics. In particular, ammonia emitted by traffic promotes the formation of inorganic and hydrophilic organic particles.

In a second step, to study the impact of trees in the street, trees are added to the 2D street canyon. The aerodynamic impact of the tree crowns significantly increases the concentration of pollutants emitted by traffic. Dry deposition on leaf surfaces is only significant for highly soluble compounds such as HNO_3 or low volatile compounds. Emissions of volatile organic compounds (VOCs) from trees have little influence on the formation of condensables, except in the case of low wind. Nevertheless, the production of some extremely low volatile organic compounds by autoxidation is high, which could favor the formation of ultrafine particles.

Finally, the indoor air quality in a closed stadium is studied using a 0D model (H^2I). The indoor-outdoor exchange rate and the filtration factor of the model are determined from the measured indoor and outdoor black carbon concentrations using a Fourier transformation. The temporal variations of O_3 and NOx concentrations in indoor air are correctly simulated, but NO concentrations are overestimated and NO_2 and O_3 concentrations are underestimated. Sensitivity tests are carried out to determine the relevant physical parameters of the model that drive these concentrations. The impact of surface reactions is limited, as the ratio of surface area to stadium volume is low compared to smaller indoor environments. The inclusion of VOCs favors the conversion of NO to NO_2 and reduces the underestimation of NO_2. Photolysis also has a strong influence on concentrations, with a

strong impact of glazing.

Keywords: *Air quality*, *CFD modeling*, *Indoor and outdoor*, *Secondary aerosol*, *Local scale*.

RÉSUMÉ

De nombreuses personnes étant exposées à de fortes concentrations de polluants atmosphériques en milieu urbain, il est important d'en comprendre les sources et les processus de formation. La modélisation est un outil efficace pour cela. Cette thèse porte sur la compréhension par modélisation des processus physiques et chimiques influençant la qualité de l'air intérieur et extérieur à l'échelle locale. Dans un premier temps, la qualité de l'air dans une rue urbaine est modélisée avec l'outil de mécanique des fluides numérique (CFD) code_saturne, couplé au module de chimie atmosphérique et de dynamique des aérosols SSH-aerosol. La rue canyon est modélisée en 2D, et l'étude porte sur une période de 12 heures. Les concentrations simulées de NO_2 et de PM_{10} se comparent bien aux mesures expérimentales lorsque la chimie atmosphérique et la dynamique des aérosols sont prises en compte. Cependant, la concentration de carbone suie est sous-estimée, probablement en partie à cause de la sous-estimation des émissions hors échappement. Les concentrations des composés secondaires des particules sont fortement influencées par la dynamique des aérosols. Notamment, l'ammoniac émis par le trafic favorise la formation de particules inorganiques et organiques hydrophiles. Dans un second temps, pour étudier l'impact des arbres dans la rue, des arbres sont ajoutés dans la rue canyon 2D. L'impact aérodynamique des couronnes d'arbres augmente significativement la concentration des polluants émis par le trafic. Le dépôt sec sur les surfaces des feuilles n'est important que pour les composés très solubles comme HNO_3 ou peu volatils. Les émissions de composés organiques volatils (COV) par les arbres influencent peu la formation des condensables, sauf en cas de vent faible. Néanmoins, la production de certains composés organiques extrêmement peu volatils par autoxidation est élevée, ce qui pourrait favoriser la formation de particules ultrafines. Finalement, la qualité de l'air intérieur dans un stade fermé est étudiée à l'aide d'un modèle 0D (H^2I). Le taux d'échange intérieur-extérieur et le facteur de filtration du modèle sont déterminés à partir des concentrations de carbone suie mesurées à l'intérieur et à l'extérieur en utilisant une transformation de Fourier. Les variations temporelles des concentrations d'O_3 et de NOx en air intérieur sont correctement simulées, mais les concentrations de NO sont sur-estimées et celles d'O_3 de NO_2 sous-estimées. Des tests de sensibilité sont effectués afin de déterminer les paramètres physiques prégnants du modèle qui pilotent ces concentrations. L'impact des réactions de surface est limité, car le ratio entre la surface et le volume du stade est faible comparé à des environnements intérieurs plus petits. La prise en compte des COV favorise la conversion du NO en NO_2 et réduit la sous-estimation du NO_2. La photolyse

influence aussi fortement les concentrations, avec un fort impact du vitrage.

Mots clés: *Qualité de l'air*, *Modélisation CFD*, *Intérieur et extérieur*, *Aérosol secondaire*, *Échelle locale*.

TABLE OF CONTENTS

CHAPTER 1

Introduction

1.1 Context of the PhD thesis

With the rapid pace of global urbanization and industrialization, environmental problems is becoming an important issue, receiving wide attention from all sectors. Urban air quality, relying on which urban citizens live, has always been essential for their impacts on human health and the quality of life. The reasons for the increasing attention for urban air quality problems in recent years are based on the following factors.

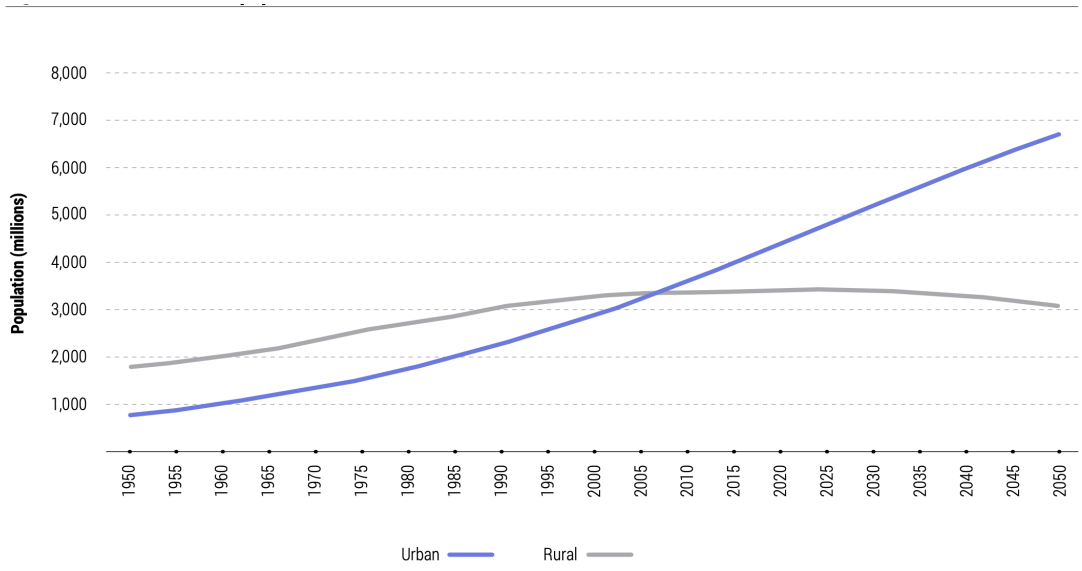

Fig. 1.1 Evolution and prediction of urban population and rural population from the year of 1950 to 2030. Source: (UN-Habitat 2022).

First of all is the explosion of urban population. The evolution of global urban and rural population is presented in Fig 1.1. From the year of 1950, the growth rate of urban population is always higher than rural population. Before 2005, global rural population was higher than urban population, at the same time, the rural population reached the highest around the year of 2005. However, since 2007, the rural population remains almost unchanged and it is estimated to decrease from 2030. In contrast, urban population keeps increasing with a high pace during the past 15 years and the high increasing rate is estimated keeping unchanged in the next 30 years. Therefore, the gap between urban and

rural populations is expected to grow. According to the World Cities Report 2022 by the United Nations Human Settlement Programme, global urbanization is advancing at a rapid pace, with an estimated 2.2 billion people expected to be added to the urban population by 2050, the global urban population will account for 68% of the world's population (UN-Habitat 2022). Corresponding to the high urban population growth, although the expansion of urban spatial space is fast, the global urban population density keeps increasing, particularly in low-income countries (UN-Habitat 2022). As one of the major components affecting the climate change (Dodman 2009), the increasing global urban population density has brought the awareness to the importance of urban air quality problems.

Secondly, the rising living standards of urban residents brings new challenges to the urban air quality. The environment is altered with human activities. In large urban areas, complex urban landscapes including high-rise buildings, roads, green spaces, and concrete surfaces exacerbate the potential for air pollution and extreme weather (Han et al. 2015, Qian et al. 2022). Recent years, due to the improvement of people's life quality, the ownership of private cars is increasing. From the modeling of global vehicle saturation over 45 countries by Dargay et al. (2007), the vehicle stock in the year of 2030 is expected to be over 2 billion, which is about 2.5 times more than at the beginning of the 21^{st} century. The impact of vehicle ownership is demonstrated to have a higher mediating impact on the air pollution among the urbanization process and vehicle exhaust emissions have been widely proven as one of the main pollutant sources (Tao et al. 2021). Besides of the vehicles, other anthropogenic activities which related to the urban residents' daily life such as the use of fossil fuels, the power generations and the industrialization also contribute to the urban air pollution (Fenger 1999), making the urban air quality an important issue for sustainable cities.

A key to evaluate the impact of human activities on the urban air quality lies on the understanding of the relative importance of different physical and chemical processes in the atmosphere (Zifa et al. 2008, Friedlander 1973, Song et al. 2019). As an important tool connecting the theoretical and experimental research, numerical modeling are essential for studying indoor and outdoor air quality in cities. Different urban environmental factors including the pollutant emissions, the meteorological parameters, urban geomorphological features can be modeled with different complexity to reproduce and predict the urban air quality and to build a comprehensive understanding of air pollution (Yassin 2013, He et al. 2013, 2016, Liu and Leung 2008). Therefore, the reproduction of concentrations of different pollutants and the related sources and processes for their formation in indoor and outdoor atmosphere in urban areas through simulation methods is the research focus in this thesis.

1.2 Urban air quality problem

Pollution is often seen as a side product of urban development that threatens human health. The World Health Organization has reported that about 93% of the children in the world have to breathe toxic air every day (Organization et al. 2018). In this section, the main urban air pollutants and their sources, the impact to human health and to the urban environment are presented.

1.2.1 Main composition of urban air pollutants

High concentrations of sulfur dioxide (SO_2), nitrogen dioxide (NO_2), ozone (O_3), and particulate matters (PM) are observed in urban atmosphere (Zabalza et al. 2007). Some of the atmospheric components are emitted directly from different sources in the atmosphere, which are called primary pollutants, while the others are formed in the atmosphere from the gas precursors via chemical reactions, named secondary pollutants.

Among the gaseous pollutants, primary gaseous pollutants, such as SO_2, CO, NOx, and some volatile organic compounds (VOC) are emitted by various sources. Power plants, industry, domestic heating, and vehicles are the main sources for these pollutants in urban areas (Lin et al. 2011), most of which are anthropogenic sources from human activities. Secondary gaseous pollutants, such as NO_2 and O_3 are formed through physical and chemical processes. The precursors of O_3 include NOx, CO and VOCs (Seigneur 2019). As the main gaseous composition in photochemical smog, O_3 is largely produced by photochemical reactions and therefore, the concentration of O_3 is high in spring and summer (Muilwijk et al. 2016). However, a secondary pollutant can at the same time be a primary pollutant, such as NO_2. For NO_2 in urban streets, about 10% on average of its concentration is from primary traffic exhaust, the rest are formed from chemical reactions (Carslaw and Beevers 2005).

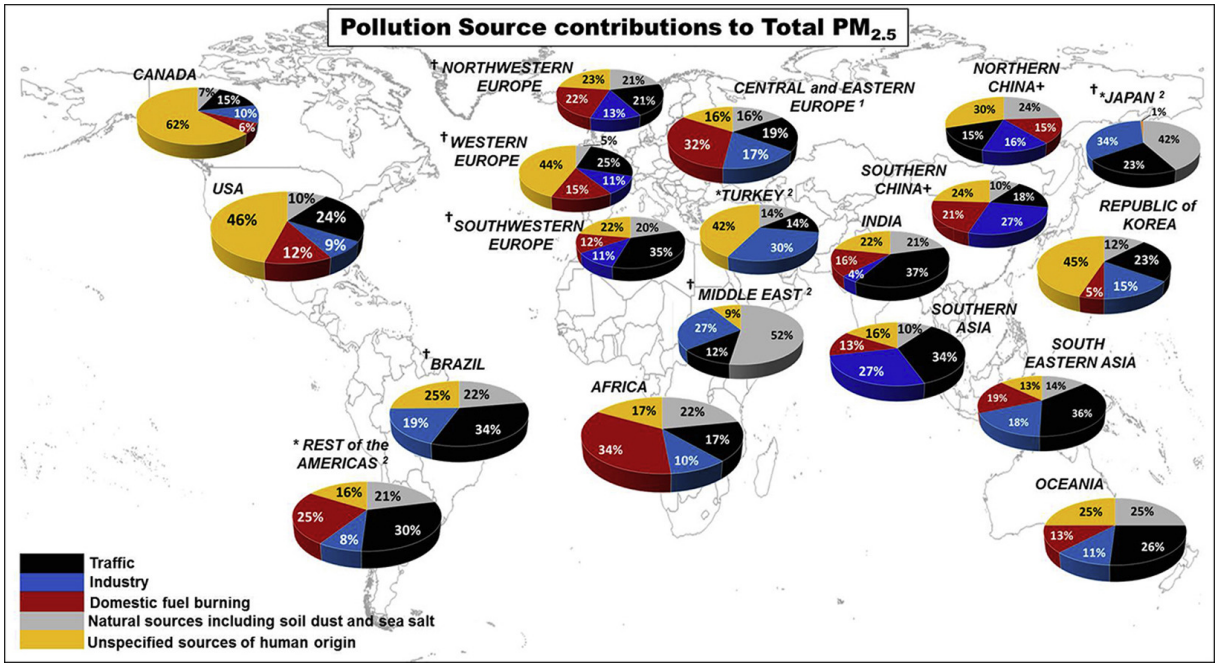

Fig. 1.2 Local source contributions to $PM_{2.5}$ for different cities at global level. Source: (Karagulian et al. 2015).

Considering particulate matters (PM), different PMs show notable distinctions in properties such as particle size, chemical composition and morphology. The size of the particles vary largely, with the diameter of the particle (Crowder et al. 2002) ranging from several nanometers (nm) to several micrometers (μm). According to the definition, ultrafine particles refer to those with particle diameters less than 100 nm. Fine particles have an aerodynamic diameter less than 2.5 μm ($PM_{2.5}$). Particles

with larger diameters are so-called coarse particles. PM_{10} includes both fine particles and coarse particles (Seigneur 2019). The primary compounds of particles includes those from dust and unspecified matter, those from the incomplete combustion of carbon, sea salt particles and some semi or low volatile organic matters (Curtius 2009). Secondary compounds of particles are those formed in the atmosphere from gaseous precursors and through the gas-phase chemistry and aerosol dynamics. For example, NOx, SO_2, VOC, and SVOC are important precursors of secondary fine particles (Seigneur 2019).

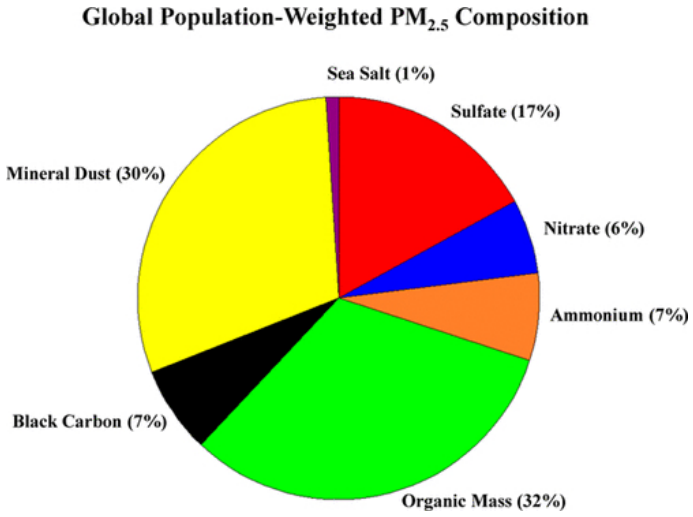

(a) Global population weighted $PM_{2.5}$ composition

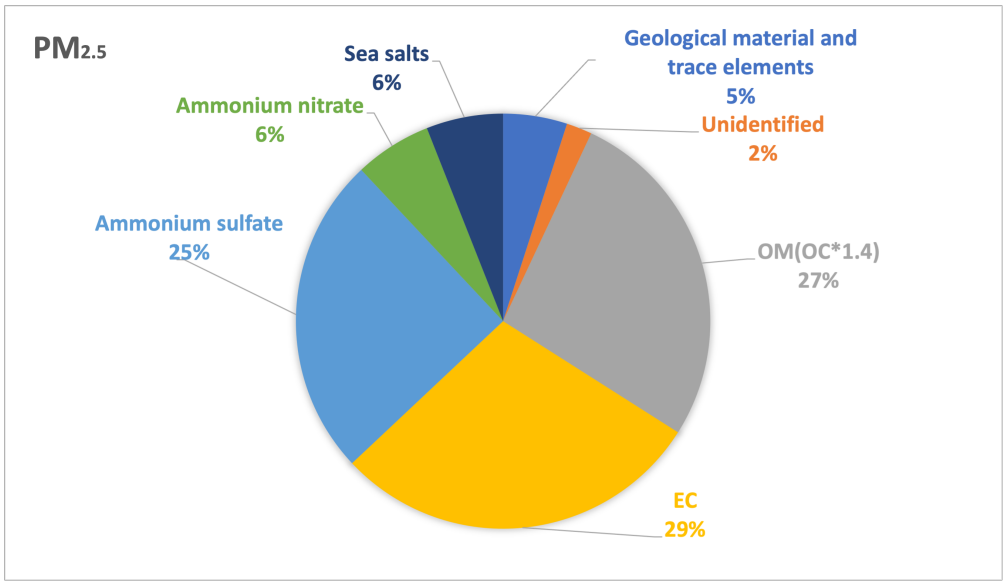

(b) $PM_{2.5}$ composition near a roadway in Hongkong

Fig. 1.3 Comparison between global population weighted $PM_{2.5}$ composition and urban PM composition near a roadway. Source: (a) (Philip et al. 2014), (b) (Cheng et al. 2015).

PM compositions vary significantly due to a diversity of sources from different areas. Fig 1.2 presents the local source contribution to the concentration of $PM_{2.5}$ in different cities of the world. Globally, 25% of the urban $PM_{2.5}$ concentration comes from traffic emissions; 15% from industry; 20% from domestic heating; 22% from unspecified human activities; and 18% from natural sources.

For most of the cities, the anthropogenic sources have higher contribution to PM2.5 mass and number concentrations than natural sources. However, the fraction differs largely in different countries. For example, the traffic is the main contributor to urban $PM_{2.5}$ in several cities in south Asia, southwestern Europe and south America. Nevertheless, this is not the case in cities in Middle East, northern China and Canada. The diversity of sources leads to different PM composition. Panels (a) and (b) in Fig 1.3 present the global population-weighted $PM_{2.5}$ composition and the PM composition near a roadway in a city. The comparison between two panels shows a significant increase in sulfate and Black carbon (EC in panel (b)) near the roadway, where traffic emissions are the main contributor to the $PM_{2.5}$. The PM composition in streets and their formation are discussed in details in Chapter 2.

1.2.2 Impact of air pollution on human health

The air pollution is a severe problem in many areas of the world. It is reported that nine-tenth of the world's population is being exposed to polluted air (Osseiran and Lindmeier 2018). In 2016, 4.2 million deaths were related to ambient air pollution, alongside with 3.8 million deaths caused by indoor air pollution during the same period (Osseiran and Lindmeier 2018). In recent years, although the deaths from indoor air quality are reduced, they are offset by the increasing deaths from ambient air pollution (Fuller et al. 2022). Air pollution remains responsible for about 9 million deaths every year, especially in low- and middle-income countries.

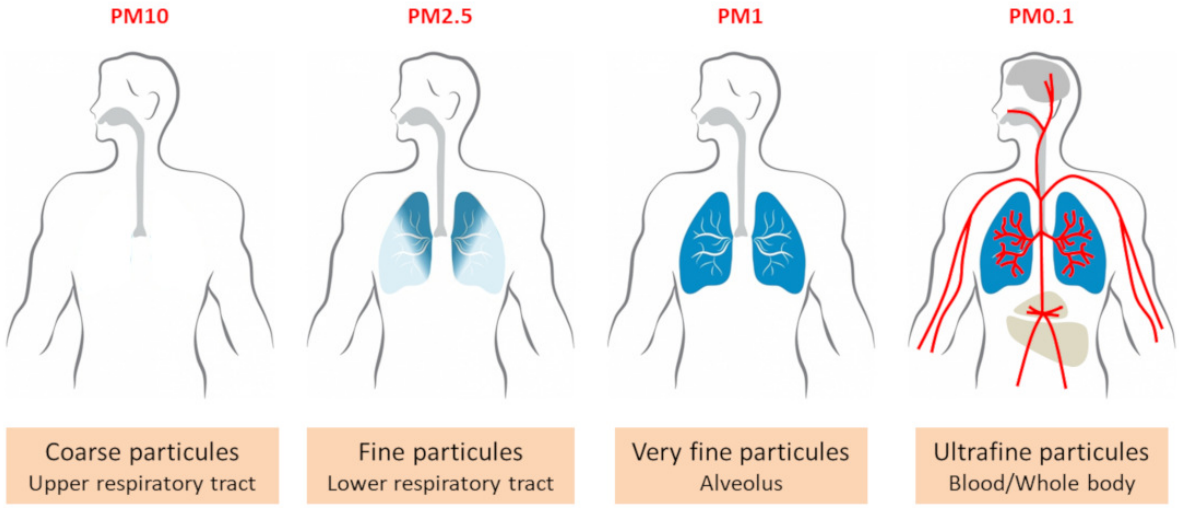

Fig. 1.4 Lung penetration of particles. Source: The Encyclopedia of the Environment (Danel 2019)

The atmospheric pollutants that have the greatest impact on human health are PM_{10} and $PM_{2.5}$ (Uzu et al. 2011). The particle diameters determine whether and how they can enter the body (Vincent 2019). Fig 1.4 presents the lung penetration of particles with different diameters. It can been seen that only particles with diameters smaller than 2.5 μm (fine particles) can reach the lungs and the alveoli of the lungs. Ultrafine PM with diameters less than 100 nm are able to cross the alveolar capillary membranes into the blood, and pass through the whole body. In addition to the respiratory pathway

through the bronchopulmonary system, PM can also penetrate the body through the digestive and dermal pathways (Vincent 2019).

Because of the lung penetration of particles, they have significant impacts on lungs. Various studies have demonstrated the association between $PM_{2.5}$ exposure and lung and asthma diseases, lung function and lung development (Tecer et al. 2008, Li et al. 2018, Liu et al. 2022). The carcinogenicity of PM and other pollutants was confirmed by the International Agency for Research on Cancer (IARC) (Loomis et al. 2013). Besides of the impact on lungs, as is described in the previous paragraph, ultrafine PM can penetrate through the whole body and even reach to the brain, which may also lead to various cardiovascular system diseases and neurological diseases (Zheng et al. 2015).

1.2.3 Impact of air pollution on the environment

While the air pollution has the most imperative impact on human health, it also damages our environment. The impact of air pollution on the environment involves the impact on climate change, ecosystems, buildings and cultural heritage.

Considering the climate change, some particles such as black carbon can absorb solar radiation. This results in less sunlight to be reflected back into space, and thus contributes to the greenhouse effect and the increase of temperature (Jacobson and Turco 1995, Wickramasinghe et al. 1989). This effect also has a cascading impact on the vegetation growth, leading to a further increase in global warming (Cline 1991). However, not all particles favors the global warming, depending on its composition. Generally, inorganic particles such as sulfates and nitrates lead to more reflections of sunlight into the universe and cooling the temperature. Particles such as black carbon have reverse impact as is shown before. Higher temperature can affect the wavelength and intensity of the heat (Garrett et al. 2002), which may also promote the photochemical formation of O_3.

Air pollution also influences the ecosystem (Lovett et al. 2009, Greaver et al. 2012). Gaseous pollutants of NOx and SO_2 are two major precursors of acid rain (Parungo et al. 1987). The deposition of sulfur and nitrogen leads to the acidification and the eutrophication of water and soil (Dentener et al. 2006, Qiao et al. 2015). The continuous acidification of soils results in the loss of salt-based ion, the free up of harmful metal ions, and thus the decline of forest (Dai-Zhang et al. 2003). The free metal ions from acidified soils move with water and enter lakes and rivers, together with the acidification of water, damages aquatic plants and animals. In addition, gaseous and particulate pollutions are able to penetrate into the plant through the leaves and generate free radicals (hydroxyl radicals) and reactive oxygen species (ROS) to induce oxidative stress reactions, which may damage the lipids, proteins and nucleic acids of plants, thus limiting their growth (Foyer and Harbinson 2019, Aranjuelo et al. 2008, Rai 2016).

In addition, atmospheric pollution injures buildings and cultural heritage. The pollution of acid rain, dust, SO_2 and O_3 are the major causes of the heritage damage (Sesana et al. 2021). Cultural relics constructed by marbles are more vulnerable to acid rain. The calcium carbonate ($CaCO_3$) in marble reacts with acid rain containing SO_2 and forms calcium sulfate ($CaSO_4$). $CaSO_4$ can deposit

on the surface of marble and gradually fall off, causing damages to the surface of stones (Schuster et al. 1994, Cheng et al. 1987). Particles also impact the corrosion of cultural heritage. The main water-soluble inorganic ions in $PM_{2.5}$ are SO_4^{2-}, NO_3^- and NH_4^+. These ions exist in the form of NH_4NO_3 and $(NH4)_2SO_4$, leading to a weakly acidic environment on metal surfaces (Wang et al. 2013). Depending on the physical and chemical properties of different PM, it is possible to accelerate the corrosion of metals (García et al. 2007). Paintings, sculptures, buildings, and other surfaces containing metal elements subject to corrosion by PM.

1.3 Physical and chemical processes in indoor and outdoor urban environment

Pollutants in the atmosphere interact with different components including other pollutants, water, soil, vegetation, etc. and undergo physical and chemical transformations. It is important to understand these different processes, in order to correctly reproduce the evolution of air pollutants in indoor and outdoor environment and to provide guidance to improve the urban air quality. In this section, main processes in ambient and indoor atmosphere in local scales are presented.

1.3.1 Physical processes

Atmospheric dispersion is an important process for pollutants in the air. It refers to the process in which pollutants disperse and dilutes under the mixing effect of turbulence that occurs within the air near the ground surface (Stockie 2011). Atmospheric dispersion of pollutants is impacted mainly by the wind direction, the wind speed, the temperature and the atmospheric stability.

Due to the chaotic character of the flow, the turbulence exists in the form of vortex with different size scales. The scale of macroscopic vortices is much larger than the mean free path of molecules. Prandtl proposed the mixing length model to describe the characteristic size of the vortex (Holton 2004). While it is impossible to determine the turbulence in mathematics (Seigneur 2019), approximations are made for the representation of turbulence. Turbulent processes can be described through lagrangian approach or eulerian approach (Gouesbet and Berlemont 1999). The lagrangian approach uses a reference system moving with the mean wind. The turbulent diffusion is relative to the reference system. While in eulerian approach, the reference system is fixed. The turbulent diffusion is the absolute diffusion.

Atmospheric deposition refers the process of pollutants in the atmosphere deposited onto the solid or liquid surfaces through different pathways. It can be divided into dry deposition and wet deposition. In this thesis, atmospheric dry deposition is focused, which refers to the removal of gaseous and particulate species by different processes in absence of precipitation (Farmer et al. 2021). Pollutants are transported to the surfaces of vegetation and buildings, and are adhered to the surface because of the molecular forces.

The deposition impact is often measured by the deposition velocity, which is defined as the ratio of the deposition flux (F) on a unit area per unit time to the air concentration. Considering the deposition of particles, for particles with diameters larger than 10 μm, gravitational settling dominates. On the oppposite, for particles with diameters smaller than 1 μm, the dry deposition are mainly due to the turbulent transfer and Brownian diffusion (Zhang et al. 2001), and the gravitational settling can be neglected.

The dry deposition velocity are parameterized in a variety of studies. Wesely (2007), Zhang et al. (2002a, 2003a) parameterized the deposition velocity for gaseous species as the inverse of the sum of resistances, which related to aerodynamic effect, the impact of molecular diffusivity of pollutants and the surface impact. Slinn (1982) developed a deposition model of aerosols for vegetation canopies, taking into account the deposition processes of gravitational settling, impaction, interception, Brownian diffusion and particle rebound. Based on this model, Zhang et al. (2001) optimised the calculation of deposition velocity for aerosols by simplifying the empirical parameterization of all deposition processes.

Occupied Space	Outdoor Air Ventilation Requirement (L/sec/person)				
	1973 version		1981 version		1989 version
	minimum	recommended	non-smoking	smoking	ventilation rate
Dance venues	7.5	10–13	3.5	18	12.5
Bars	15.0	18–20	5.0	25	15.0
Beauty shops	12.5	15–18	10.0	18	12.5
Classrooms	5.0	5–8	2.5	13	7.5
Dining areas	5.0	8–10	3.5	18	10.0
Hospital patient rooms	5.0	8–10	3.5	18	12.5
Conference rooms	10–13	13–20	3.5	18	10.0
Offices	7.5	8–13	2.5	10	10.0
Residences	2.5	4–5	5.0	5	0.35 ACH
Retail stores	3.5	5–8	2.5	13	1.0–1.5L/sec/m^2
Smoking lounges	–	–	–	–	30.0
Spectator areas	10.0	13–15	3.5	18	7.5
Theatres	2.5	3–5	3.5	18	7.5
Transport waiting rooms	7.5	10–13	3.5	18	7.5

Fig. 1.5 Air change standard for different indoor space. Source: (Brown 1997).

Outdoor-to-indoor air exchange rate refers to the rate at which outdoor air replaces indoor air when studying the indoor air quality (IAQ) (Nero 1988). It is defined as the number of times per hour of the total air exchange in an indoor space. Air exchange rate is important for the residents' health.

Insufficient air exchange may cause excessive indoor air pollution such as the accumulation of formaldehyde from indoor equipment (Milner et al. 2014), which is harmful to human health. The confined indoor environment with inadequate outdoor-to-indoor air exchange also results in the high concentration of CO_2, which is not beneficial for human health in long-term, especially for pregnant

women and children (Satish et al. 2012). In addition, a variety of mold, bacteria, viruses and dust mites are easily to be bred in a long-term non-ventilated indoor space. They are attached to furniture, clothes and are able to enter the human body through the respiratory system, resulting in the sickness (Srikanth et al. 2008). Fig 1.5 presents the generic outdoor air ventilation standard for different indoor spaces. In general, indoor spaces with high emissions, with high crowd flow or with high requirements of air quality have a higher air exchange rate than other spaces. The air exchange rate can be adjusted with the equipment of air handlers, together with the filtration of airborne contaminants.

1.3.2 Gas-phase chemistry

In the atmosphere, the gas-phase chemistry can be categorized as photochemical reactions and other chemical reactions (Seigneur 2019).

Photochemical reactions mainly occur in the ozone layer of the atmosphere, where reactants absorb energy from solar radiation and excite electrons, which leads to the breakage and formation of bonds. In urban areas, photochemical smog is currently one of the most concerned pollution issues. The main components of photochemical smog are O_3 and NOx. O_3 is formed through the chemical reactions between NOx and VOCs under the sunlight. The formation of photochemical smog is complex, following a set of photochemical reactions in the atmosphere (Zhong et al. 2014).

Besides of the photochemical reactions, the oxidation of atmospheric components is the major process in the atmosphere, because of the highly oxidizing environment provided by the existence of more than 20% of the oxygen (O_2) in the air (Solazzo et al. 2008). However, because of the relatively stronger chemical stability, O_2 is not the main oxidants in the atmosphere. Instead, O_3, alongside with the hydroxyl radical (OH) and the nitrate radicals NO_3, are the main atmospheric oxidants.

NO_3 is mainly formed through the oxidation of NO_2, and is easily decomposed under the sunlight. O_3 and OH are mainly formed through photochemical reactions. Therefore, in the daytime, OH and O_3 act as the main oxidants, while in the nighttime, NO_3 and O_3 are the main oxidants.

The photochemical formation of O_3 and OH are presented as follows:

1. The photochemical formation of O_3:

$$NO_2 + h\nu \longrightarrow NO + O \tag{1.1}$$

$$O + O_2 + M \longrightarrow O_3 + M \tag{1.2}$$

Where M represents a molecule of N_2

2. The photochemical formation of OH:

$$O_3 + h\nu \longrightarrow O(^1D) + O_2 \tag{1.3}$$

$$O(^1D) + H_2O \longrightarrow OH \tag{1.4}$$

Where $O(^1D)$ represents the excited oxygen atoms.

O_3 can be continuously regenerated through the photolysis of NO_2 in the atmosphere, while at the same time, it is balanced by the consumption as one of the major oxidants. The destruction of O_3 with NO is presented as follows:

$$NO + O_3 \longrightarrow NO_2 + O_2 \tag{1.5}$$

However, the chemical balance between the production and consumption of NOx and O_3 can be interrupted by the addition CO and VOC species. Two chemical regimes are therefore observed according to the possible main oxidation pathways of NOx. As shown in Fig 1.6, in the high-NOx regime, when the fraction [COV]/[NOx] is low, the production of peroxyl radical (RO_2) is limited. NO tends to react with O_3 and therefore results in the destruction of O_3. In contrast, in the low-NOx regime, when the fraction [COV]/[NOx] is high, the production of RO_2 is significant. NO reacts preferentially with RO_2, which favors the formation of O_3. The critical fraction between [COV] and [NOx] identifying the chemical regime has been osberved to be around 8 (ppb C/ppb) (Seinfeld and Pandis 2016).

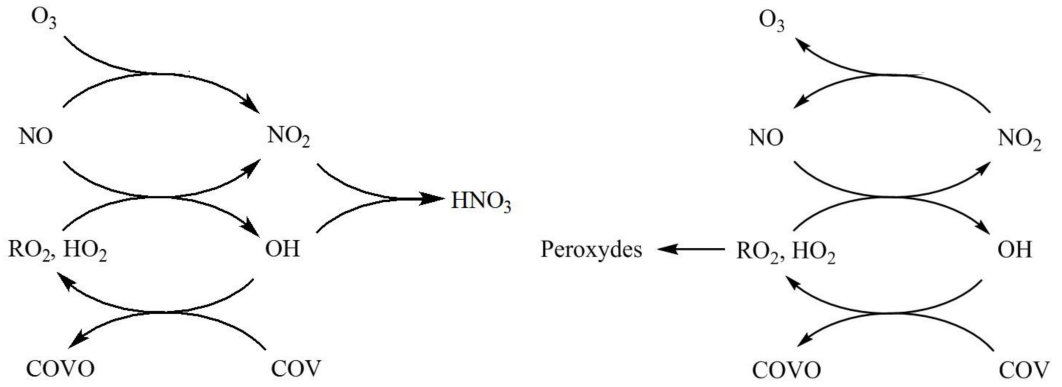

(a) High-NOx regime

(b) Low-NOx regime

Fig. 1.6 Possible NOx oxidation pathways observed in two chemical regimes. Source: Ecole des Ponts/ POLU1 course.

The oxidation of precursor gases in the atmosphere, such as NO_2 and VOCs, impacts the formation of condensables. The formation of these condensables, which may condense onto particles depending on the environment, is detailed in Chapters 2 and 3.

1.3.3 Aerosol dynamics

Aerosols are solid or liquid particles suspended in the atmosphere, ranging in size from a few nanometers to several micrometers. Aerosols are formed naturally from volcanic eruptions, forest fires, dust storms. They are also formed from human activities such as industrial processes, transportation and burning of fossil fuels.

Aerosol dynamics concern how aerosols move, interact, and transform in the atmosphere. It involves the physical, chemical, and biological processes that affect aerosols, such as coagulation,

nucleation, condensation and evaporation. These processes determine the concentration, size distribution, and chemical composition of aerosols in the atmosphere, which in turn influence air quality, climate, and human health.

1.3.3.1 Nucleation

Nucleation is the process of the formation and growth of new particles from gas precursors in the atmosphere. The process of nucleation may involve two or three species, and is referred as homogeneous or heterogeneous nucleation.

Tn the atmosphere, some low volatility gas cluster together to form small clusters or particles. Therefore, the nucleation is in competition with condensation. The nucleation is favoured when the concentration of gaseous molecules is high, and for gaseous species that have a very low saturation vapor pressure (Seigneur 2019). The clusters formed from gaseous precursors can then grow by colliding with other gas molecules in the atmosphere to grow into aerosol particles. Therefore, the nucleation rate is defined as the number of particles formed per unit volume per unit time. The nucleation rate depends on various factors, including temperature, pressure, and the concentration of gas molecules in the atmosphere. Higher temperatures and lower pressures can both promote the nucleation by making it easier for gas molecules to cluster together.

The nucleation is strongly related to the particle growth in number and size. As this work focuses on mass concentrations, nucleation is not considered.

1.3.3.2 Coagulation

Coagulation refers to the process by which two small particles aggregate and grow into larger particles through collisions and adhesion. The coagulation rate is minimum for two particles of the same size and increases as the difference between the sizes of the two particles increases.

The change in the distribution of the particle number concentration as a function of particle volume due to coagulation is represented by the following equation including the coagulation coefficients between particles of different volumes:

$$\frac{dn_p(v_p)}{dt} = \frac{1}{2}\int_0^{v_p} \beta(v'_p, v_p - v'_p) n_p(v'_p) n_p(v_p - v'_p) dv'_p - \int_0^{\infty} \beta(v_p, v'_p) n_p(v_p) n_p(v'_p) dv'_p \qquad (1.6)$$

Where v_p and v'_p are the volume of two particles, $\beta(v_p, v'_p)$ is the coagulation coefficients between two volumes.

The coagulation coefficients are dependent on the size of the particles and the type of regime they are in, such as the continuous regime for coarse particles and the kinetic theory of gases for ultrafine particles in the free molecular regime. The Fuchs equation is commonly used to parameterize the intermediate regime that corresponds to fine particles (Fuchs 1965).

The coagulation rate between particles depends on their number concentrations, with coagulation being more important for ultrafine particles due to their typically high number concentrations.

1.3.3.3 Condensation/evaporation

The processes of condensation and evaporation refer to the transfer of gaseous molecules to an existing particle and the reverse. These two processes do not change the particle number concentration, only the particle mass concentration and their chemical composition are altered (Seigneur 2019). Condensation/evaporation is impacted by the meteorological parameters including the temperature, pressure and relative humidity. When the vapour pressure in gas phase is higher than the pressure in particle phase, gaseous molecules condense onto particles. Conversely, when the pressure in particle phase is higher than the vapour pressure, particulate molecules evaporate into the gas.

1.4 Urban air quality modeling

Urban air quality are studied through different methods, from experiments to modeling. Based on the scientific understanding of physical and chemical processes in the atmosphere, mathematical tools are used to simulate the transportation and the reaction of air pollutants in different scales. Different environmental factors and parameters are considered in the modeling, including meteorological conditions, emissions, and urban landscape. The modeling is an effective tool for the reproduction and prediction of air quality, and can be contributed to the pollutant-related decision-making for the development of cities.

Regional-scale chemistry-transport models (CTM) are largely used for the air quality modeling, such as Polair3D (Sartelet et al. 2007). Thanks to the large geographic area covered (ranging from tens to thousands of kilometers, with spatial resolution coarser than 1 x 1 km^2), these models are designed to simulate the long-range transport of pollutants across large regions, such as entire countries or continents. However, regional-scale models fail to represent the high concentrations of gaseous and particulate pollutants observed locally in urban areas and in streets. In this context, local-scale models are developed with different complexity and computational costs.

Local-scale air quality models focus on a smaller geographic area. They are designed to reproduce the high concentrations of gaseous and particulate pollutants from a single or several sources in specific areas of cities, such as in streets or in buildings. The landscape characteristics of the modeling area are often also considered, as their impacts on the air pollutant dispersion and conversion are important in local-scale models.

According to the literature, four main groups of local-scale air quality models are used in different studies: Gaussian, Lagrangian, street box models and computational fluid dynamics (CFD).

Gaussian models, such as CALINE4 (Sharma et al. 2013) and ADMS (Carruthers et al. 1994), adopt a Gaussian plume distribution for the pollutant dispersion. These models are largely used to evaluate the impacts of existing and proposed pollutant sources at the local scale (Srivastava and Rao 2011). The computational cost of Gaussian models is low, when representing the dispersion around a single point source, such as an industry. However, the computational cost can be high if line sources, such as roads or streets, are represented as a succession of individual sources. Therefore,

the advantage of Gaussian models is that they are able to study the dispersion around a point source with high efficiency. However, the model is usually simple, the complex urban environmental conditions including the landscape and meteorological conditions cannot be modeled, nor the chemical interactions between pollutants from the regional and local scales.

Lagrangian models such as SPRAY (Gariazzo et al. 2007) and STILT-Chem (Wen et al. 2013) simulate the movement and dispersion of air pollutants by tracking the motion of individual particles or parcels of air. These models use mathematical equations to calculate the transport and diffusion of pollutants as they move through the atmosphere. Unlike Gaussian models, Lagrangian models can simulate complex wind fields and terrain, and can account for chemical reactions and physical processes, and are often used for studying the transport and fate of air pollutants over long distances and timescales. However, the computational cost of Lagrangian models is high. Another drawback of this kind of model is that they fail to simulate the interactions between different phases (Schmidt et al. 2019).

Street-network models such as MUNICH (Kim et al. 2018b, Lugon et al. 2020a) and SIRANE (Soulhac et al. 2011) use parameterised turbulence and wind flow based on CFD simulations and/or wind tunnel experiments. MUNICH uses an eulerian approach to model the street network, allowing coupling with chemical modules and regional-scale transport models. With high spatial resolution and the quick assessments, street-network models are efficient in predicting the air quality in urban areas.

CFD models such as Code_Saturne (Archambeau et al. 2004) are based on numerical algorithms that solve the Navier-Stokes equation for governing mass and momentum of the fluid flow. The spatial resolution of CFD models can be very fine, e.g. lower than 1 m, allowing to accurately simulate and predict the dispersion of air pollutants over complex terrain and assess the impact of emissions from various sources. The cost of CFD models is high, and the conventional CFD models often treat the pollutants as passive scalars, which may lead to some bias for the formation of secondary compounds.

1.5 Presentation of the thesis

This thesis presents urban local-scale indoor and outdoor air-quality studies, focusing on the development of numerical simulations for the understanding of the physical and chemical processes in the atmosphere that affect the formation of air pollutants. Air quality in urban street canyons is studied using the CFD tool Code_Saturne coupled to the chemistry module SSH-aerosol for investigations related to atmospheric chemistry and aerosol dynamics. Indoor air quality is studied for an enclosed stadium in Paris using a 0D indoor air quality model H^2I, which represent with a parameterized approach ventilation, surface adsorption, deposition, and chemical reactions in indoor environments. This thesis is written through a collection of two articles which were published during the PhD period, together with the redaction of one chapter on indoor air quality.

Chapter 2 presents the outdoor gas and particle modeling in an urban street canyon in Greater

Paris. The model validation is conducted through the comparisons of simulated NO_2 and PM_{10} concentrations with measurements. The formation of secondary particles is also studied and the impacts of different processes and emissions are discussed.

In Chapter 3, to study the impact of trees on pollutant concentrations in streets, a tree model is added to the simulations of Chapter 2. The impacts of the aerodynamic effect of tree crowns, atmospheric dry deposition on leaf surfaces and on urban surfaces, and tree VOC emissions are studied for gaseous pollutants and condensables in different meteorological conditions. The overall impact of trees is also evaluated based on the up-mentioned physical and chemical processes.

Chapter 4 presents the modeling of indoor air quality in an enclosed stadium using the H^2I model. The model ventilation parameters are determined in the study through indoor-outdoor measurements of black carbon concentrations. The model is then used to simulate O_3, NO_2 and NO concentrations, and the impacts of different physical and chemical processes on their formation are discussed.

The summary of the results and perspectives for future studies and applications are presented in Chapter 5.

CHAPTER 2

Modeling of gaseous and particulate species in the street

2.1 Summary

NO_2 and particulate matter (PM) may have strong impact on human health. They are both directly emitted by traffic but also formed from gaseous precursors. In order to investigate and understand their evolution at the street level, computational fluid dynamics (CFD) method is used and coupled to the SSH-aerosol model, which represents gas chemistry and aerosol dynamics. The work was done in collaboration with the university of Tokyo. For the CFD simulations, two CFD tools are used and compared: CEREA used Code_Saturne while the university of Tokyo used OpenFoam. Both tools are free and open source.

In the present study, both CFD tools rely on a RANS turbulence model ($k - \varepsilon$). They are coupled with the modular box chemistry model SSH-aerosol to model pollutant dispersion, chemical reactions and aerosol dynamics during a period of 12 hours (from 5 a.m. to 5 p.m., local time, GMT+2 h) in a street of Greater Paris. Sensitivity tests to the mesh and the time step are conducted, in order to determine a configuration that is as computationally efficient as possible. The most computationally cost-effective method is used to perform the simulation. The impact of turbulence model on reactive and non-reactive pollutant concentrations is assessed by comparing the concentrations simulated by the two codes. This comparison of the CFD tools provides a qualitative estimation of the uncertainty associated with the modelling of the atmospheric flow on air quality.

In order to evaluate the models, the simulated concentrations are compared with measurements. However, as the models are built with a simplified 2D domain, the simulation period is chosen, so that it corresponds to a measured wind direction that is almost perpendicular to the street length during a period of 12 hours. This relatively long period of simulation avoids the appearance of fortuitous short-term correspondence between simulated concentrations and measurements, which makes the comparison more convincing. It is found that the simulated NO_2 and PM_{10} concentrations based on the coupled model achieved better agreement with measurement data than the conventional CFD simulation. However, the black carbon concentration is underestimated, which may be explained by the underestimation of non-exhaust emissions (tire and road wear). This simulation set up will also be used for the model evaluation of the study on the impact of trees in the next chapter.

The detailed results and analysis are presented in the following article. This article has been

published in the scientific journal Atmospheric Chemistry and Physics, with the doi 10.5194/acp-23-1421-2023.

2.2 Article

2.2.1 Abstract

In the urban environment, gas and particles impose adverse impacts on the health of pedestrians. The conventional computational fluid dynamics (CFD) methods that regard pollutants as passive scalars cannot reproduce the formation of secondary pollutants and lead to uncertain prediction. In this study, SSH-aerosol, a modular box model that simulates the evolution of gas, primary and secondary aerosols, is coupled with the CFD software, OpenFOAM and Code_Saturne. The transient dispersion of pollutants emitted from traffic in a street canyon is simulated using the unsteady Reynolds-averaged Navier–Stokes equations (RANS) model. The simulated concentrations of NO_2, PM_{10}, and black carbon (BC) are compared with field measurements on a street of Greater Paris. The simulated NO_2 and PM_{10} concentrations based on the coupled model achieved better agreement with measurement data than the conventional CFD simulation. Meanwhile, the black carbon concentration is underestimated, probably partly because of the underestimation of non-exhaust emissions (tire and road wear). Aerosol dynamics lead to a large increase of ammonium nitrate and anthropogenic organic compounds from precursor gas emitted in the street canyon.

2.2.2 Introduction

Traffic-related pollutants can impose adverse effects on pedestrians' health in the urban environment (Anenberg et al. 2017, Jones et al. 2008). Especially particulate matter (PM) is strongly associated with increased cardiovascular diseases (Du et al. 2016). Therefore, investigating the dispersion of PM and the corresponding precursor gas is of great significance to evaluate the environmental impact and devise suitable countermeasures (Kumar et al. 2008).

With the development of numerical simulations, computational fluid dynamics (CFD) has been widely used for near-field dispersion prediction (Tominaga and Stathopoulos 2013). The pollutant dispersion patterns in complex geometric and non-uniform building configurations can be well predicted using CFD simulations (Blocken et al. 2013). Pollutant dispersion, deposition and transformation (chemical re- actions and aerosol dynamics) have primary roles in near-field prediction models. However, most CFD-based studies assume that the timescale of transport at the street scale (100 m) is relatively shorter than the timescale of deposition and transformation; therefore, they frequently regard pollutants as inert matter. Meanwhile, the recirculation flows which commonly exist in street canyons lead to low- ventilation zones and may provide sufficient time for trans- formation (Lo and Ngan 2017, Zhang et al. 2020).

In addition, when PM is transported as a passive scalar, the distribution of the total concentration

can be simulated; however, information on the particle size distribution and chemical composition is unclear. Understanding the size distribution is important for evaluating the health hazards because large particles are deposited in the mouth and upper airways, whereas smaller particles deposit deeper in the lungs and can even reach the alveolar region of the lungs (Sung et al. 2007). Moreover, as particles of different chemical compositions are related to different sources and/or precursor gases, gaining knowledge of their composition may help to devise countermeasures to limit their concentrations (Kim 2019). To simulate pollutant concentrations considering both transport and transformation, many studies have coupled air-quality models with gas-phase chemistry and aerosol modules and achieved chemical transport from a regional scale (100 km) (Sartelet et al. 2007) to a street scale (Lugon et al. 2021b). However, few models can simultaneously represent detailed particle dispersion in a complicated urban flow field considering secondary aerosol formation.

For the recent development and application of the CFD–chemistry coupling model, Kurppa et al. (2018) implemented a sectional aerosol module into large eddy simulation (LES) and conducted a particle dispersion simulation on a neigh-borhood scale. Gao et al. (2022) employed the same model to examine the dispersion of cooking-generated aerosols in an urban street canyon. In both studies, the effect of particle dynamics on aerosol number concentration was well reproduced. However, the simulated chemical composition was not detailed. In addition, the chemical reactions of the precursor gas were not considered. Kim et al. (2019) coupled the unsteady Reynolds-averaged Navier–Stokes equations (RANS) model with gas chemistry and aerosol modules and conducted simulations of PM_1 in a street canyon under summer and winter conditions. The diurnal variations, spatial distribution, and chemical composition of pollutants in the street canyon were investigated. However, the size distribution of particles and the secondary organic aerosol (SOA) chemistry were not considered. Therefore, a more comprehensive coupled model is needed to simulate the evolution of gas concentrations, mass, and number concentrations of primary and secondary particles at the same time.

Vehicles are considered to be the main ammonia (NH_3) source in urban environments (Sun et al. 2017). Reactive nitrogen emissions from many new vehicles are now dominated by NH_3 (Bishop and Stedman 2015). Since the formation of ammonium nitrate is often limited by HNO_3 rather than NH_3 in urban areas (NH_3-limited), increasing NH_3 may lead to increased ammonium nitrate production and PM concentration in urban streets (Lugon et al. 2021b). However, NH_3 emissions from passenger cars are usually not regulated (Suarez-Bertoa and Astorga 2018). Therefore, to provide evidence in making policies for NH_3 emission regulation, it is important to investigate the local influence of NH_3 emissions on PM concentrations.

Therefore, to achieve a more comprehensive simulation of PM and related precursor gas, this study couples soft- ware of two open-source CFD: OpenFOAM (OpenFOAM 2022) and Code_Saturne (Archambeau et al. 2004), with gas-phase chemistry and aerosol module SSH-aerosol (Sartelet et al. 2020). Both OpenFOAM and Code_Saturne own wide users. Therefore, coupling SSH-aerosol with software of both CFD may satisfy more needs. Simulations of the PM concentrations in a 2-D street canyon are conducted. The coupled model is validated by comparison to field measurements. The size distributions and chemical compositions of particles from the models with and without secondary

aerosol formation are compared. In addition, cases with large NH_3 emissions are considered and the related PM increase is investigated.

The remainder of this paper is organized as follows. The coupling of the aerosol model and CFD is introduced in Sect. 2.2.3. The computational details are presented in Sect. 2.2.4. In Sect. 2.2.5, the simulated pollutant concentrations are compared with field measurements, followed by evaluations of the influence of the grid, coupling method, and time step. In Sect. 2.2.6, spatial and temporal variations in the concentrations are analyzed. The chemical compositions and size distributions of the particles between the coupled model and the model that does not consider gas chemistry or aerosol dynamics are compared. In addition, the effect of NH_3 traffic emissions on particle concentrations is discussed. Finally, the conclusions and perspectives are presented in Sect. 2.2.7.

2.2.3 Model description

The coupling method between CFD and chemistry modules is similar to the literature (Gao et al. 2022, Kurppa et al. 2018). OpenFOAM v2012 and Code_Saturne 6.2 are used to solve the governing equations of the flow field and transport equations of gas and particle mass fractions. The inflow conditions, pollutants' background concentrations, and emission rates are obtained from regional models and are linearly interpolated into each time step; this will be introduced in Sect. 2.2.4. This simulation method is called the transient- condition method (TCM) in this study. However, because time-varying flow fields and concentration fields are expensive to compute in terms of computational time, conducting CFD simulations with fixed boundary conditions and emission rates at specific time points is considered a practical method for evaluating street-level pollutant concentrations (Wu et al. 2021, Zhang et al. 2020). The transport (advection and diffusion) and chemical processes will reach equilibrium, and the simulated concentrations will reach quasi-stable values. These values are often regarded as time- averaged concentrations. This method is called the constant-condition method (CCM) in this study, in contrast to TCM. However, the simulation accuracy of CCM has not been validated in simulations that consider both gas chemistry and particle dynamics. Therefore, validation is conducted using boundary conditions and emission rates at specific time points and the simulated concentrations with CCM and TCM are compared in Sect. 2.2.5.2.

The unsteady RANS model is used for the transient simulations with both CFD codes. In OpenFOAM, the RNG (re-normalization group) k–ε model (Yakhot et al. 1992) is deployed for turbulence closure. All transport equations are discretized using the total variation diminishing (TVD) scheme (Harten 1984, Yee 1987), which combines the first-order upwind difference scheme and the second-order central difference scheme. The PIMPLE algorithm, a merged PISO (Pressure Implicit with Splitting of Operator)–SIMPLE (Semi-Implicit Method for Pressure-Linked Equations) algorithm in the OpenFOAM toolkit, is used for pressure–velocity coupling. In Code_Saturne, turbulence is solved using the k–ε turbulence model (linear production) (Guimet and Laurence 2002). The time and space discretization of velocity, pressure, and other scalars in all transport equations are realized through a centered scheme and a fractional step scheme (Archambeau et al. 2004). For both CFD software, the

dry deposition schemes for gas and particle are added to the transport equations using volume sink terms based on Zhang et al. (2003b) and Zhang et al. (2001), respectively. The details of the implementation are provided in Appendix A. The SSH-aerosol (Sartelet et al. 2020) is a modular box model that simulates the evolution of not only gas concentrations but also the mass and number concentrations of primary and secondary particles. In SSH-aerosol, 112 gas species and 40 particle species are considered. The particle compounds are dust, black carbon (BC), inorganics (sodium, sulfate, ammonium, nitrate, and chloride), primary organic aerosol (POA) and secondary organic aerosol (SOA). Three main processes involved in aerosol dynamics (coagulation, condensation/evaporation, and nucleation) are included. The particle size distribution is modeled using a sectional size distribution. Nucleation is not considered in this study because only the mass and not the number of particles is available for evaluation, and large uncertainties remain on the nucleation parameterizations (Sartelet et al. 2022) that mostly affect the number of particles. As nucleation is not considered, the minimum diameter does not need to be as low as 0.001 μm, and it is fixed to 0.01 μm, as in the regional-scale simulations of Sartelet et al. (2018), which provide the background concentrations. Six particle size sections are employed with bound diameters of 0.01, 0.04, 0.16, 0.4, 1.0, 2.5, and 10 μm.

The coupling between CFD and SSH-aerosol is achieved by using the application program interface (API) of SSH- aerosol. The gas and particle concentrations are initialized in CFD and transported in the domain for each time step. For each grid volume cell, these transported concentrations, as well as meteorological parameters, such as temperature and humidity, are then sent to SSH-aerosol to advance 1 time step of gaseous chemistry and aerosol dynamics. Once the SSH-aerosol calculation is completed, the concentrations are sent back to the CFD for the next time step. It should be noted that as the SSH-aerosol processes the ensemble-averaged concentration from the RANS model, the covariance of turbulent diffusion and chemical reaction may not be fully reproduced. The influence of different operator splitting algorithms is discussed in Sect. 2.2.5.4.

2.2.4 Simulation setup

The simulation is set up to model a street in Greater Paris (Boulevard Alsace-Lorraine), where field measurements were conducted from 6 April to 15 June 2014. The concentrations of nitrogen dioxide (NO_2), particles with diameters less than 10 μm (PM_{10}), and black carbon were measured as described in Kim et al. (2018b).

Figure 2.1 shows the simulation domain. The 2-D street canyon is 27.5 m in width (W) and 8.5m in height (H). The domain height is 6 H. The street canyon is discretized into uniform grids in x and z directions. The grid resolutions in the street canyon are 0.5 m in both x and z directions, respectively. The largest grid sizes are 4 m (x) $\times$ 2 m (z). An analysis of the grid sensitivity is described in Sect. 2.2.5.3.

Simulations are conducted from 04:30 LT to 17:00 LT on 30 April 2014 at local time (GMT+2). This period is selected because the wind direction is almost perpendicular to the street canyon during that day, allowing for a 2-D simulation setting. During the field measurement, there are several

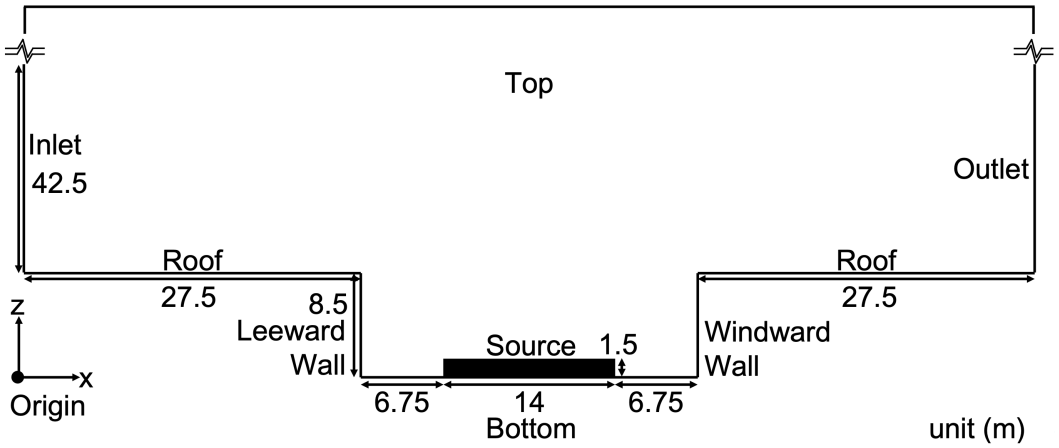

Fig. 2.1 Simulation domain of street canyon.

time periods when the wind direction is perpendicular with the street canyon. Meanwhile, some time periods are short (less than 5 h), and we consider that such a short period simulation is not representative in simulation accuracy. In addition, we consider that it is critical to have a simulation time long enough to cover both daytime chemistry and nighttime chemistry. The first 30 min of the simulation cor- responds to model spin-up, and the simulation lasts 12 h. A sensitivity analysis of numerical aspects, such as the splitting method between transport and chemistry and the time step, is described in Sect. 2.2.5.4.

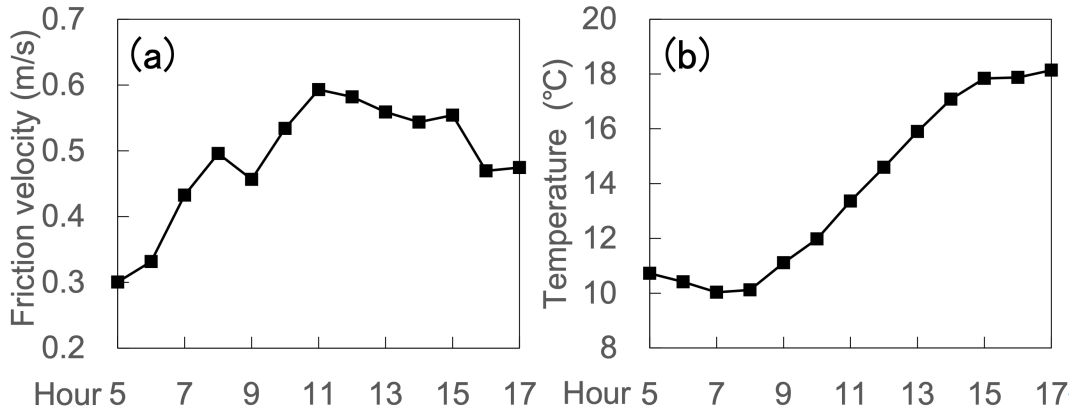

Fig. 2.2 Time variations of hourly (a) friction velocity and (b) temperature for inflow.

Meteorological conditions (Fig. 2.2) including time-varying friction velocity and temperature are obtained from the simulation described in Sartelet et al. (2018) using the Weather Research and Forecasting (WRF) model. The grid resolution is 1 km $\times$ 1 km in Paris. The lowest and highest friction velocities occurred approximately at 05:00 LT and 11:00 LT, respectively. The lowest and highest temperatures are around 08:00 LT and 17:00 LT. For the inflow, the wind direction is perpendicular to the street canyon. The friction velocity u_* is used to prescribe the vertical profiles of the streamwise velocity U, turbulent kinetic energy k, and turbulent dissipation rate ε as follows:

$$U(z) = \frac{u_*}{\kappa} \ln(\frac{z - H}{z_0}) \tag{2.1}$$

$$k(z) = \frac{u_*^2}{\sqrt{C_\mu}} \tag{2.2}$$

$$\varepsilon(z) = \frac{u_*^3}{\kappa(z - H)} \tag{2.3}$$

2.2.5 Model evaluation

where κ is the von Kármán constant and C_μ is the model constant (=0.09) in the k–ε model. The roughness length z_0 is set to 1 m for the inlet (Belcher 2005) and 0.1 m for the wall and bottom (Lo and Ngan 2015).

In addition, since the domain height is low (51 m) in this study and we focus on the pollutant dispersion behaviors in the street canyon, it is reasonable to consider the atmospheric stability as neutral; therefore, the temperature is assumed to be spatially uniform at the inflow. The hourly friction velocities and temperatures are linearly interpolated into each time step and prescribed at the inflow. It should be noted that the general trends are simulated but the fast fluctuations at the inlet are not reproduced. The same linear interpolation is used for background concentrations and emission rates, which will be described in the following.

Figure 2.3a shows the time variations of the PM_{10}, NO, and NO_2 background concentrations. Figure 2.3b and c show the emission rates for NO, NO_2, and the emitted compounds of PM_{10}. The background concentrations of the gas and particles are obtained from the regional-scale simulations of Sartelet et al. (2018) with the Eulerian model Polair3D of the Polyphemus air quality modeling platform (Mallet et al. 2007) which uses the same chemical representation as in this study. As detailed in Sartelet et al. (2018), the regional background concentrations compare well to measurements of O_3, NO_2 , PM_{10} , $PM_{2.5}$, black carbon, and organic aerosols. The hourly background concentrations are linearly interpolated into each time step, and the spatial distribution is uniformly prescribed at the inflow and top. The traffic emission source is assumed to be approximately 14 m in width and 1.5 m in height, and it is set in the middle of the bottom of the canyon (Fig. 2.1). As detailed in Kim et al. (2022), emissions are estimated from the fleet composition and the number of vehicles in the street using COPERT's emission factors (COmputer Program to calculate Emissions from Road Transport, version 2019, (EMEP/EEA 2019)). After the speciation of NOx , volatile organic compounds (VOCs), $PM_{2.5}$, and PM_{10} into model species, emissions are set for 16 gaseous model species and 3 particle model species: dust and unspecified matter (dust), black carbon (BC), and primary organic aerosol of low volatility (POAlP). The PM size distribution at emission is assumed to be the same as in the previous studies (Lugon et al. 2021a,b). The exhaust primary PM is assumed to be in the size bin (0.04–0.16 μm) while non-exhaust primary PM is coarser in the size bin (0.4–10 μm). For the boundary conditions of OpenFOAM, the pressure and gradients of all other variables are set to zero at the outlet. For the walls, we use the wall functions of ε and turbulent kinematic viscosity ν_t for atmospheric boundary layer modeling in the OpenFOAM toolkit (OpenFOAM 2022) based on Parente et al. (2011). The gradients of turbulent kinetic energy k, concentration, and temperature are set to

zero. In Code_Saturne, a two-scale logarithmic friction velocity wall function is used for solving the fluid velocity near wall cell and a three-layer wall function is used for computing other transported scalar profiles such as temperature near the wall (Arpaci and Larsen 1984).

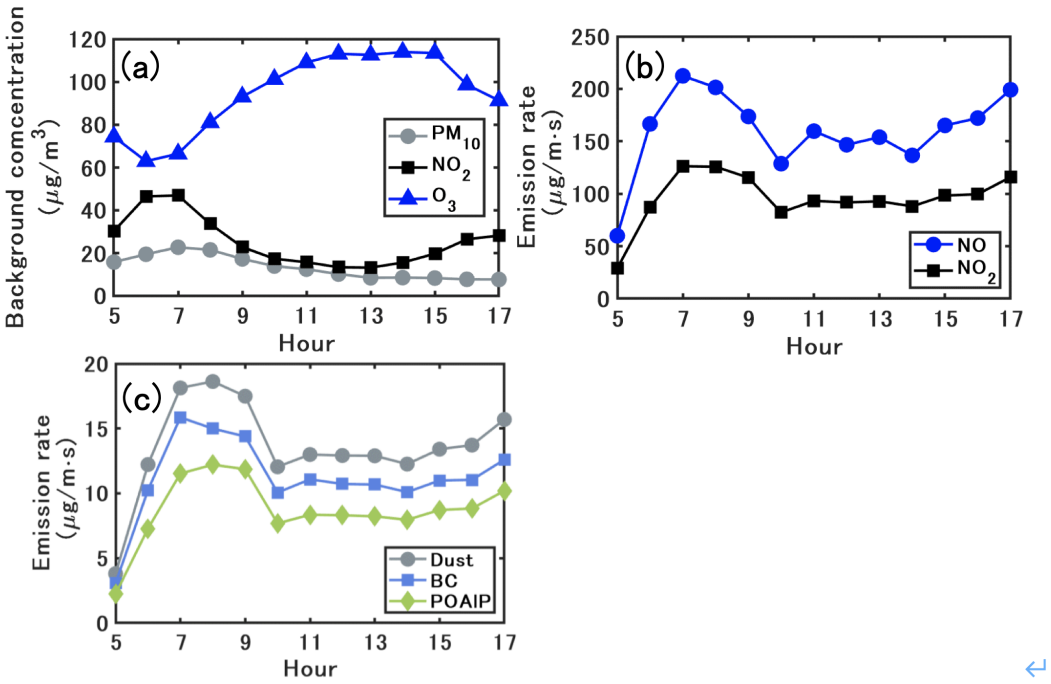

Fig. 2.3 Time variations of (a) PM_{10}, NO and NO_2 background concentrations, (b) emission rates of NO and NO_2 and (c) emission rates of dust, BC, and organics (POAlP).

The turbulent Schmidt number S_{ct} in the concentration transport equations, which is the ratio of the turbulent diffusivity to the concentration and turbulent kinematic viscosity, is important in turbulent diffusion modeling. The value of S_{ct} is considered between 0.2 and 1.3, depending on the flow properties and geometries (Tominaga and Stathopoulos 2007). For urban environments with a compact layout, a small S_{ct} = 0.4 is found to show better agreement with wind tunnel experiment data (Di Sabatino et al. 2007). Therefore, a value of 0.4 is adopted in the current study.

2.2.5.1 Validation with field measurements and comparison of simulated concentrations with the two CFD software

Reproducing the flow field is important in this study. Meanwhile, the observation data on wind velocity are not available. Therefore, we conducted a velocity validation for OpenFOAM v2012 using data from a wind tunnel experiment (Blackman et al. 2015). The predicted mean velocity agreed well with the experimental values. The details can be found in Appendix B.

Figure 2.4 compares the simulated concentrations with those obtained from the field measurements. In the field measurements, the measured concentration was obtained from averaging over two measurement points near the leeward and windward walls in the street canyon. In this section, the simulated results and discussion are based on the spatially averaged values in the street canyon (27.5

$\leq$ x $\leq$ 55, 0 $\leq$ z $\leq$ 8.5 m). The CFD–passive and CFD–chemistry denote the CFD simulation without and with chemistry coupling, respectively. The OF and CS denote simulated concentrations based on OpenFOAM and Code_Saturne, respectively. The operator splitting order and time step for OF and CS are the A-B-A splitting method with 0.5 s and the A-B splitting method with 0.25 s, as detailed in Sect. 2.2.5.4. The simulation time ratio of CFD–chemistry and CFD–passive is about 3 times in both OpenFOAM and Code_Saturne in this study.

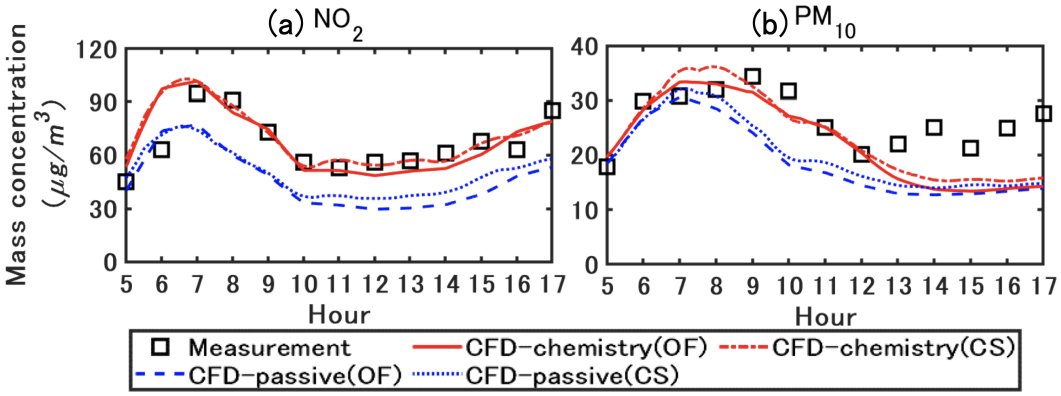

Fig. 2.4 Measured and simulated NO_2 and PM_{10} concentrations. The values are spatially averaged in the street canyon (27.5 $\leq$ x $\leq$ 55, 0 $\leq$ z $\leq$ 8.5 m). CFD–passive and CFD-chemistry denote the CFD simulation without and with chemistry coupling, respectively. OF and CS denote the simulated concentrations based on OpenFOAM and Code_Saturne, respectively. All concentrations are represented in local time (GMT+2).

For NO_2, the peak concentration in the field measurement occurred approximately at 07:00 LT owing to the morning traffic. In the CFD–passive simulations, the lack of chemical reactions lead to an underestimation of NO_2, while the concentrations simulated with CFD–chemistry agree well with the measurements. For PM_{10}, the concentrations simulated with CFD–chemistry also show better agreement with the measurements than CFD–passive. The primary reason is that CFD–chemistry can reproduce the condensation of inorganic and organic matter from the gas phase to the particle phase, which will be further explained in the following sections. The simulation results based on OF and CS show small differences, and detailed comparisons are presented in Fig. 2.6.

Validation metrics (Chang and Hanna 2004) are used to quantify the overall accuracy of the CFD simulated concentrations based on OF compared with the measured values (Castelli et al. 2018, Ferrero et al. 2019). The following metrics are used: fractional bias (FB), geometric mean bias (MG), and normalized mean square error (NMSE). These metrics are defined as follows:

$$FB = \frac{\overline{Obs} - \overline{CFD}}{0.5(\overline{Obs} + \overline{CFD})} \tag{2.4}$$

$$MG = \exp(\overline{\ln Obs} - \overline{\ln CFD}) \tag{2.5}$$

$$NMSE = \frac{\overline{(Obs_i - CFD_i)^2}}{\overline{Obs} \times \overline{CFD}} \tag{2.6}$$

where Obs_i and CFD_i are the measured and CFD-simulated concentrations for the compound/species i, respectively. The overbar represents the mean value of the entire dataset. The ideal values are 1 for MG and 0 for FB and NMSE. Previous research has suggested that $|FB| < 0.3$, $0.7 < MG < 1.3$ and $NMSE < 4$ are acceptable for simulated concentrations (Hanna et al. 2004).

Table 2.1 Statistical indicators for NO_2 and PM_{10} in the street canyon from 05:00 LT to 17:00 LT. The concentrations are simulated with OpenFOAM.

	Concentration (μg m^{-3})		Validation metrics		
NO_2	Mean	Percentile 90%	FB	MG	NMSE
Measurement	66.6	91.8	-	-	-
CFD-chemistry	67.3	97.3	-0.01	1.00	1E-4
CFD-passive	45.9	73.7	0.36	1.50	0.14
PM_{10}	Mean	Percentile 90%	FB	MG	NMSE
Measurement	26.4	32.5	-	-	-
CFD-chemistry	22.3	33.1	0.17	1.23	0.03
CFD-passive	18.8	28.9	0.34	1.45	0.13

Table 2.1 shows the statistical indicators for spatially averaged concentrations of NO_2 and PM_{10} in the street canyon from 05:00 LT to 17:00 LT. For NO_2 and PM_{10}, the mean and 90% percentile concentrations simulated with CFD–chemistry are closer to the measurements than those simulated with CFD-passive. In addition, the FB, MG, and NMSE values of CFD–chemistry are closer to the ideal values than those of CFD–passive.

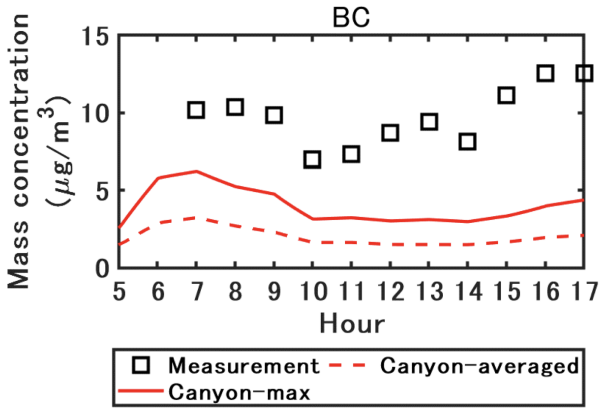

Fig. 2.5 Measured and simulated black carbon concentrations with OpenFOAM. The canyon-averaged and maximum concentrations in the street canyon are represented by the plain line and the dashed line, respectively ($27.5 \leq x \leq 55$, $0 \leq z \leq 8.5$ m).

The black carbon (BC) concentration simulated with OF is compared with the measurements in Fig. 2.5. Because BC is considered an inert matter, considering chemistry does not influence the mass concentration. Therefore, the concentrations simulated with CFD–passive and CFD–chemistry show little difference; only the concentration simulated with CFD–chemistry is shown here. The BC concentrations are under-estimated by a factor of approximately 5. Even the maximum concentrations in the street canyon largely underestimate the measurements. One of the causes of this underestimation

may be the underestimation of the non-exhaust tire emission factors in the COPERT emission factors used here (Lugon et al. 2021a).

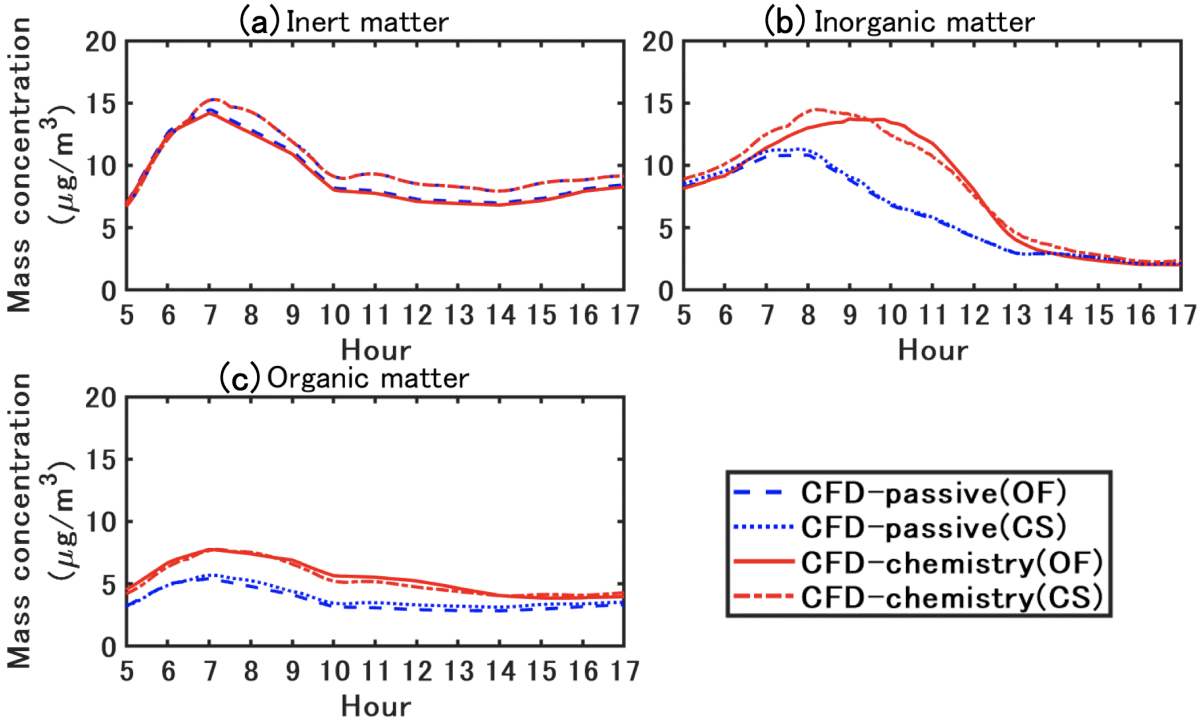

Fig. 2.6 Simulated particle concentrations with OpenFOAM (OF) and Code_Saturne (CS). CFD–passive and CFD–chemistry denote the CFD simulation without and with chemistry coupling, respectively.

The particle concentrations simulated with OF and CS are compared in Fig. 2.6. The evolutions of the concentrations simulated by OF and CS are similar. Higher PM_{10} concentrations are simulated by CS around 08:00 LT during the traffic peak and in the afternoon, mostly because of the higher concentrations of emitted inert compounds such as black carbon and dust. Differences in the turbulence scheme may explain these variations. Meanwhile, the difference between CFD–passive and CFD–chemistry for the inorganic and organic matter is in accordance with OF and CS, showing the robustness of the coupling method between CFD and SSH-aerosol by API. For simplicity, only the simulated concentration based on OF is presented and discussed in the following sections.

2.2.5.2 Transient-condition method and constant-condition method

To validate the simulation accuracy of CCM in simulations that consider both gas chemistry and particle dynamics, simulations are conducted using boundary conditions and emission rates at five time points (07:00 LT, 10:00 LT, 13:00 LT, 15:00LT, and 17:00LT). Other simulation conditions, including the grid, coupling method, and time step, are the same as the transient-condition simulation.

In Fig. 2.7, for PM_{10} and NO_2, the concentrations simulated with CCM (red triangles) are similar to those simulated with TCM. In addition, depending on the background concentration and emission conditions, the simulation time required for CCM to reach dynamic equilibrium is less than 1000 time

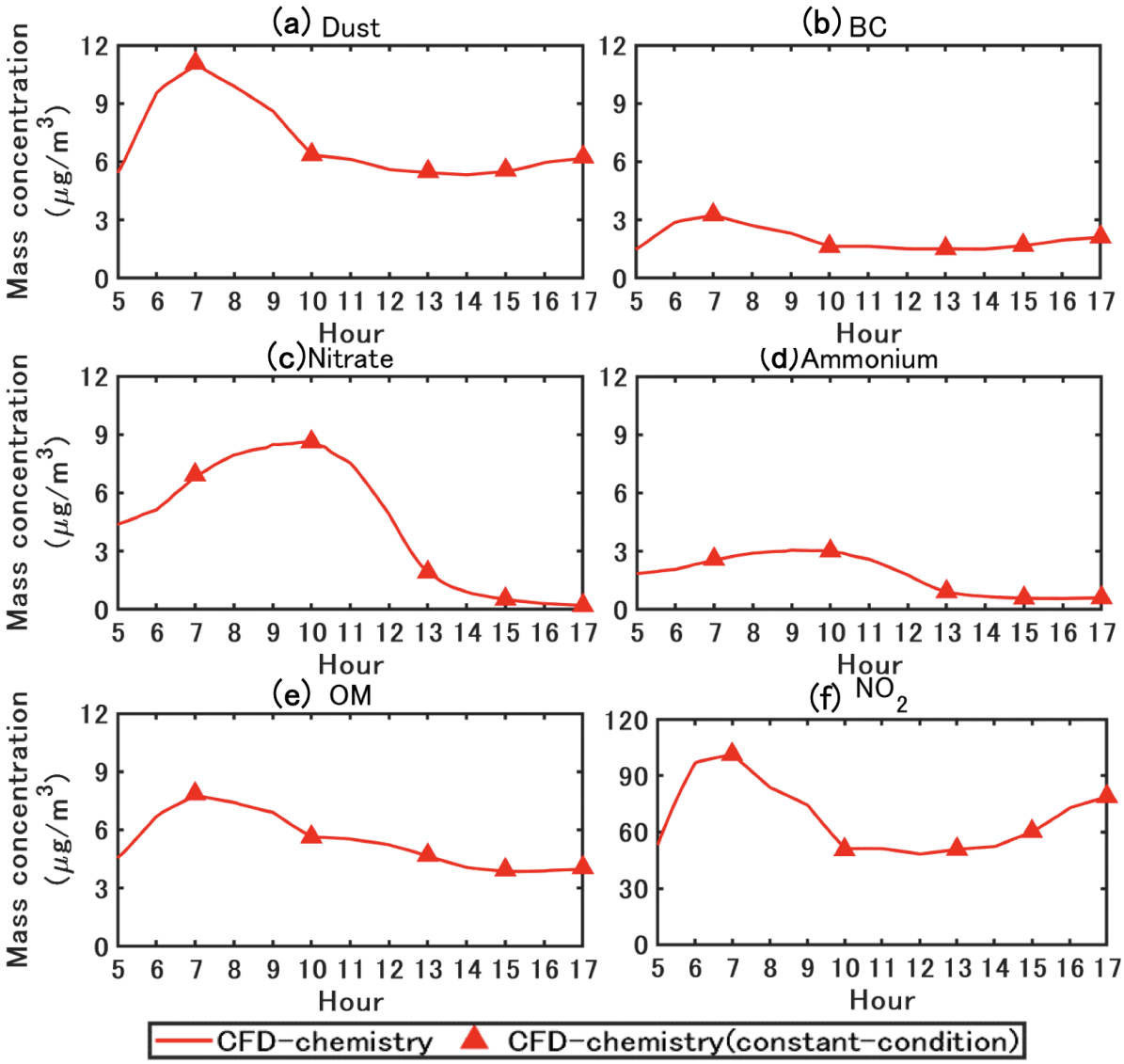

Fig. 2.7 Simulated PM_{10} and NO_2 concentrations with the transient-condition and constant-condition methods. The concentrations are spatially averaged in the street canyon.

steps (approximately 500 s). Therefore, CCM can be utilized for parameter studies. The sensitivity analysis of the grid, coupling method, and time step in Sect. 2.2.5.3 and 2.2.5.4 is based on CCM. However, CCM should be used with caution when the inflow wind speed and direction vary rapidly. The simulated concentrations in Sect. 2.2.6 are based on TCM.

2.2.5.3 Grid sensitivity

A grid sensitivity analysis is conducted based on three different resolutions as shown in Fig. 2.8. The grid resolutions in the street canyon for coarse, basic, and fine grids are 1m, 0.5m, and 0.25m in both x and z directions, respectively. The largest grid sizes are 4m (x) $\times$ 2m (z) for the coarse and basic grids, and 2 m (x) $\times$ 2 m (z) for the fine grid. The simulations are based on the constant-condition method (CTM). The A-B-A splitting method, which is introduced in Sect. 2.2.5.4, is used with a time step of 0.5 s. Figure 2.9 shows the comparative results for the mass concentration. No significant discrepancy is observed between the different grids for NO_2, inert matter, and organic matter. Meanwhile, the simulated inorganic matter based on coarse grids shows slightly smaller concentrations than the other grid resolutions, while the concentrations based on basic and fine grids are close. Therefore, the basic grid is adopted for simulations in this study.

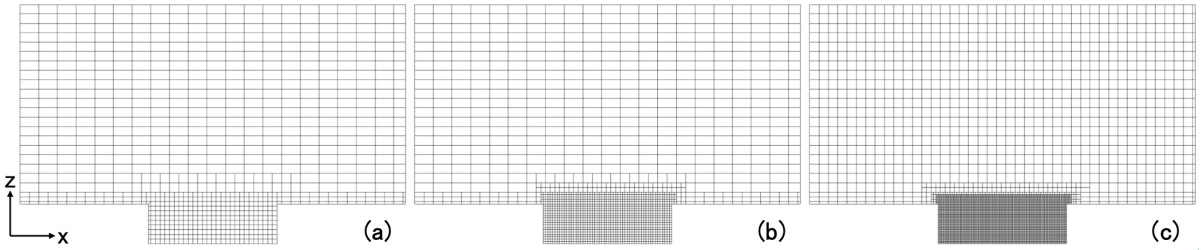

Fig. 2.8 Different grid resolutions for sensitivity analysis: (a) coarse, (b) basic, (c) fine. The grid resolutions in the street canyon are 1 m, 0.5 m, and 0.25 m in both x and z directions, respectively. The largest grid sizes are 4 m (x) $\times$ 2 m (z) in the coarse and basic grids, and 2 m (x) $\times$ 2m (z) in the fine grid.

2.2.5.4 Coupling method and time step sensitivity

The transport equation for the chemical species includes terms of advection, diffusion, emission, and chemical reactions. Ideally, the transport equation should be solved with all the above terms, that is, by coupling all processes. However, the chemical process is integrated with a stiff integrator, whereas advection, diffusion, and emission are integrated with a flux scheme. Therefore, operator splitting (Sportisse 2000) is often employed to solve different terms individually and sequentially over a given time step in chemical transport simulations (Fu and Liang 2016). In this study, advection, diffusion, and emission are simultaneously solved in CFD, and the chemical reactions including

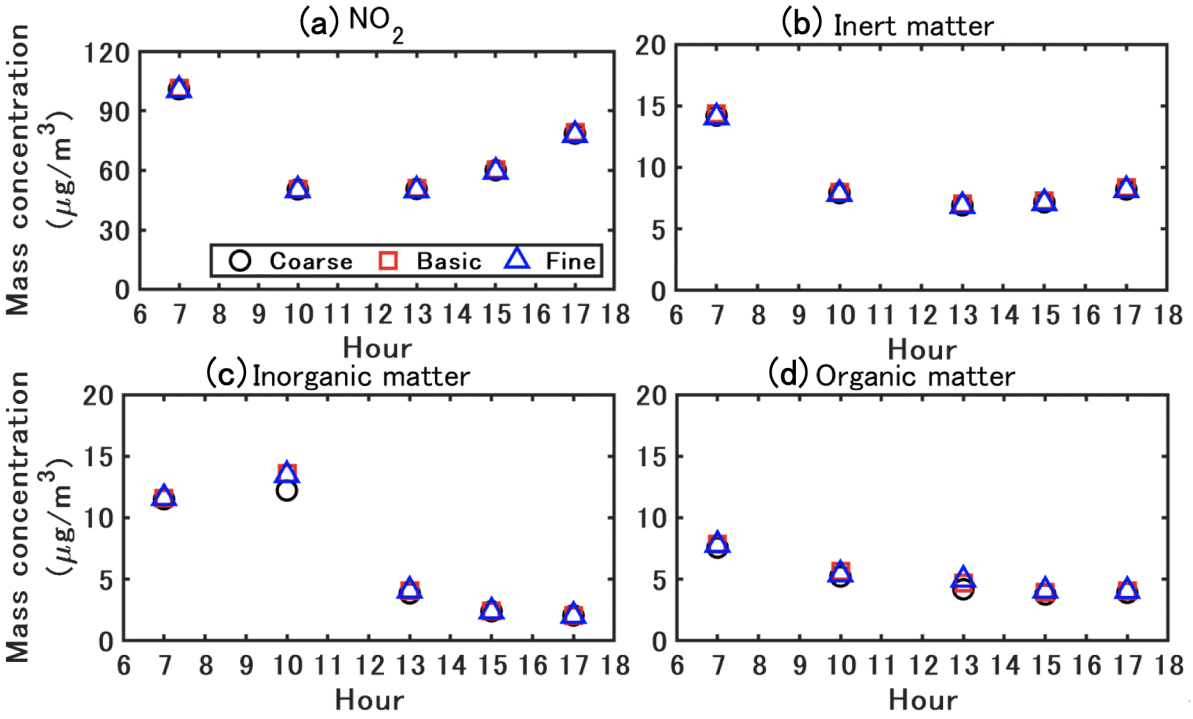

Fig. 2.9 Simulated NO_2 and particle concentrations with different grid resolutions.

gas chemistry, particle dynamics, and size redistribution are solved in SSH-aerosol. Two operator-splitting orders are considered for coupling: A–B splitting and A–B–A splitting (Sportisse 2000). For A-B splitting, which can be summarized as CFD(Δt)–Chemistry(Δt), the mass concentrations are first integrated for transport over a time step Δt. The updated concentrations are then integrated for chemistry at the same Δt. On the other side, A–B–A splitting adopts a symmetric sequence of operators, which can be summarized as CFD($\Delta t/2$)–Chemistry(Δt)–CFD($\Delta t/2$). The mass concentrations are first integrated for transport over a half time step, then for chemistry over the full time step, and finally for transport again over a half time step.

Table 2.2 Relative change in the computation time with different operator-splitting order and time steps. The computation time is normalized by ABA-05.

Case	Operator splitting order	Δt (s)	Change in the computation time
AB-05	A-B splitting	0.5	0.90
AB-025	CFD(Δt)-Chemistry($\Delta t/$)	0.25	1.56
ABA-1	A–B–A splitting CFD($\Delta t/2$)-	1	0.57
ABA-05	Chemistry($\Delta t/$)- CFD($\Delta t/2$)	0.5	1
ABA-025		0.25	2.44

A sensitivity analysis is conducted on the operator-splitting method and splitting time step. As shown in Table 2.2, the time step is considered 0.5 and 0.25 s for the A–B splitting (named AB-05 and AB-025), and 1, 0.5, and 0.25 s for the A–B–A splitting (named ABA-1, ABA-05, and ABA-025). The simulated NO_2 and particle concentrations are presented in Fig. 2.10. The ABA-1 and AB-05

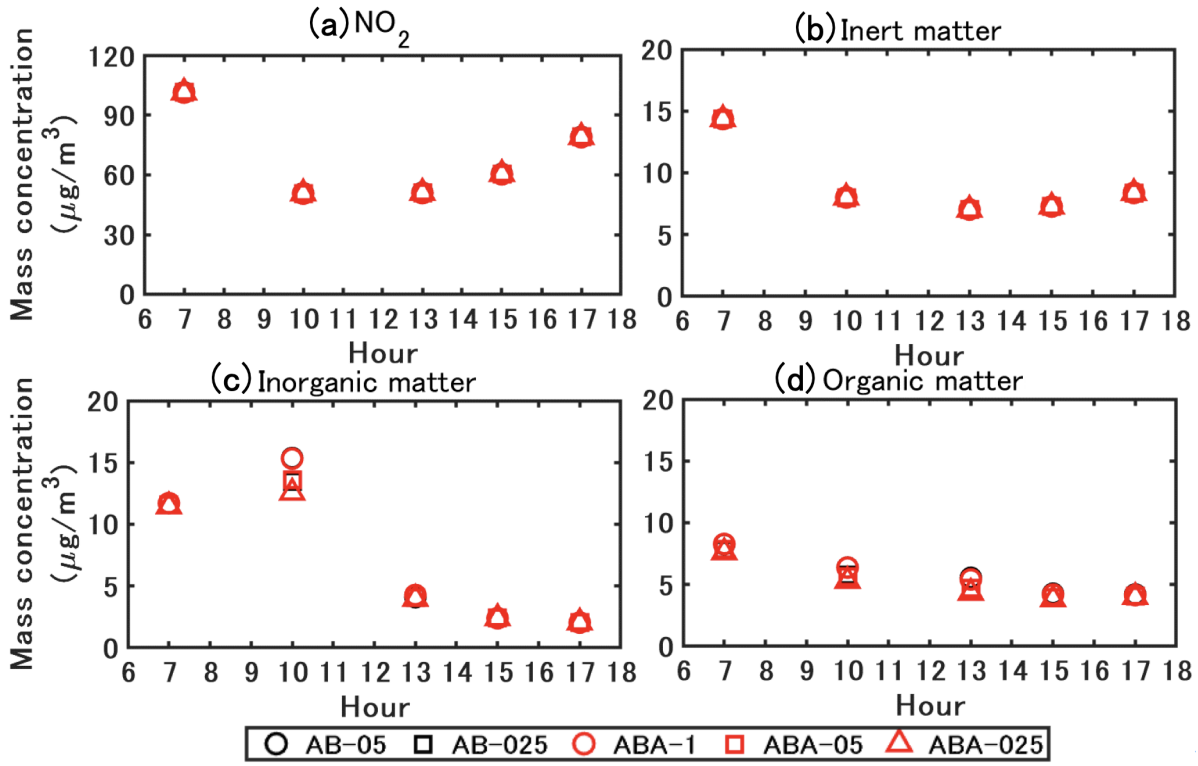

Fig. 2.10 Simulated NO and particle concentrations with different coupling methods and time steps. ABA denotes the A–B–A splitting method: CFD(1t/2)–Chemistry(1t)–CFD(1t/2). AB denotes the A–B splitting method: CFD(1t)–Chemistry(1t). In the legend, the values that follow the capital letter ABA or AB denote the time step 1t (in s) used in the simulation.

concentrations hardly differ from the figures. Meanwhile, the computational time of ABA-1 is only 63% of that of AB-05. Similarly, the concentrations simulated with ABA-05 and AB-025 are almost the same, and the computational time of ABA-05 is only 64% of AB-025. Therefore, the A–B–A splitting method can be considered as a cost-effective method.

The concentrations simulated with the A–B–A splitting method and different time steps show that a small time step results in low inorganic and organic matter concentrations. The concentrations simulated with ABA-1 are larger than those of ABA-05, and larger than ABA-025. However, the differences between the concentrations simulated with ABA-05 and ABA-025 are lower than the differences between ABA-1 and ABA-05. For NO_2 and inert particles, no obvious difference is found between the simulations with different splitting methods and splitting time steps. Therefore, the A–B–A splitting method with a time step of 0.5 s is adopted in this study.

2.2.6 Results and discussion

2.2.6.1 Time-averaged flow field and concentration field

This section shows the results for time-averaged values from 05:00 LT to 17:00 LT. Figure 2.11 shows the 12 h time-averaged streamwise velocity and wind direction in the street canyon. At the current aspect ratio (H / W = 0.31), a large vortex is observed in the canyon with a small secondary vortex at the corner of the leeward wall. A reverse flow is ob- served in the lower half of the canyon.

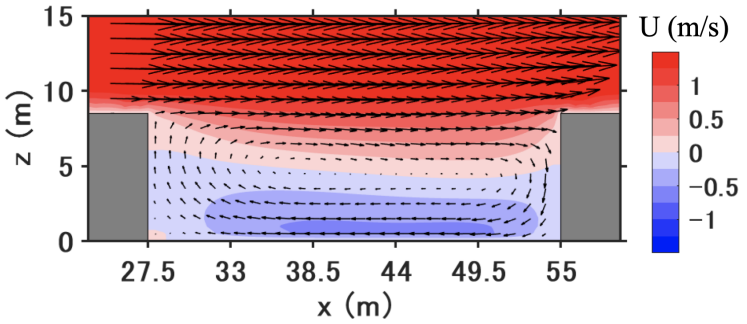

Fig. 2.11 Time-averaged flow field in the street canyon from 05:00 LT to 17:00 LT.

Figure 2.12 shows the time-averaged concentrations of the gaseous pollutants from 05:00 LT to 17:00 LT. For gaseous pollutants emitted by traffic, such as NO_2 , NO, and NH_3 , larger concentrations are found in the street, particularly near the leeward wall, compared to the windward wall due to the reverse flow. Simultaneously, gas-phase chemistry and condensation/evaporation between the gas and particle phases also influence the concentration distribution. NO_2 mainly increases due to chemical production from NO emissions and background O_3. Compared to the background NO_2 concentration of 26 μg m^{-3}, the longest retention time at the leeward side corner leads to the street canyon's largest

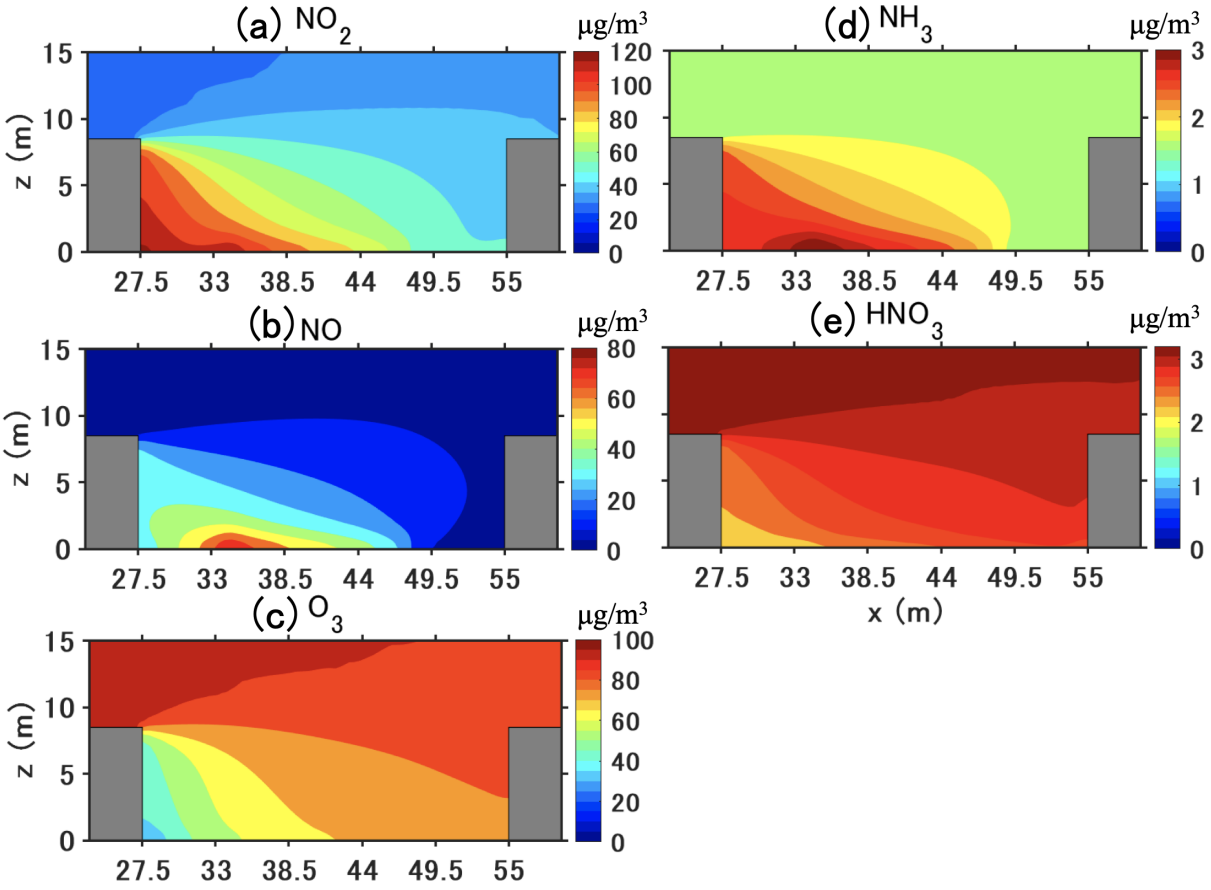

Fig. 2.12 Time-averaged concentrations (μg m^{-3}) of gaseous pol- lutants in the street canyon from 05:00 LT to 17:00 LT.

concentration (121 μg m^{-3}). At pedestrian height (z=1.5 m), NO_2 concentration is 116 μg m^{-3} at the leeward wall and 49 μg m^{-3} at the windward wall.

However, NO and NH_3 generally decrease because of loss by gaseous chemistry and the condensation of ammonium nitrate, respectively; therefore, the largest concentrations are at the leeward corner of the traffic emission source. For secondary gaseous pollutants without traffic emissions such as O_3 and HNO_3, gaseous chemistry and condensation lead to lower concentrations in the street canyon than background concentrations. For O_3, this is due to the titration of O_3 by NO, whose concentration is large near the leeward wall. For HNO_3 , this is because of the high concentrations of NH_3 , which then condenses with HNO_3 to form ammonium nitrate. In addition, the lowest concentration of O_3 and HNO_3 can be found at the leeward corner which corresponds to the secondary vortex in Fig. 2.11, indicating that the pollutant residence time is the highest in that corner leading to enhanced ozone titration.

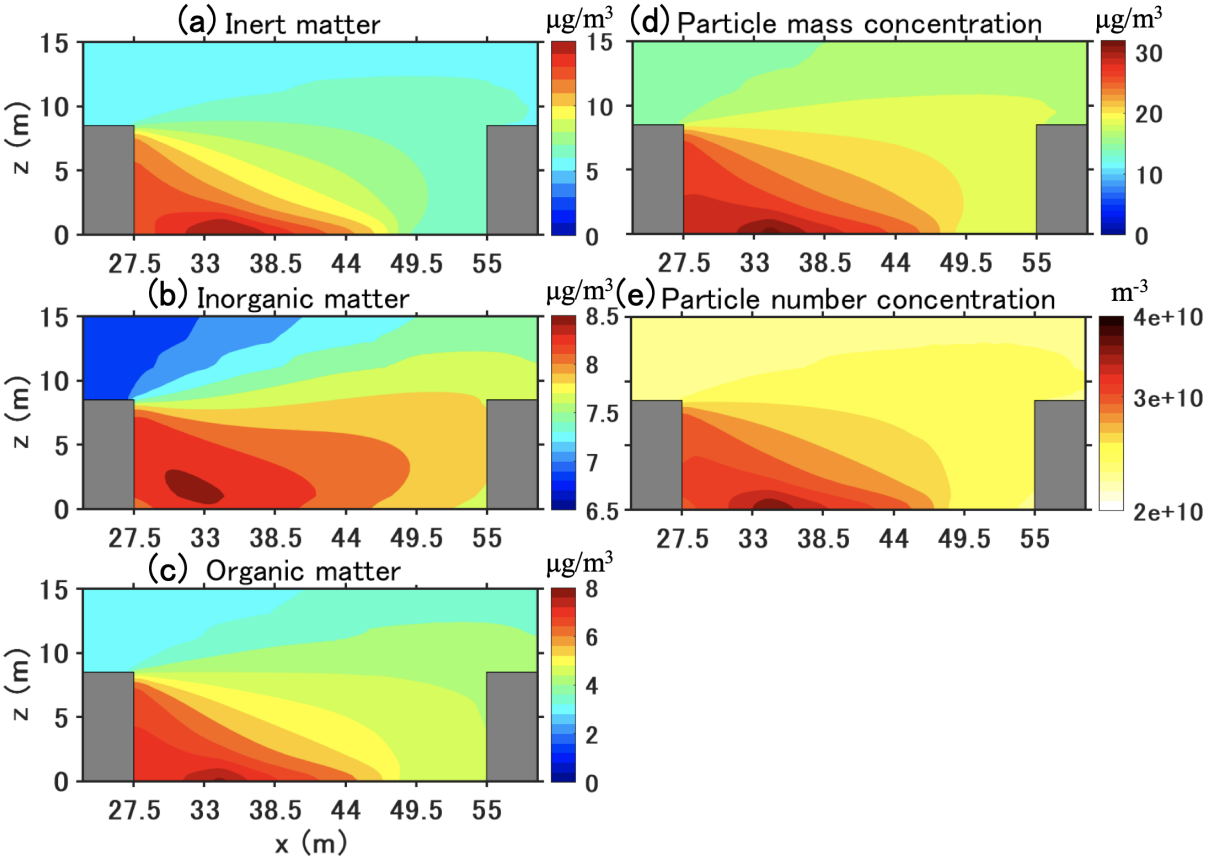

Fig. 2.13 Time-averaged concentrations of particle number, mass, and composition in the street canyon from 05:00LT to 17:00LT. The unit is μg m^{-3} for mass concentration and m^{-3} for number concentration.

Figure 2.13 shows the time-averaged PM_{10} mass concentration and the number concentrations and PM composition (inorganic, organic and inert matter) from 05:00 LT to 17:00 LT. For inert and organic matter, the highest concentrations are near the leeward corner of the traffic emission source. Because inorganic matter is not emitted, the concentration distribution differs from inert and organic

matter. However, as they are produced from gas condensation and strongly influenced by traffic emissions, the highest concentrations are observed in the leeward corner.

At pedestrian height (z = 1.5 m), the PM_{10} mass concentration is approximately 28 μg m^{-3} at the leeward wall and 19 μg m^{-3} at the windward wall, which is larger than the background concentration of 15 μg m^{-3}. The number concentration is computed from the mass concentration and therefore has a similar spatial distribution as PM_{10} mass concentration (nucleation from gas was not taken into account). Traffic emission significantly increases the number concentration. The number concentration is about 2.3 $\times$ 1010 m^{-3} in the background, whereas the largest number concentration in the street canyon is about 3.8 $\times$ 1010 m^{-3}.

2.2.6.2 Time-variant characteristics

Figure 2.14 shows the simulated time-varying concentrations of ammonium nitrate formed by the condensation of HNO_3 and NH_3. Based on the traffic fleet in the current study, NH_3 emission is approximately 1%–2% of NO emissions. Ammonium nitrate and HNO_3 are not emitted and differences between simulations with or without chemistry coupling are due to gas chemical reactions and phase change between the gas and particle. Phase change may be driven by NH_3 emissions as well as the non-thermodynamic equilibrium of the background concentrations.

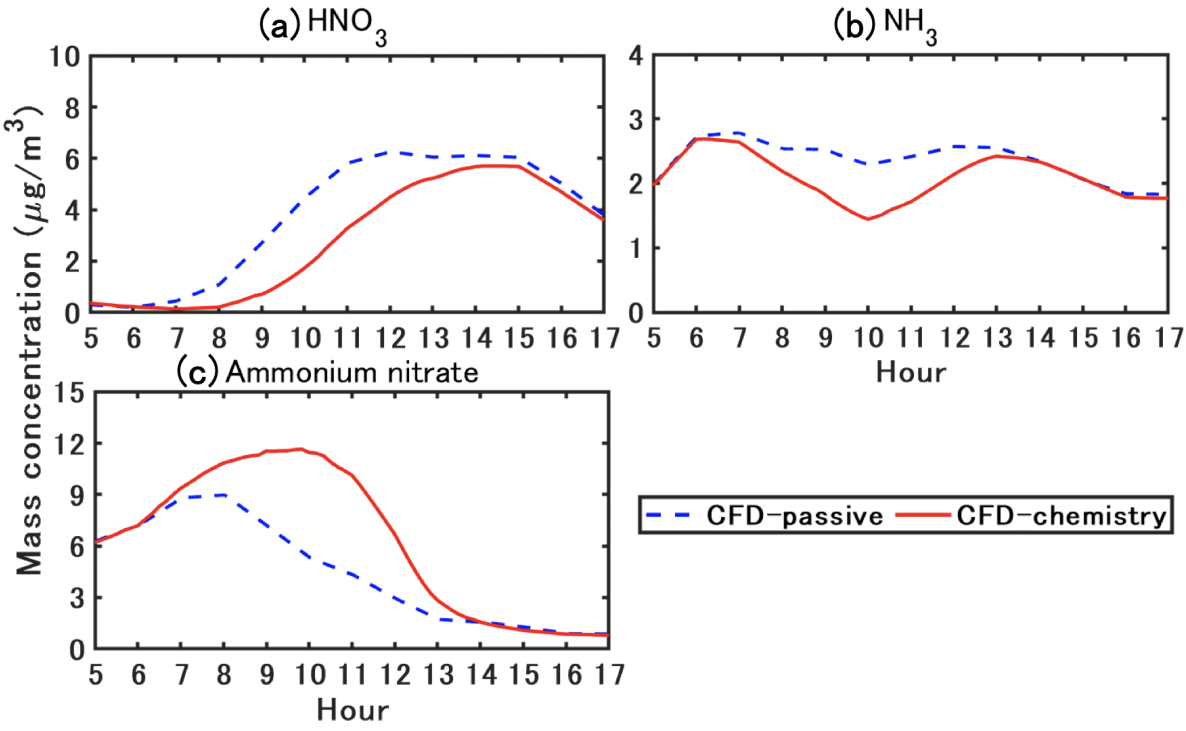

Fig. 2.14 Simulated time-varying concentrations of ammonium nitrate and precursor gas (HNO_3 and NH_3).

In CFD–passive, NH_3 concentration peaks around 07:00 LT as NOx because it is emitted by traffic. The peak in HNO_3 concentration is later in the morning, around 11:00 LT. HNO_3 is formed from

the oxidation of NO_2, which is emitted by traffic and is rapidly formed from NO traffic emissions. The formation of HNO_3 is slower than the formation of NO_2; it probably occurs at the regional scale, leading to a delay in the peak of HNO_3 concentration compared to NO_2 concentration. In CFD–chemistry, the temporal variations of HNO_3 concentration show large differences with CFD–passive because HNO_3 condenses with NH_3 to form ammonium nitrate during the daytime. As a result, the HNO_3 concentration peak in CFD–chemistry is later than that in CFD–passive (it is shifted from 11:00 LT to around 14:00 LT). The NH_3 concentration in CFD–passive peaks at 07:00 LT because of traffic emission and is stable from 07:00 LT to 13:00 LT and then decreases from 13:00 LT. Meanwhile, the condensation in CFD–chemistry leads to lower concentration than in CFD–passive during the daytime (between 07:00 LT and 13:00 LT).

For 12 h time-averaged concentrations, ammonium nitrate increases by 46% in CFD–chemistry compared with that in CFD–passive. Background ammonium nitrate concentration (CFD–passive) peaks around the morning rush (07:00–08:00 LT) and then decreases. Meanwhile, in CFD–chemistry, ammonium nitrate concentration peaks later around 10:00LT because of the large increase in HNO_3 between the traffic rush and 10:00LT. However, although HNO_3 concentration does not vary much between 11:00 LT and 15:00 LT, the ammonium nitrate concentration decreases from 10:00 LT to a very small level (lower than 1 μg m^{-3}) after 14:00 LT. This decrease is probably linked to the temperature increase during the daytime (Fig. 2.2b) and the relative humidity decrease, leading to a decrease in the condensation rate (Stelson and Seinfeld, 1982).

Figure 2.15 shows the simulated time-varying concentrations of organic matter. Organic matter is divided into two main categories depending on the origin of the precursors: Bio and Ant refer to the organic matter of biogenic and anthropogenic precursors, respectively.

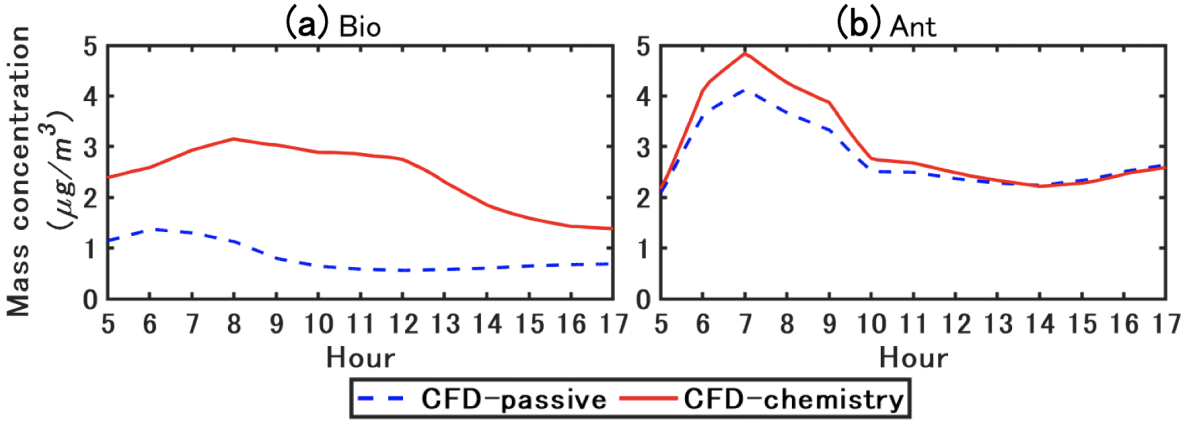

Fig. 2.15 Simulated time-varying concentration of organic matter. Bio refers to organic matter formed from biogenic precursors. Ant refers to organic matter formed from anthropogenic precursors.

In CFD–chemistry, Bio concentration is larger than that in CFD–passive. As biogenic precursors are not emitted in the street, the condensation of Bio is due to background precursor gases. As discussed previously, the concentration of ammonium nitrate is higher in CFD–chemistry than in CFD–passive, providing a larger aqueous mass onto which hydrophilic compounds of the biogenic

precursor gases condense. As the condensation of ammonium nitrate decreases in the afternoon as shown in Fig. 2.15, the condensation of Bio also decreases.

Ant is largely influenced by traffic emissions in the street, particularly by emissions of semi-volatile compounds (Sartelet et al., 2018) which soon condense after emissions. Therefore, there is a peak around 07:00 LT owing to the morning rush. In the model, anthropogenic emissions are mostly hydrophobic, therefore the condensation is not enhanced by the increase in inorganic concentrations. Consequently, the difference between CFD–chemistry and CFD-passive is larger in the morning owing to the large increase in traffic emissions, but small differences are observed in the afternoon.

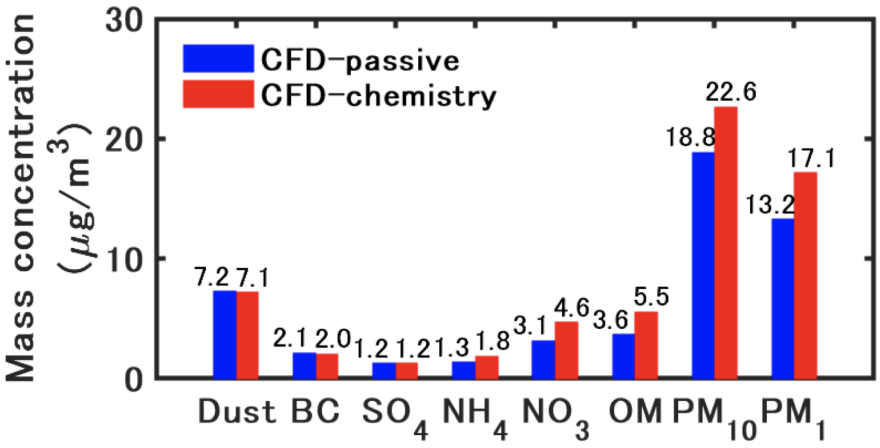

Fig. 2.16 Time-averaged concentration of PM_{10}, PM_1 and the chemical compounds of PM_{10} from 05:00 to 17:00.

Figure 2.16 shows the time-averaged concentrations of PM_{10} , PM_1 , and the chemical compounds of PM_{10} from 05:00 LT to 17:00 LT. The time-averaged PM_{10} and PM_1 concentrations increase by approximately 3.8 μg m^{-3} in CFD–chemistry compared to CFD–passive, indicating that chemistry mainly influences small particles. Inert matter slightly decreases in CFD–chemistry owing to dry deposition. Condensation increases by 48%, 38%, and 53% of nitrate, ammonium, and organic matter concentrations, respectively, in CFD–chemistry compared to CFD–passive.

2.2.6.3 Size distribution of particulate matter

Figure 17 shows the time-averaged size distribution of PM_{10} for the different chemical compounds of particles from 05:00 LT to 17:00 LT. The bound diameters are 0.01, 0.04, 0.16, 0.4, 1.0, 2.5, and 10 μm, and the mean diameters are 0.02, 0.08, 0.25, 0.63, 1.58, and 5.01 μm.

For the total concentration of PM_{10} (Fig. 2.17a), the lowest and the largest concentrations are in the first size section (0.01–0.04 μm) and the second size section (0.04– 0.16 μm) respectively, for both the CFD–passive and the CFD–chemistry simulations. Generally, the loss and gain of mass concentration in each size section are related to emission, dry deposition, coagulation (small particles coagulate into large particles), and condensation/evaporation (phase exchange between gas and particles).

Figure 2.17b shows the mass concentration ratio between CFD–passive and CFD-chemistry for

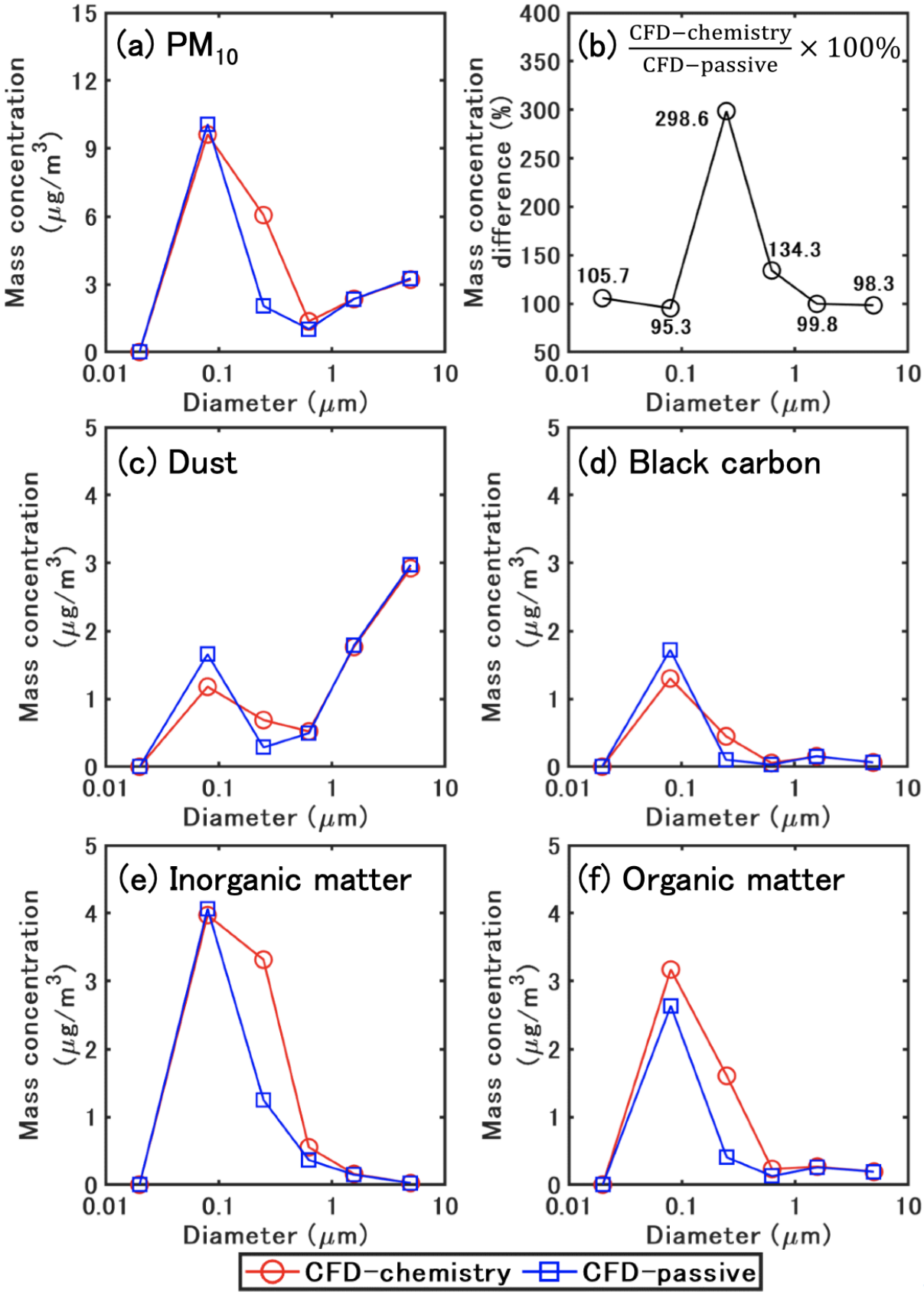

Fig. 2.17 Time-averaged size distribution of PM_{10} for different chemical species from 05:00 LT to 17:00 LT.

each size section. For particles in the size range of 0.04–0.16 μm, the concentrations are smaller in CFD-chemistry than in CFD–passive, because dry deposition and coagulation both decrease mass concentration for those particles. Furthermore, semi-volatile gases may evaporate from small particles because of the Kelvin effect and condense onto larger particles. For particles in the size range of 0.16–1.0 μm, the concentrations are much larger in CFD–chemistry than CFD–passive, indicating that coagulation and condensation on the mass-concentration increase are dominant to other processes, such as deposition. For particles larger than 1 μm, the concentrations of CFD–passive and CFD–chemistry are similar because particle dynamics have a low influence on large particles.

The size distribution of dust (Fig. 2.17c) shows that most dust mass concentrations are in particles larger than 1 μm. Meanwhile, most of the mass concentration of BC, inorganic, and organic matter (Fig. 2.17d–f) is in particles smaller than 1 μm. Coagulation is the main process influencing the size distribution for inert matter (dust and BC). Compared to CFD–passive, the mass concentration of dust and BC in the second size section decrease by 0.48 and 0.43 μg m^{-3} in CFD–chemistry. Correspondingly, the mass concentrations of dust and BC in the third size section increase by 0.41 and 0.35 μg m^{-3}.

For inorganic matter, in the second size section, the concentrations are similar in CFD-passive and CFD–chemistry: particle dynamics decrease sulfate concentration by 0.32 μg m^{-3} and increase nitrate concentration by 0.17 μg m^{-3}. However, because of the results of the combination effect of coagulation and ammonium nitrate condensation, the concentrations largely increase in the third size section in CFD–chemistry: sulfate, ammonium ,and nitrate increase by 0.27, 0.6 and 1.24 μg m^{-3}, respectively.

For organic matter, because of the condensation of hydrophilic compounds from background biogenic gases and anthropogenic emissions, CFD–chemistry leads to a small increase in concentrations (0.53 μg m^{-3}) in the second size section and a large increase in the third section (1.21 μg m^{-3}) compared to CFD–passive. In detail, Bio concentrations increase by 0.89 μg m^{-3} and Ant concentrations decrease by 0.36 μg m^{-3} in the second size section. In the third size section, Bio and Ant concentrations increase by 0.67, 0.54 μg m^{-3}.

2.2.6.4 Influence of ammonia traffic emissions

Suarez-Bertoa et al. (2017) conducted on-road measurements of NH_3 emissions from two Euro 6b compliant light-duty cars (one gasoline and one diesel) under real-world driving conditions, and they found that NH_3 emissions accounted for 11.9% and 0.92% of NOx emissions for gasoline and diesel vehicles. As explained in Sect. 2.2.6.2, NH_3 emissions are approximately 1%–2% of NOx emissions in the reference case. Two cases are considered to simulate the impact of an increase in the fraction of gasoline cars, and sensitivity simulations are performed with NH_3 emissions considered as 10% and 20% of the NOx emissions.

Figure 2.18 shows the sensitivity of ammonium nitrate concentration to NH_3 emissions. A larger NH_3 emission delays the peak of ammonium nitrate by approximately 1 h. For a 12 h average,

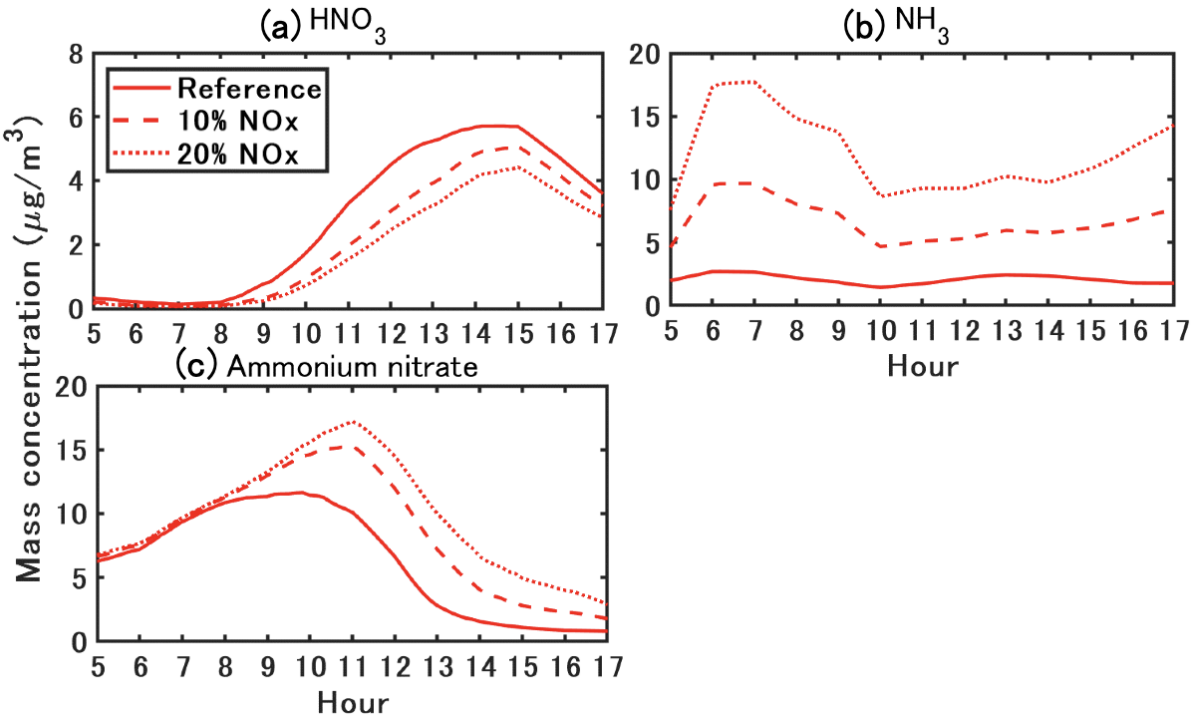

Fig. 2.18 Sensitivity of ammonium nitrate concentration to NH_3 emission.

considering NH_3 emissions of 10% and 20% of NOx emissions leads to a large increase in ammonium nitrate (35% and 55%) compared to the reference case because of the formation of ammonium nitrate by the condensation of HNO_3 and NH_3.

2.2.7 Conclusions

Particles in urban environment impose adverse impacts on pedestrians' health. Conventional CFD methods regarding particles as passive scalars cannot reproduce the formation of secondary aerosols and may lead to uncertain simulations. Therefore, to increase the simulation accuracy of particle dispersion, we coupled the CFD software OpenFOAM (OF) and Code_Saturne (CS) with SSH-aerosol, a modular box model to simulate the evolution of primary and secondary aerosols. The main processes involved in the aerosol dynamics (coagulation, condensation/evaporation, and dry deposition) were considered.

We simulated a 12h transient dispersion of pollutants from traffic emissions in a street canyon using the unsteady RANS model. The simulation domain was generated to model a street canyon where field measurements are available. The flow field was based on the WRF model. The background concentrations of gas and particles were obtained from regional-scale simulations with a chemistry transport model. The particle diameter range (0.01 to 10 μm) was divided into six size sections. The following conclusions were drawn from the results of this study.

1. The simulated spatially averaged values in the street canyon were validated from field mea-

surement using validation metrics. For both OF and CS, the simulated NO_2 and PM_{10} concentrations based on the coupling model (CFD–chemistry) achieved better agreement with the measurement data than the conventional CFD simulation which considered pollutants as passive scalars (CFD–passive). The differences between the OF and CS results were not obvious and were mainly due to the differences in the turbulence scheme. The following conclusions were drawn based on the simulated OF concentrations.

2. For the flow field, a large vortex was observed in the canyon with a small secondary vortex at the corner of the leeward wall at the current aspect ratio (H/W = 0.31). In CFD–chemistry, because of the reverse flow, the 12h (from 05:00LT to 17:00LT) time-averaged NO_2 mass concentration, PM_{10} mass and number concentrations at pedestrian height were much higher near the leeward wall (116, 28, 3.2×10^{10} m^{-3}) than the background (26, 15, 2.3×10^{10} m^{-3}).

3. Secondary aerosol formation largely affected the mass concentration and size distribution of particulate matter. For 12 h time-averaged concentrations, ammonium nitrate and organic matter increased by 46% and 53% in CFD–chemistry compared to CFD–passive because of condensation of HNO_3 and NH_3, background biogenic precursor gases and anthropogenic precursor gas emissions. Coagulation largely influenced the size distribution of small particles by combining particles with a diameter of 0.04–0.16 μm into 0.16–0.4 μm. At the same time, CFD–chemistry showed a much larger concentration than CFD–passive for the particles in 0.16–1.0 μm, indicating that the effect of condensation on increasing mass concentration was dominant compared to other chemical processes.

4. Urban areas are NH_3-limited (HNO_3 sufficient) areas, therefore, increasing NH_3 leads to a large increase in ammonium nitrate. Vehicles are considered to be the main source of NH_3 in urban environments. Increasing the fleet's proportion of recent gasoline vehicles may increase NH_3 emissions. For a 12 h average, we considered NH_3 emissions of 10% and 20% of NOx emissions led to a large increase in ammonium nitrate (35% and 55%) compared to the reference case which considers NH_3 emissions as 1%–2% of NOx emissions.

5. A grid sensitivity analysis showed that the particles' concentrations of inorganic and organic compounds were sensitive to grid resolution, whereas inert particle concentrations were not sensitive to grid resolution. In addition, simulated values based on a grid size of 0.5 m in the street canyon showed small differences with a grid size of 0.25 m, indicating that a spatial resolution of 0.5 m can be enough for reactive particle dispersion at the street level.

6. Operator splitting is often employed to solve the transport term and chemical reactions over a given time step in chemical transport simulations. Two integration orders were considered: A–B splitting method (CFD(Δt)–Chemistry(Δt)) and A–B–A splitting method (CFD($\Delta t/2$)–Chemistry(Δt)–CFD($\Delta t/2$)). The results showed that the A–B–A splitting method had almost the same concentrations as the A–B split- ting method with half the computational time. Further sensitivity analysis on the time step showed that a time step of 0.5 s was enough when using the A–B–A splitting method.

7. Conducting a CFD simulation with constant boundary conditions and emission rates at a specific time point is considered a practical method to achieve time-averaged concentrations for evaluating street-level pollutant concentrations. The validation was conducted using conditions on five time

points (07:00 LT, 10:00 LT, 13:00 LT, 15:00 LT, and 17:00 LT). The simulated concentration based on the above method exhibited almost the same value as the simulation with transient conditions at the same time points.

The limitation of this study should be addressed as several reasonable approximations and assumptions were made in the simulation settings.

1. Concerning the simulation domain, since we focused on the coupling of gas chemical reactions and particle dynamics to the CFD codes, we selected a 12 h period when wind direction was perpendicular to the street. In that case, a 2-D simplification of the simulation domain is reasonable, as shown by Maison, Flageul, Carissimo, Wang, Tuzet and Sartelet (2022). In addition, the 2-D simplification is frequently adopted for studying dispersion of reactive pollutants in a street canyon (Garmory et al. 2009, Wu et al. 2021). However, in more general cases, the pollutant residence time for a 3-D canyon could be shorter compared to the 2-D canyon adopted in this study, and the effects of chemical reaction or aerosol processes could be weaker than this study reported. In addition, various wind directions should be considered to better evaluate the performance of the coupled model. Further work will focus on the application of the coupled model to a complex urban environment with changing wind directions.

2. Concerning the physical model, the simulations were based on RANS closure, and the SSH-aerosol processed the ensemble-averaged concentration, therefore the covariance of turbulent diffusion and chemical reaction may not be fully reproduced. The simulation based on LES may provide better prediction of second-order quantities. In addition, the radiation on the wall may lead to street-level variations of temperature and could affect the flow field and chemical reaction rates. However, this was not considered here, and the radiation effect on the local temperature was simplified as being the same as in the inflow condition. The inflow temperature was obtained from the WRF model where the radiation was considered, and the time variation of temperature was considered to be the same as the background. Future work will be conducted on the influence of environmental factors and emission conditions, aiming to provide knowledge to devise suitable countermeasures to decrease particle concentration in micro-scale urban environments.

2.3 Appendix

2.3.1 Appendix A

The schemes for particle deposition velocity vd were added to the transport equations using volume sink terms based on Zhang et al. (2001) and can be represented as follows:

$$v_{d,p} = \begin{cases} v_g + \frac{1}{R_a + R_s}, & \text{Wall surfaces} \\ v_g, & \text{Entire field} \end{cases} \tag{2.7}$$

$$v_g = \frac{\rho d_p^2 g C}{18\eta} \tag{2.8}$$

$$R_a = \frac{\ln(z_R/z_0) - \psi_H}{\kappa u_*} \tag{2.9}$$

$$R_s = \frac{1}{\varepsilon_0 u_* (E_B + E_{IM} + E_{IN}) R_1} \tag{2.10}$$

The deposition velocity for the particles $v_{d,p}$ consists of both gravitational settling and surface deposition near the wall surfaces. The gravitational settling velocity v_g was considered for the entire field, ρ is the particle density; d_p is the particle diameter; g is the acceleration of gravity; C is Cunningham correction factor for small particles; η is the viscosity coefficient of air. The aerodynamic resistance R_a is calculated from the first-layer height z_R , roughness length z_0, Von Kármán constant κ, friction velocity u_*, and stability function ψ_H. For the k-ε model, u_* is estimated by $(C_\mu^{0.5} k)^{0.5}$ and C_μ = 0.09 is a constant of the model. The surface resistance R_s is calculated from u_*, the collection efficiency from Brownian diffusion E_B, the impaction E_{IM} and the interception E_{IN}. The correction factor represents the fraction of particles that stick to the surface R_1 and an empirical constant ε_0 = 3. The dry deposition schemes for gas were added to the transport equations using volume sink terms based on Wesely (1989) and Zhang et al. (2003b),which can be represented as follows:

$$v_{d,g} = \frac{1}{R_a + R_b + R_c} \tag{2.11}$$

$$R_b = \frac{2}{\kappa u_*} \left(\frac{Sc}{Pr}\right)^{2/3} \tag{2.12}$$

The deposition velocity for gas $v_{d,g}$ is calculated from the aerodynamic resistance R_a, the quasi-laminar layer resistance R_b and the surface resistance for gas R_c; $Sc = \nu/D$ and $Pr = 0.72$ are the Schmidt and Prandtl number; ν is the kinematic viscosity of air, and D is the molecular diffusivity of different gases. R_c is calculated based on Zhang et al. (2003b).

2.3.2 Appendix B

Correctly representing the flow field in the street canyon is important to accurately model the concentrations. Unfortunately, observation data on wind velocity in the street are not available. Therefore, we conducted a velocity validation for OpenFOAM v2012 using data from a wind tunnel experiment (Blackman et al. 2015).

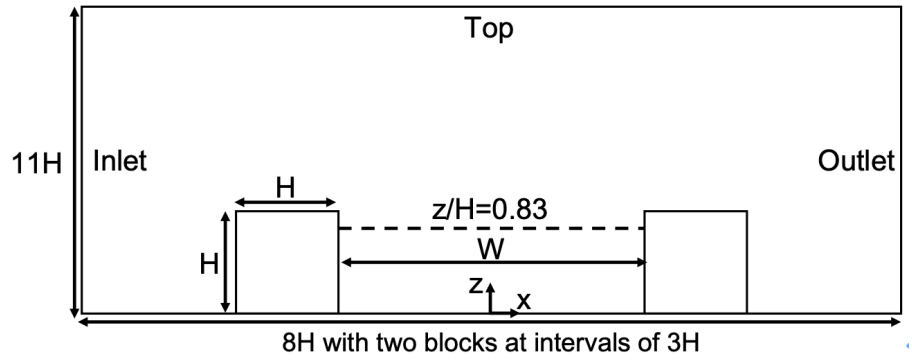

Fig. 2.19 Simulation domain for velocity validation.

The 2-D simulation do- main is shown in Fig. 2.19. The aspect ratio in the experiment (H/W = 0.33) is close to this study (H/W = 0.31). The building height H is 0.06 m. The grid size is 1/20 H in x and z directions in the simulation domain under 3H . The free-stream velocity U_{ref} is 5.9 m s^{-1}. The steady-state flow field is simulated with the same turbulence model (RNG k–ε model) as in the paper, and cyclic boundary conditions are used for the inlet and outlet. The slip boundary is considered for the top, and non-slip boundary conditions with the same wall functions as in the paper are considered for other walls. Figure 2.20 compares the simulated streamwise and vertical direction of mean wind velocities with the experimental values at z/H = 0.83. The RNG k–ε model reproduces the velocities well, although the velocities very close to the windward wall show differences with the experimental values. The above validation shows that if suitable inlet conditions are given, the flow field is well reproduced with the turbulence model adopted in this study.

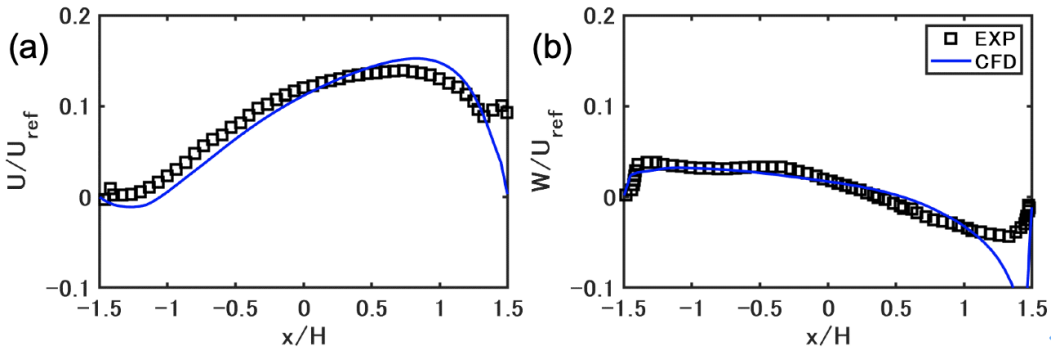

Fig. 2.20 Streamwise and vertical direction of mean wind velocities at z/H = 0.83.

Code and data availability.

The codes and data sets in this publication are available to the community, and they can be accessed by request to the corresponding author.

Author contributions.

KS and RO were responsible for conceptualization. CL, YW, CF, KS, YK, and ZW developed the software. CL and YW conducted the visualization and validation; CL, YW, and KS performed the formal analysis. KS and RO acquired resources. CL, YW, RO, and KS were responsible for writing and original draft preparation. CF, YK, and HK reviewed and edited the paper. All co-authors contributed to the discussion of the paper.

CHAPTER 3

Impact of tree-related processes on the air quality in the street

3.1 Summary

Because of different tree-related processes involved, urban trees have complex impacts on the air quality in streets. In this chapter, the influence of tree-related processes linked to the street ventilation, atmospheric dry deposition, chemical processes and emissions of biogenic volatile organic compounds is studied. Their respective and overall impact on gaseous species and condensables in an urban street canyon is investigated.

The street and the tree crown used in the study are modeled using local-scale simulations performed by the CFD tool Code_Saturne. The tree aerodynamic effects are characterized using the Leaf Area Index (LAI), Crown Volume Fraction (CVF) and tree height to street height ratio (h/H), as detailed in Maison, Flageul, Carissimo, Tuzet, Wang and Sartelet (2022). The impact of the tree trunk is not included in the modeling, only the tree crown part is considered. In Maison, Flageul, Carissimo, Tuzet, Wang and Sartelet (2022), although other tree-related processes such as deposition and chemical reactions are not taken into account, the aerodynamic impact of tree crowns has been parameterized for different tree characteristics and different types of street canyons. This parameterization can be used in simplified street-network models, such as MUNICH.

In this study, the simulations are conducted in the street Boulevard Alsace-Lorraine with the setup detailed in the previous chapter. The width and the height of this street canyon correspond to a wide canyon type. As detailed in Maison, Flageul, Carissimo, Tuzet, Wang and Sartelet (2022), the aerodynamic impact of tree crowns on the horizontal airflow velocity and on the pollutant concentrations is very significant.

Besides of the aerodynamic impact of tree crowns, atmospheric gaseous chemistry, VOC emissions and deposition are also taken into account. Overall, the impact of tree-related chemistry depends on the timescale of pollutant transformation, compared with the time scale of pollutant transport at the street scale. In this context, the characteristic time of pollutant reaction and of pollutant dispersion are calculated and compared in this chapter. Except in the case of low winds, the dispersion of the pollutants in the street is faster than reactions, which results in limited formation of condensables in the presence of trees. Lower wind speed in the street leads to a longer characteristic time of dispersion, and therefore leads to a more significant production of condensables. The formation

of extremely-low volatile organic compounds from autoxidation is significant even when the wind is high. Although its influence on the formation of organic aerosols may be low, it may significantly influence the formation of ultrafine particles.

Apart from the aerodynamic impact and the tree-related chemistry, in this chapter, the atmospheric dry deposition on tree surfaces and on urban surfaces is also studied. Dry deposition is found important only for compounds of high solubility, such as HNO_3, or low volatility.

Based on the above-mentioned tree-related processes, the overall impact of trees is investigated for different types of pollutants, such as traffic-emitted pollutants, oxidants and condensables. Although the simulations are only conducted for gaseous species, the potential influence on the formation of particles is also discussed through the concentration of condensables, providing a more comprehensive understanding of the impact of trees on the air quality in street canyons.

This article has been published in the scientific journal Environmental Pollution, with the doi 10.1016/j.envpol.2023.121210.

3.2 Article

3.2.1 Abstract

Trees grown in streets impact air quality by influencing ventilation (aerodynamic effects), pollutant deposition (dry deposition on vegetation surfaces), and atmospheric chemistry (emissions of biogenic volatile organic compounds, BVOCs). To qualitatively evaluate the impact of trees on pollutant concentrations and assist decision-making for the greening of cities, 2-D simulations on a street in greater Paris were performed using a computational fluid dynamics tool coupled to a gaseous chemistry module. Globally, the presence of trees has a negative effect on the traffic-emitted pollutant concentrations, such as NO_2 and organic condensables, particularly on the leeward side of a street. When not under low wind conditions, the impact of BVOC emissions on the formation of most condensables within the street was low owing to the short characteristic time of dispersion compared with the atmospheric chemistry. However, autoxidation of BVOC quickly forms some extremely-low volatile organic compounds, potentially leading to the formation of ultra-fine particles. Planting trees in streets with traffic is only effective in mitigating the concentration of some oxidants such as ozone (O_3), which has low levels in cities regardless of this, and hydroxyl radical (OH), which may slightly lower the rate of oxidation reactions and the formation of secondary species in the street.

3.2.2 Introduction

Urban air pollution is an important global issue and has been reported as being responsible for almost nine million premature deaths in 2015 (Forouzanfar et al. 2016, Landrigan et al. 2018). Observations of high concentrations of nitrogen dioxide (NO_2) and particulate matter (PM) of aerodynamic diameters lower than 2.5 µm and 10 µm ($PM_{2.5}$ and PM_{10}) in urban streets have been attributed to

traffic emissions and reduced atmospheric ventilation (Gottlicher et al. 2010, Thorpe and Harrison 2008, Markku 2015). As these pollutants have adverse health effects (Speizer et al. 1980, Weinmayr et al. 2010, WHO 2021) and human exposure to outdoor pollution is high due to the pollutants' high concentrations (Lugon et al. 2022), improving street-level air quality is beneficial for human health (Finkelstein and Jerrett 2007, Chen et al. 2017, Yuchi et al. 2020).

Planting vegetation along streets is considered an effective method to mitigate air pollution. However, the impact of trees on the air quality within urban street canyons is subject to complex processes. The presence of trees affects street ventilation and changes pollutant dispersion (Gromke and Ruck 2007, Buccolieri et al. 2009, Abhijith et al. 2017), leading to high concentrations of pollutants emitted by traffic, such as NO_2 and PM (Vos et al. 2013). However, trees can absorb pollutants and retain them via deposition (Nowak et al. 2006, Currie and Bass 2008, Escobedo et al. 2011). The deposition velocity varies with the vegetation type and the different pollutants (Buccolieri et al. 2009), depending on both the reactivity and the Henry's Law constant of the pollutant (Wesely 1989). Several models have been developed to evaluate the deposition effects from simple constant deposition velocity models (Nowak et al. 2006, 2013, Pugh et al. 2012, Baraldi et al. 2019) to more complex models that estimate the deposition velocities as the inverse of the sum of resistances (Baldocchi et al. 1987, Hirabayashi et al. 2012, Cabaraban et al. 2013, Selmi et al. 2016). In addition, the presence of trees in streets can affect atmospheric chemistry. Trees emit biogenic volatile organic compounds (BVOCs), which may lead to the formation of O_3 in cities (Calfapietra et al. 2013, Churkina et al. 2015, 2017), because the chemical regimes of cities are usually VOC-limited (Sartelet et al. 2012, Seigneur 2019), however, this may be minimal at the street scale where O_3 concentrations are generally quite low (Kwak and Baik 2014). Furthermore, BVOC emissions may lead to the formation of PM (Churkina et al. 2017). BVOCs may be oxidized by O_3 and radicals such as hydroxyl (OH) to form organic condensables (Seigneur, 2019). Condensable species are gaseous compounds that may condense onto particles depending on the environment. Organic condensables also have an anthropogenic origin and may be emitted directly by traffic (Sartelet et al. 2018).

To study the combined effects of these tree-related processes, various numerical modeling techniques have been developed, ranging from simple street models (Maison, Flageul, Carissimo, Tuzet, Wang and Sartelet 2022, Lugon et al. 2020b) to more complex Computational Fluid Dynamics (CFD) models. CFD models are powerful tools for estimating pollutant concentrations and fluxes at small scales (with feasible grid refinement less than 1 m). Pollutants are treated as passive scalars in most CFD models due to the high impact of atmospheric and morphological conditions, and chemical reactions are not considered (Zhang et al. 2020). This may lead to an underestimation of pollutant concentrations, particularly for NO_2 and organic condensables (Lugon et al. 2020b). Therefore, chemical models are coupled with CFD models to represent the transport of pollutants and their interactions (Baker et al. 2004, Grawe et al. 2007, Baik et al. 2007, Kikumoto and Ooka 2012, Liu and Leung 2008, Garmory et al. 2009, Kwak and Baik 2012, Kwak et al. 2013, Zhong et al. 2014). Most chemical models have been designed originally for O_3 formation and so often ignore condensable formation (Kim et al. 2011).

In this study, a modified version of the chemical mechanism CB05 (Yarwood et al. 2005) that considers the formation of condensables (Chrit et al. 2017, Sartelet et al. 2020) was coupled to a RANS (k-ε) turbulence model to investigate air quality in a street canyon, focusing on the two-dimensional flow in the vertical cross-section (Vardoulakis et al. 2003). As the physico-chemical processes linked to the presence of trees in street canyons have antagonistic impacts on air quality (circulation, deposition, and chemistry), the objective of this study is to evaluate their relative and overall impacts to provide guidance to aid decision-making with respect to the greening of cities. The model is presented in the second section. Sensitivity tests are undertaken and the results are presented in the third section to qualitatively evaluate the impacts of the different tree-related processes. The influence of these processes on atmospheric compounds, such as NO_2, CO, and inorganic and organic condensables, is discussed to provide a qualitative estimation of the local-scale impact of trees on the mitigation of air pollutants in street canyons.

3.2.3 Methodology

CFD simulations were performed with Code_Saturne (Archambeau et al. 2004, Milliez and Carissimo 2007) using the RANS approach with a k-ε linear production for turbulence (Guimet and Laurence 2002). The gas-phase mechanism, coupled with the CFD model, is a modified version of CB05 (Yarwood et al. 2005) which considers condensables (Sartelet et al. 2020).

3.2.3.1 Domain of study

The street canyon "Boulevard Alsace-Lorraine" (in east Paris), as discussed in Kim et al. (2018a), was modelled by a two-dimensional regular grid with a resolution of 0.5 m. The geometry of the model corresponded to the average aspect ratio of the street. Figure 3.1 shows the domain used in the simulation. The canyon height (H) was 8.5 m, and the width (W) 27.5 m, corresponding to a moderate aspect ratio of 0.31 (Sini et al. 1996, Lugon et al. 2020b). Trees were located on both sides of the street and were placed every 10 m along the street's length. The center of the crown was placed at a height of 6 m and extended along the street length, with crown radius of 3 m. The tree canopy structure was described by the leaf area index (LAI), which is a commonly-used indicator of the number of leaves for different types of vegetation. As the model was 2-D, the crown of trees was modelled as a cylinder and the LAI 3-D of the vegetation converted to LAI 2-D (Maison, Flageul, Carissimo, Tuzet, Wang and Sartelet 2022). The roadway, determined as the traffic zone, was placed between the trees, as shown by the striped zone in Figure 3.1. The height of the vehicle zone, where the traffic produced turbulence mixes and diluted traffic emissions, was assumed to be 1.5 m according to Solazzo et al. (2008) and Niroomand et al. (2021). The inlet was set at the lower x boundary (left, Figure 3.1) and at the top of the domain. The outlet was set at the upper x boundary of the domain (right, Figure 3.1).

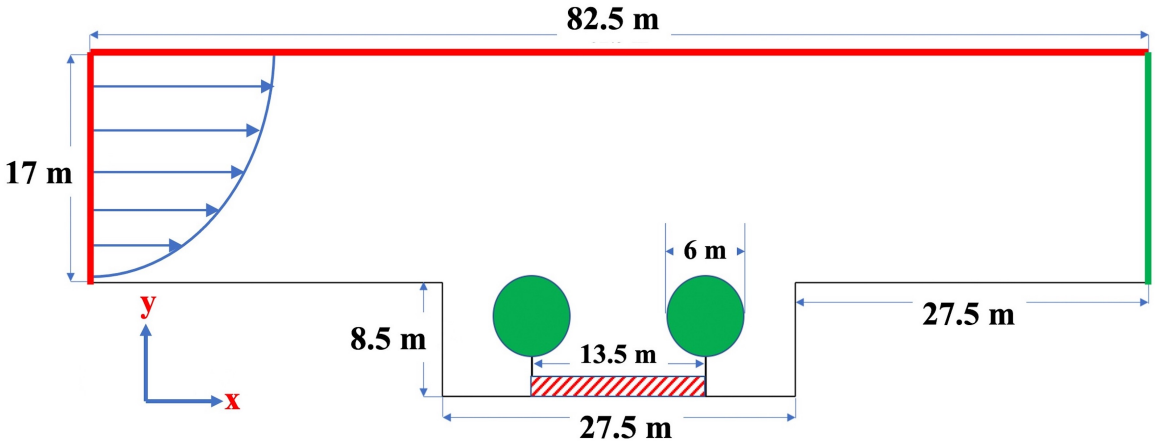

Fig. 3.1 Simulation domain. Tree crowns are cylindrical, as shown in green. Between the trees, the traffic zone is modelled as a surface source, as shown by the red stripe lines.

3.2.3.2 Air flow around trees

In areas covered by trees, the turbulent flow was computed using a porosity model (Zaidi et al. 2013). The canopy of trees exerted an aerodynamic drag force on the flow, which reduced the speed and changed the turbulence structure. It was modeled by a source term in the momentum and turbulence equations, which are detailed in section 1.1 in the supplementary materials.

3.2.3.3 Emissions from traffic and vegetation

CO, NH_3, NOx and VOC emissions from traffic exhaust (Kim et al. 2022) and monoterpene and isoprene emissions from trees were considered in the model. Hourly-varying traffic emissions were those reported by Kim et al. (2022) and relied on emission factors from the COPERT methodology (COmputer Program to calculate Emissions from Road Transport, version 2019, EMEP/EEA, 2019). The characteristics of the Japanese pagoda tree (Styphnolobium japonicum), a common species in Paris known widely as "Sophora Japonica" were used, with a 2-D LAI of 4 $m^2.m^{-2}$. Isoprene (ISOP) and monoterpenes (α-pinene API, β-pinene BPI and limonene LIM) account for the largest fraction (Guenther et al. 1995) of VOCs emitted by trees and therefore were the only emissions considered. The emissions were modelled using standard parameterizations, as detailed in section 1.3 in the supplementary materials.

3.2.3.4 Dry deposition

Gaseous pollutants can be deposited on urban surfaces such as streets, building walls and vegetation. Deposition on urban surfaces is achieved by imposing a mass flux on the boundary faces, while deposition on vegetation surfaces is achieved by using a sink term in the transport equation, as detailed in section 1.2 in the supplementary materials.

The formulations used to represent dry deposition on urban surfaces were based on Chérin et al. (2015), Hicks et al. (1987) and Wesely (1989). Deposition on trunks was ignored because gaseous pollutants are mainly affected by leaves in the tree canopy. The deposition velocity on trees was estimated using surface resistance and the quasi-laminar layer resistance (Wesely 1989, Erisman et al. 1994).

3.2.3.5 Boundary conditions

As the simulation domain is small and low in height, the atmosphere was assumed to be neutral. The wind from the inlet was assumed to be unidirectional and perpendicular to the direction of the street, as shown in Figure 3.1. The wind profile at the inlet above the street canyon was assumed to follow the semi-empirical logarithmic function:

$$u_x = \frac{u_*}{\kappa} \times \log\left(\frac{z - H + z_0}{z_0}\right), \tag{3.1}$$

where u_* is the friction velocity, κ is the Von Karman constant (0.42), H is the building height (8.5 m), and z_0 is the surface roughness of the building roof. The turbulent kinetic energy k and dissipation rate ε at the inlet are calculated as follows:

$$k = \frac{u_*^2}{\sqrt{C_\mu}} \text{ and } \varepsilon = \frac{u_*^3}{\kappa(z - H + z_0)} \text{ with } C_\mu = 0.09. \tag{3.2}$$

The time-varying inflow was driven by the meteorological parameters. Hourly-varying meteorological conditions (friction velocity ($m\ s^{-1}$), temperature (K), and specific humidity ($g\ kg^{-1}$)) and the background concentrations of the gas-phase compounds above the street were obtained from the regional-scale simulations of Sartelet et al. (2018). At each time step, a linear interpolation provided inlet profiles.

3.2.3.6 Model parameters

Surface roughness (z_0) was detailed for different urban surfaces, set at 1 m on roof surfaces (Wiernga 1993), and 0.1 m on walls and road surfaces in the canyon, considering the urban furniture (windows, balconies, pavements, etc).

The turbulent dispersion of pollutants is described by the turbulent Schmidt number (Sc_t) under the simple gradient diffusion hypothesis. According to Tominaga and Stathopoulos (2007), Sc_t ranges between 0.2 and 1.3, and the optimum choice of this parameter depends on the local flow characteristics. In this study, the best model for measurement comparison was obtained with $Sc_t = 0.4$. The model without trees was evaluated by comparing the simulated concentrations of NO_2 and PM_{10} to measurements for a day in April reported by Lin et al. (2022).

3.2.3.7 Case study

Tree-related processes (VOC emissions by trees, atmospheric dry depositions, and aerodynamic effects of tree crowns) and chemical reactions influence the evolution of concentrations in the street. Simulations were performed for a few hours in July, when the temperature and tree VOC emissions were high, and also for a few hours in April, when NO_2 measurements were available (Lin et al. 2022).

Table 3.1 List of simulations and their configurations

Case id	BVOC emissions	Dry deposition on urban surfaces	Dry deposition on vegetation surfaces	Date	Tree
ref_A / ref_J	no	yes	no	April / July	no
0_J	no	yes	no	July	yes
1_A / 1_J	yes	yes	yes	April / July	yes
2_J	no	yes	yes	July	yes
3_J	yes	no	yes	July	yes
4_J	yes	yes	no	July	yes

Table 3.1 lists the simulations and adopted configurations. In the reference cases for April (case ref_A) and July (case ref_J), trees were not considered. In case 1_J and 1_A, all trees-related processes were considered, while case 0_J only considered the aerodynamic effect. Sensitivity tests were performed and analyzed by comparison with case 1_J, except for the aerodynamic effect, which used case 0_J as the reference case. In each sensitivity test, one process was ignored (case 2_J for BVOC emissions, case 3_J for dry deposition on urban surfaces, and case 4_J for dry deposition on vegetation surfaces), as detailed in Table 3.1. The difference between the two simulations was quantified using the relative deviation (RD_{C_i}) of the spatially averaged street concentration of the street (from the ground to the roof level), which is defined as follows:

$$RD_{C_i} = \frac{C_i - C_i\_0}{C_i\_0} \times 100\% \tag{3.3}$$

where C_i represents the average street concentration in a sensitivity test and C_i_0 represents the average street concentration in the reference case.

Each sensitivity simulation lasted 3.5 h, on July 18, 2014 (or on April 30, 2014) from 2.30 p.m. to 6 p.m. (local Paris time, GMT+2), with a constant time step of 1 s. The first 30 min corresponded to the model spin-up time, and the analysis was performed for the remaining 3 h.

The impact of tree-related processes was assessed for several gaseous species, including those

emitted by traffic (NO, NO_2, NH_3, and CO), O_3, radical OH, and condensable HNO_3 (which may condense with NH_3 to form inorganic particles of ammonium nitrate). For organic compounds, three groups of organic condensables were studied: biogenics, formed from the oxidation of monoterpenes and isoprene (Bio. cond.), anthropogenics, formed from the oxidation of xylenes and toluene (Ant. cond.), and anthropogenic intermediate, semi-, and low-volatility organic compounds (ISVOC), which are directly emitted by traffic and oxidized in the atmosphere.

The characteristic times of dispersion and reaction were calculated to compare the dispersion rate with the chemical reaction rates. For dispersion, the street-average concentration was assumed to evolve following an exponential function for a transient period under constant wind conditions as follows:

$$C(t) = C_0 + (C_\infty - C_0)\left(1 - \exp\left(-\frac{t}{\tau_D}\right)\right) \tag{3.4}$$

where C_0 is the initial street concentration of a compound, C_∞ is the concentration at the end of the transient period, and τ_D is the characteristic dispersion time.

The characteristic reaction time τ_R considers the production/consumption of a reactive compound by different chemical reactions. This is approximated as follows:

$$\tau_R = \frac{\overline{C}}{|R_P - R_C|} \tag{3.5}$$

where $\overline{C}$ is the average concentration, R_P is the production rate, and R_C is the consumption rate.

3.2.4 Results

The impacts of different tree-related processes on the evolution of concentrations were estimated. The processes involve tree VOC emissions, dry deposition on vegetation and urban surfaces, and aerodynamic influence of tree crowns on the dispersion. Finally, the overall impact of these processes on the pollutant concentrations in the streets was evaluated. Table 3.2 illustrates the impact of different processes using the relative deviation of the street-averaged concentrations (RD_{C_i}) between the two simulations.

3.2.4.1 Impact of tree VOC emissions

Tree VOC emissions had a limited impact (lower than 1%) on the gas-phase reactive compounds: NO, NO_2, and O_3. However, the street-averaged concentration of radical OH was significantly reduced by approximately 17%. The production of O_3 by the tree VOC emissions was low in the high-NOx chemical regime of the street (approximately 0.2%). Therefore, the production of OH by O_3 photolysis was low. The OH concentration decreased because it was consumed by the VOC emitted by the trees. The evolution of NO_2, OH, and the chemical regime are detailed in Figures 1 and 2 in the supplementary materials.

Table 3.2 Summary of tree impacts on the street-average concentrations of different species in the street. The column Ref. corresponds to the average concentrations of the case 1_J. The columns VOC, Dep urb, Dep tree, Aerodyn. and Synth. correspond to the impact of VOC emissions, deposition on urban surfaces, deposition on trees, aerodynamic effects and overall effects, respectively.

Species	Ref. 1_J μg m^{-3}	VOC % (2_J - 1_J) %	Dep urb (3_J - 1_J) %	Dep tree (4_J - 1_J) %	Aerodyn (ref_J - 0_J) %	Synth July (ref_J - 1_J) %	Synth April (ref_A - 1_A) %
NO	22.0	0.9	-0.4	-0.9	**-27.5**	-27.6	-27.8
NO_2	42.3	-0.7	1.5	3.5	**-23.8**	-21.5	-16.1
NH_3	2.8	0.0	1.2	3.6	-6.3	-2.0	-9.0
CO	158	0.0	0.0	2.2	**-10.5**	-8.7	-7.3
HNO_3	2.6	0.7	5.9	**25.0**	0.3	21.8	26.2
O_3	82.5	-0.3	0.9	3.2	6.1	8.8	10.7
OH	3.1×10^{-4}	**17.4**	-0.4	-1.4	**13.6**	26.4	9.0
Bio cond.	4.3	-0.2	0.0	0.0	0.0	-0.2	-0.1
ELVOC	1.6×10^{-4}	**-73.9**	0.7	2.4	**-14.3**	-78.0	-55.1
Ant cond.	0.8	0.1	0.0	-0.01	-0.2	-0.1	-0.2
ISVOC	5.5	0.04	0.1	0.7	**-15.0**	-14.1	-16.7

This decrease in OH also resulted in a slight decrease in HNO_3 (0.7%), which was formed from the oxidation of NO_2. This low decrease in HNO_3 most likely has a low impact on inorganic aerosol concentrations.

For organic compounds, the monoterpene and isoprene concentrations increased substantially owing to tree VOC emissions, reaching on average 467% and 5,000%, respectively, over the simulation period. Monoterpene and isoprene were oxidized to form biogenic organic condensables (see Figure 3 in the supplementary materials). However, tree VOC emissions had a low impact on the mass of organic condensables at the local scale (Table 3.2). In the model, a representation of the condensable formation was built from chamber experiments with a limited number of model species. The formation of condensables was simplified by only one oxidation step of the precursor. The oxidation characteristic time was typical of what was observed in chambers, but it might not represent the fast-forming compounds, such as those produced from autoxidation (Ehn et al. 2014), which were only modelled in this study for the autoxidation of monoterpenes. For monoterpenes, one oxidation step by O_3, NO_3 and OH directly leaded to the formation of modelled condensables (of note, BiA0D, BiA1D, BiA2D, BiNIT, Monomer and Dimer). Only the formation of extremely-low volatile compounds (ELVOC) with very low saturation vapor pressure (Ehn et al. 2014), from monoterpene autoxidation, which was represented by two model species (Monomer and Dimer), was enhanced because it involved fast reacting radical species. Although the ELVOC concentrations largely increased (by 276% on average), they were low compared to other organic concentrations, with a maximum of

1.5×10^{-4} μg.m^{-3}. Panels (a) and (b) of Figure 3.3 show the spatial distribution of the time averaged ELVOC concentrations. This increase was mostly near the leeward side of the street.

For isoprene, biogenic condensables were modelled as for monoterpenes, from the limited number of model species in chamber experiments. Some of these species were produced from the oxidation of intermediate products such as isoprene nitrates (ISON), first-order OH reaction products of isoprene (ISOR), methacrolein (MACR) and methacryloyl peroxynitrate (MPAN). Although the concentrations of these intermediate products largely increased with tree VOC emissions (ISON +47.39%, ISOR +1195.18%, MACR +1101.37% and MPAN + 136.17%), the formation of condensables was not significantly affected.

Owing to the long time required for monoterpenes and isoprene to undergo oxidation in the atmosphere (Seigneur 2019), secondary organic condensables did not seem to have sufficient time to form in the street, except for those formed from autoxidation. A better representation of the fast-forming condensables from radicals is desirable to determine more accurately the influence of monoterpenes and isoprene emissions on condensable concentrations.

3.2.4.2 Impact of VOC emissions in the street with low-wind speed

Although some intermediate oxidized species, such as MACR and MPAN were significantly produced with the addition of tree VOC emissions, the production of condensables was limited because of the long time required for the oxidation reactions to complete. To illustrate this, the characteristic times of the OH reactions, τ_R, and the dispersion of the flow, τ_D, were compared.

The concentration of CO was used for the calculation of τ_D because of its low reactivity. τ_D was estimated to be approximately 32 s. For OH, τ_R was approximately 86 s with tree VOC emissions and 154 s without tree VOC emissions, i.e., it is at least twice the characteristic time of dispersion, highlighting the low value of the characteristic time of dispersion.

This low characteristic time of dispersion may be due to the high wind speed at the inlet of 5 m.s^{-1} at 25 m. With a lower wind speed of 0.7 m.s^{-1} at 25 m, the characteristic time of dispersion was 186 s. To assess the effect of wind speed, two more sensitivity tests with the same configuration as cases 1_J and 2_J were conducted at low wind speeds (cases 5_J and 6_J). Figure 3.2 compares the condensable concentrations from the oxidation of monoterpenes and isoprene, when tree VOC emissions were considered or not under high- and low-wind speed conditions. The production of condensables was more significant in the low-wind speed condition than in the high-wind speed condition, with a time-averaged increase of approximately 5% for monoterpene condensables and 7% for isoprene condensables, compared to less than 1% for both under the high-wind speed condition.

3.2.4.3 Atmospheric dry deposition

To evaluate the impact of atmospheric dry deposition, case 1_J, which considered dry deposition on both urban and vegetation surfaces (tree crowns), was compared to cases 3_J and 4_J, which considered only urban and vegetation surfaces, respectively. Here, urban surfaces refer to the building

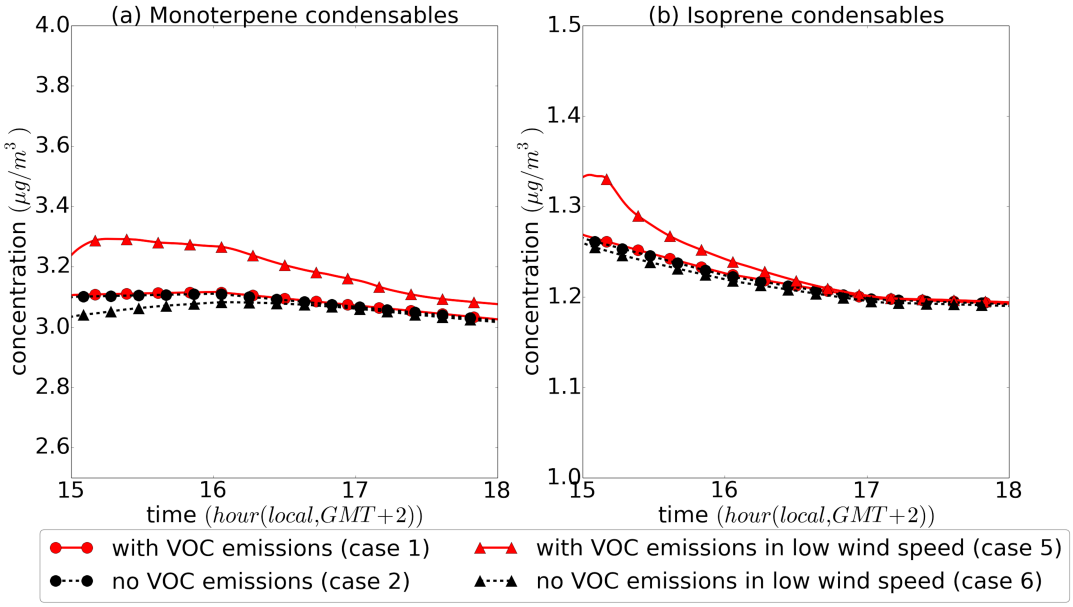

Fig. 3.2 Condensable concentrations in high-wind speed and low-wind speed conditions, (a) condensables from monoterpene, (b) condensables from isoprene.

walls and the ground in the canyon. The impact varies with species due to properties such as solubility (Henry coefficient) and volatility.

For all species studied, the impact of deposition on urban surfaces was low (less than 1%, except for HNO_3 (6%)). For most species, the deposition on vegetation surfaces was slightly higher than that on urban surfaces, but it remained low (lower than 4%). However, as is shown in Figure 4 in the supplementary material, HNO_3 is shown to be more affected by deposition due to its high solubility, particularly on leaf surfaces. This resulted in a significant reduction in HNO_3 concentrations (25%), which may restrain the gas/particle partitioning and the formation of secondary aerosols.

3.2.4.4 Aerodynamic impact of tree crowns

A comparison of the flow fields in Figure 5 in the supplementary material shows that, in general, the presence of trees reduced the turbulent viscosity in the canyon, which indicates that the turbulent dispersion of pollutants was reduced. The characteristic time of dispersion increased from 21 to 32 s with the trees present, under which conditions the horizontal wind velocity was higher in the middle and near the windward side of the street, and lower on the leeward side. This indicates that the residence time was higher on the leeward side, which was more prone to pollutant accumulation.

The variation in the flow field affects both the dispersion of pollutants and their concentrations. Table 3.2 shows that the aerodynamic effect of tree crowns significantly increased the street average concentration for species emitted by traffic (NO, NO_2, CO, NH_3, ISVOC). Owing to the presence of tree crowns, species were less dispersed and accumulated more in the traffic zone, resulting in a higher street average concentration. However, the aerodynamic effect of tree crowns significantly reduced the concentrations of reactive oxidants in the atmosphere, such as O_3 and OH radical, because these

species were more consumed by reactions with traffic exhaust emissions such as NO.

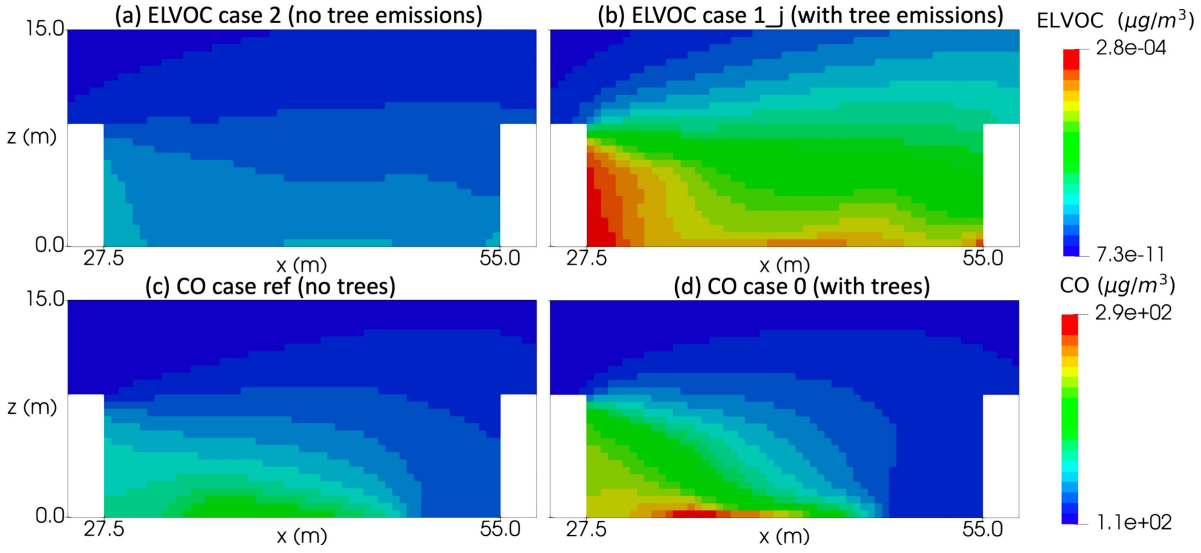

Fig. 3.3 Temporally-averaged concentration of ELVOCs (panels (a) and (b)) and CO (panels (c) and (d)) in and above the street.

To analyze the aerodynamic effect of tree crowns on spatial distribution, CO is studied, because it is relatively unaffected by the chemistry at the urban scale (Seigneur 2019) compared to other species. Panels (c) and (d) of Figure 3.3 present the CO concentration in and above the street with and without tree crowns. The CO concentration was much higher in the street than in the background above the street, due to traffic emissions, regardless of the presence of trees. The highest concentration was observed on the leeward side of the street because of the reverse flow. Trees led to a significant increase in concentrations near the leeward side, and a small decrease near the windward side. The presence of trees accentuated the concentration differences between the leeward and the windward sides.

3.2.4.5 Overall impact of trees

The overall impact of trees was evaluated by comparing the Case ref (without trees) and the Case 1 (with trees) for both April and July (Table 3.2). The presence of trees led to a large increase in the concentrations of NO, NO_2, CO and ISVOC emitted by traffic, mainly due to the aerodynamic effects. The overall impact was similar in April and in July. The increase ranged from 7% for CO to 28% for NO.

The presence of trees led to a large decrease in the concentrations of the oxidants O_3 and OH, by 9%-11% and 9%-26%, respectively. O_3 concentrations were low in streets because of the traffic emissions of NOx. The decrease of O_3 and OH were both partly due to the increase in NOx (aerodynamic effect), but also due to the dry deposition for O_3 and tree VOC emissions for OH. Owing to the high wind speed in the canyon, this decrease in oxidant concentrations had a very low impact on organic condensables, which were almost not modified by trees, except for ISVOCs, because they

were directly emitted by traffic.

From those results, it can be inferred that the presence of trees likely leads to an increase in particle concentrations in the street, as particles are directly emitted by traffic and would accumulate due to aerodynamic effects. Furthermore, the increase in organic condensables at low wind speeds may lead to the formation of organic particles. The evolution of inorganic particles is less clear, as it depends on the evolution of inorganic condensables and the limiting factor for the formation of ammonium nitrate, i.e., HNO_3 or NH_3 concentrations. These evolved in the opposite direction, with the HNO_3 concentrations reduced by trees (by 22% to 26%) because of dry deposition on leaf surfaces, while NH_3 increased because it was emitted by traffic.

3.2.5 Conclusions

In this study, the effects of trees on gaseous species and condensable concentrations in a street canyon were investigated by a coupled CFD-gas-chemistry model to evaluate the impact of trees on mitigating pollutant concentrations.

Different gaseous species are sensitive to various tree-related processes. Trees grown in streets cannot mitigate the concentrations of pollutants emitted by traffic because the aerodynamic effect dominates. The pollutant concentrations accumulate at the pedestrian level near the leeward side of the street. For oxidants, trees reduce the average concentrations of O_3 and OH radicals, thereby decreasing the formation of secondary species. However, this decrease is not very important for the formation of condensables, and O_3 concentrations are low in streets regardless of this. The concentrations of organic condensables increase slightly due to the oxidation of tree-emitted VOC, especially on the leeward side, while the formation of ELVOC from autoxidation is enhanced, potentially leading to the formation of ultra-fine particles. For inorganic condensables, the impact of vegetation is balanced, with HNO_3 reduced owing to the dry deposition effect on tree leaves, while NH_3 increased due to the aerodynamic effects of trees.

In this study, the geometry of the street canyon was simplified to a 2-D representation with a perpendicular wind direction. However, further studies with a more realistic 3-D geometry-based model and more complex street networks are important to acquire conclusions more representative of individual districts, alongside with a field measurement campaign to provide a robust validation. The radiative effects of trees and the aging of tree-emitted VOCs at the regional scale should also be considered in future models.

Research data

The code and data that used in this study is openly available in `https://doi.org/10.5281/zenodo.7180003`.

Acknowledgements

We would like to thank Marc Dufresnoy, Toshiki Kurohata and Antoine Journain De Muizon for their contributions to this study, and Youngseob Kim and Lya Lugon for providing traffic emissions and boundary conditions. The authors acknowledge funding from DIM QI^2 (Air Quality Research Network on air quality in the Île-de-France region), from the Île-de-France region and from the sTREEt ANR project (ANR-19-CE22-0012).

3.3 Supplementary materials

3.3.1 Governing equations

The existence of traffic and trees in the street affect the flow and dispersion of atmospheric chemical species. In addition, traffic is an important source of emissions in the street canyon. Furthermore, trees also release VOC emissions. These elements are considered as source terms to be added in the governing equations, to study the influence on the evolution of pollutants.

3.3.1.1 Porosity model

$$S_{u,i} = -\frac{1}{2}\rho\alpha C_D|U|\overline{U_i} \tag{3.6}$$

where α is the leaf area density (m^2/m^3); C_D is the drag coefficient of the canopy. This coefficient varies from 0.1 to 0.3 for different types of trees (Fesquet et al. (2009)). Here, it is chosen to be 0.2. $|U|$ is the local mean velocity magnitude and U_i is the i^{th} component of the wind vector.

The effect of trees on turbulence is modeled by source terms S_k and S_ε in the $k-\varepsilon$ equations as follows:

$$S_k = \frac{1}{2}\rho\alpha C_D\beta_p|U|^3 - \frac{1}{2}\rho\alpha C_D\beta_p|U| \tag{3.7}$$

and

$$S_\varepsilon = \frac{\varepsilon}{k}C_{4\varepsilon}\rho\alpha C_D|U|^3 - C_{5\varepsilon}\beta_d k|U| \tag{3.8}$$

Where $C_{4\varepsilon}$, $C_{5\varepsilon}$, β_d and β_p are model constants. $\beta_p = 1$ (Sanz (2003), Katul et al. (2004)), the other constants are calculated as $C_{4\varepsilon} = C_{5\varepsilon} = 0.9$, $\beta_d = 5.03$.

3.3.1.2 Dry deposition of pollutants

The ability of deposition of a given pollutant depends on its dry-deposition velocity v_d, which is defined as the inverse of the sum of resistances:

$$v_d = \frac{1}{R_a + R_b + R_c} \tag{3.9}$$

where R_a, R_b and R_c are resistances to the atmospheric flow, to the air layer above the surface and to the surface, respectively.

- Deposition velocity on urban surfaces

Buildings, streets and other surfaces in the street canyon contribute to the deposition. To model the dry deposition on urban surfaces, the aerodynamic resistance R_a can be represented as Chérin et al. (2015):

$$R_a \approx \frac{1}{K_t^c} \times z \tag{3.10}$$

where z is the distance between the center of the cell near the surface and the surface, the turbulent mass diffusivity K_t^c is estimated from the turbulent viscosity ν_t and the turbulent Schmidt number Sc_t:

$$\frac{\nu_t}{K_t^c} = Sc_t. \tag{3.11}$$

The choice of the turbulent Schmidt number is controversial, especially in urban areas. It is usually chosen between 0.2 and 1.3 (Tominaga and Stathopoulos 2007). In the present study, a value of 0.4 is used.

The quasi-laminar layer resistance R_b is obtained by the empirical equation (Hicks et al. 1987):

$$R_b = \frac{2}{\kappa u_*} \left(\frac{S_c}{P_r} \right)^p \tag{3.12}$$

where κ is the Von Karman constant (0.42); u_* is the friction velocity; S_c is the Schmidt number, which is defined as $S_c = \nu / D_i$, with ν the kinematic viscosity of air ($0.15\ cm^2 s^{-1}$) and D_i the molecular diffusivity of the pollutant; $P_r = 0.74$ is the Prandtl number for air, the exponent p is taken equal to $\frac{2}{3}$ following Baldocchi et al. (1987).

Modelling the surface resistance R_c is often challenging (Baldocchi et al. 1987). In the present study, R_c is taken equal to the urban ground resistance parameter R_{gs} of Wesely (1989). Table 3.3 shows the ground resistance of SO_2 and O_3 for urban areas during the different seasons of a year.

Table 3.3 Ground resistance R_{gs} for SO_2 and O_3 in different seasons (from Wesely (1989))

Seasonal category	SO_2	O_3
Mid summer	400	300
Autumn	400	300
Late autumn	400	300
Winter	100	600
Transitional spring	500	300

For other species, their ground resistance ($R_{gs,i}$) can be computed on the basis of two key parameters: their Henry constant H_i^* and reactivity $f_{0,i}$:

$$R_{gs,i} = \left[\frac{H_i^*}{10^5 R_{gsSO_2}} + \frac{f_{0,i}}{R_{gsO_3}} \right]^{-1} \tag{3.13}$$

Finally, the deposition velocity v_d (m/s) is estimated from the resistances R_a, R_b and R_c, and the deposition on urban surfaces is achieved by imposing a flux F (mg/s) on the boundary surfaces:

$$F = \rho * C_{species} * v_d * \sum S_{wall}, \tag{3.14}$$

where ρ is the density of the flow near the surface, $C_{species}$ (ppm) is the species mass fraction, S_{wall} (m^2) is the wall surface. The surfaces included in the simulations are building walls and the street.

- Deposition velocity on vegetation surfaces

Vegetation canopies are considered as rough surfaces, where the aerodynamic resistance R_a is usually small (Erisman et al. 1994). The deposition velocity on leaf surfaces is therefore estimated as the inverse of the quasi-laminar layer resistance R_b and the bulk surface resistance R_c.

The model of Wesely (1989), Zhang et al. (2002b, 2003b) for decidious forest is adapted to calculate R_c, which depends on the leaf stomatal resistance R_s, the mesophyll resistance R_m and the leaf cuticular resistance R_{lu}:

$$R_c = \frac{1}{\frac{1}{R_s+R_m} + \frac{1}{R_{lu}}} \tag{3.15}$$

The bulk canopy stomatal resistance for species i (R_s^i) computes mass transfer due to the diffusion through stomatal apertures which may exist on one or both sides of the leaves, and is approximated from the stomatal resistance of water vapor ($R_s^{H_2O}$) and their diffusivities (D_{H_2O} and D_i):

$$R_s^i = R_s^{H_2O} \frac{D_{H_2O}}{D_i} \tag{3.16}$$

where the stomatal resistance for water is defined by:

$$R_s^{H_2O} = R_i(1 + (200(G + 0.1)^{-1})^2)(400(T_s(40 - T_s))^{-1}) \tag{3.17}$$

where R_i ($s.m^{-1}$) is the minimum bulk canopy stomatal resistance for water vapor (see Table 3.4), G is the solar irradiation in Wm^{-2}. T_s is the surface air temperature, taken to be 35 $^\circ C$ in the summer simulation and 20 $^\circ C$ in the spring simulation, averaged from simulation period.

Table 3.4 Minimum bulk canopy stomatal resistance R_i and culticular resistances for SO_2 and O_3 in different seasons (from Wesely (1989), Zhang et al. (2002b))

Seasonal category	R_i	$R_{lu}^{SO_2}$	$R_{lu}^{O_3}$
Mid summer	70	1200	1200
Autumn	-	2000	2000
Late autumn	-	9000	9000
Winter	-	-	-
Transitional spring	140	2000	2000

For dry leaf surfaces, the leaf cuticular resistance for a pollutant i is computed as:

$$R_{lu}^i = (\frac{\alpha_i}{R_{lu}^{SO_2}} + \frac{\beta_i}{R_{lu}^{O_3}})^{-1} \tag{3.18}$$

where α_i and β_i for species i are parameters derived from the observation of its dry deposition velocity. SO_2 and O_3 are chosen as basic species and their cuticular resistances in different seasons are shown in Table 3.4.

Finally, deposition on vegetation surfaces is achieved by adding a sink term S (mg.m^{-3}.s^{-1}) in the transport equation:

$$S = \rho * C_{pollutant} * v_d * LAD \tag{3.19}$$

where C$_{pollutant}$ (ppm) is the pollutant mass fraction, LAD is the leaf area density (m^2/m^3).

3.3.1.3 Emissions of VOCs by trees

Following Guenther et al. (1995, 2000), Owen et al. (2001), Wang et al. (2003), emissions of volatile organic compounds (VOC) by trees are computed as follows:

$$E = \epsilon D_{biomass}\ \gamma_P\ \gamma_T\ \gamma_A\ \xi \tag{3.20}$$

where ϵ is the tree emission factor (μg C g^{-1} h^{-1}), $D_{biomass}$ is the dry foliar mass (g), γ_P, γ_T, γ_A are emission activity factors representing the influence of PAR (Photosynthetic Active Radiation), temperature and leaf age respectively, ξ is an escape efficiency factor that represents the fraction of the VOCs emitted by the canopy that is released into the nearby atmosphere. Following Wang et al. (2003), Kalogridis (2014), ξ is assumed constant and equal to 0.95. The influence of leaf age is neglected here (γ_A=1). The trees used in this study are assumed to be "Sophora Japonica", as this species is common in the streets of Paris (Ville de Paris 2020) and its emission factors are high, especially for monoterpenes (Ren et al. 2017): $\epsilon = 69.2$ μg C.g^{-1}.h^{-1} for isoprene and $\epsilon = 1.9$ μg C.g^{-1}.h^{-1} for monoterpenes. The foliar density is computed following Nowak (1996):

$$D_{biomass} = exp\left(7.6109 + 0.0643\ DBH\right) \tag{3.21}$$

with DBH the Diameter at Breast Height (cm), which is computed from the tree circumference, assumed to be 100 cm here (which seems to be a realistic value for "Sophora Japonica" in Paris according to Ville de Paris (2020)). Concerning the temperature dependency, γ_T is estimated following Guenther et al. (2000), Wang et al. (2003):

$$\gamma_T = E_{opt} C_{T_2} \frac{exp\left(\frac{C_{T_2}}{R}\left(\frac{1}{T_{opt}} - \frac{1}{T}\right)\right)}{C_{T_2} - C_{T_1}\left(1 - exp\left(\frac{C_{T_2}}{R}\left(\frac{1}{T_{opt}} - \frac{1}{T}\right)\right)\right)} \tag{3.22}$$

where T is the leaf temperature assumed here to be equal to the air temperature (K), R = 0.00831, $C_{T_1} = 80$ and $C_{T_2} = 200$, E_{opt} is the maximum normalised emission capacity, T_{opt} is the temperature at which E_{opt} occurs (Guenther et al. 2006):

$$E_{opt} = 1.75 exp\left(0.08(T_D - 297)\right) \tag{3.23}$$

$$T_{opt} = 313 + 0.6(T_D - 297) \tag{3.24}$$

with T_D the daily temperature (K). The PAR dependence is only considered for isoprene emissions (Guenther et al. 1993):

$$\gamma_P = \frac{\alpha \, C_L \, PAR}{\sqrt{1 + \alpha^2 . PAR^2}} \tag{3.25}$$

with $\alpha = 0.0027$ and $C_L = 1.066$.

3.3.2 Supplementary figures

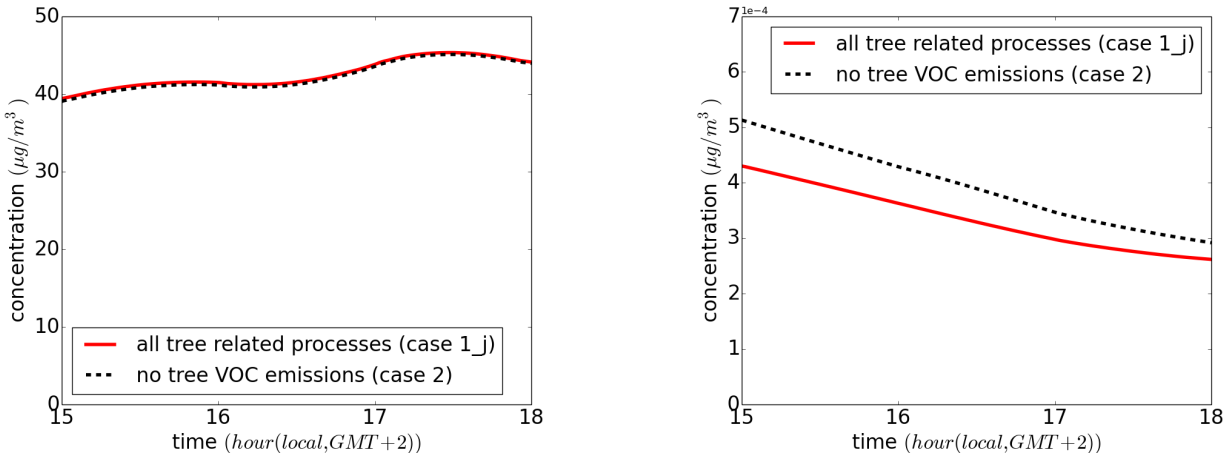

(a) NO_2 (b) OH

Fig. 3.4 Impact of tree VOC emissions on street-average concentrations. The impact of tree VOC emissions on NO_2 concentrations is very low, but it leads to a non-negligible decrease of OH concentrations.

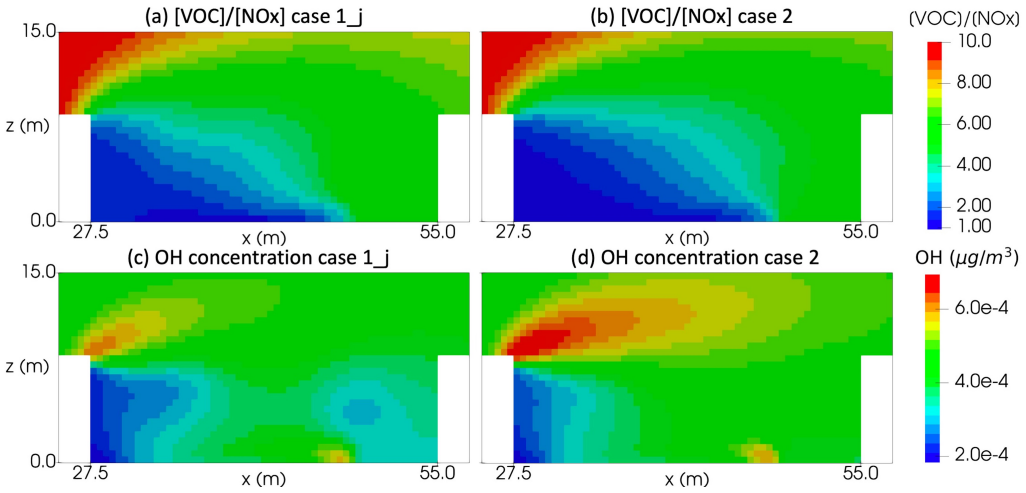

Fig. 3.5 Average chemical regime and OH concentration in the street. (a) chemical regime in the street with all tree-related processes (case 1), (b) chemical regime in the street with no tree VOC emissions (case 2), (c) average OH concentration in the street with all tree-related processes (case 1), (d) average OH concentration in the street with no tree VOC emissions (case 2). As the simulation is typical of summer time with relatively low background concentrations of NO and NO_2 but high biogenic VOC concentrations, the boundary condition is in a NOx-limited regime (Kinosian 1982)(the concentration ratio [VOC]/[NOx] is 10). However, because of the traffic emissions, the regime is rather VOC-limited, with low [VOC]/[NOx] in the street and just above the street. Tree VOC emissions do not drastically change the chemical regime, although the [VOC]/[NOx] are slightly higher with trees. In the street (VOC-limited), O_3 concentration is low because it is titrated by NO. The averaged increase of O_3 concentration is therefore low, by only about 0.2%. This may not lead to an increase of OH concentration. Meanwhile, as the main reactive oxidant in the daytime, OH is consumed by the VOCs emitted by trees. When tree VOC emissions are taken into account, the lowest OH concentration is observed around the tree crown, which indicates that the formation of OH by O_3 photolysis is lower than its consumption by VOCs.

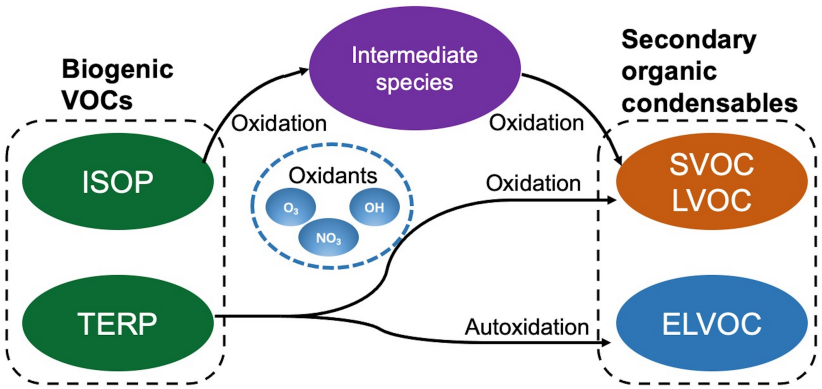

Fig. 3.6 Reaction scheme of biogenic VOCs to form secondary organic condensables in the chemical scheme used in the paper. Isoprene (ISOP) is oxidized into intermediate species, which are then oxidized to form SVOC (Semi Volatile Organic Compounds) and LVOC (Low Volatile Organic Compounds). SVOC and LVOC are also formed from terpene (TERP) oxidation, and ELVOC (Extremely-Low Volatile Organic Compounds) are formed from terpene autoxidation.

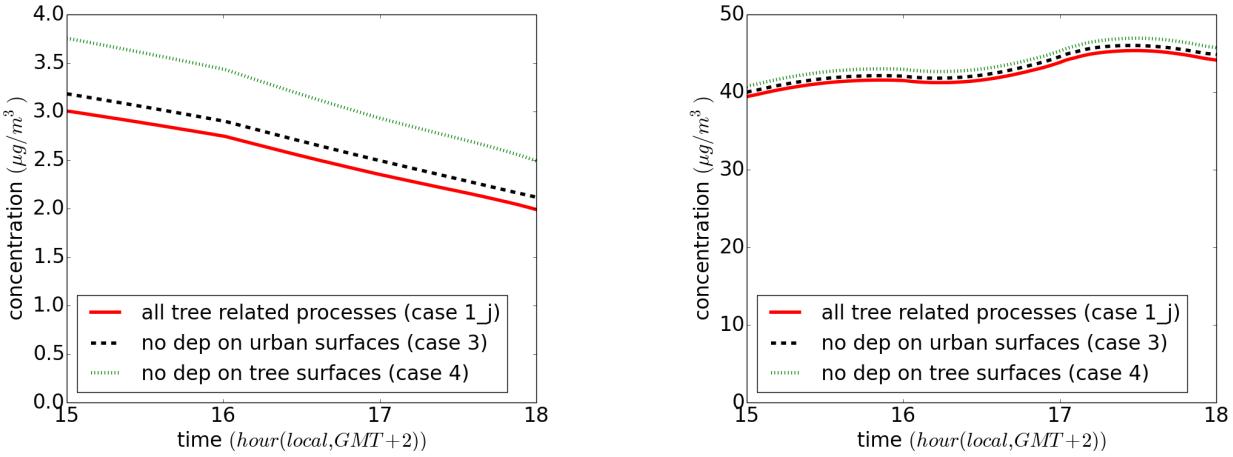

(a) HNO_3 (b) NO_2

Fig. 3.7 Impact of dry deposition on street-average concentrations. The impact of dry deposition is large for highly soluble compounds such as HNO_3 but is limited for other species such as NO_2.

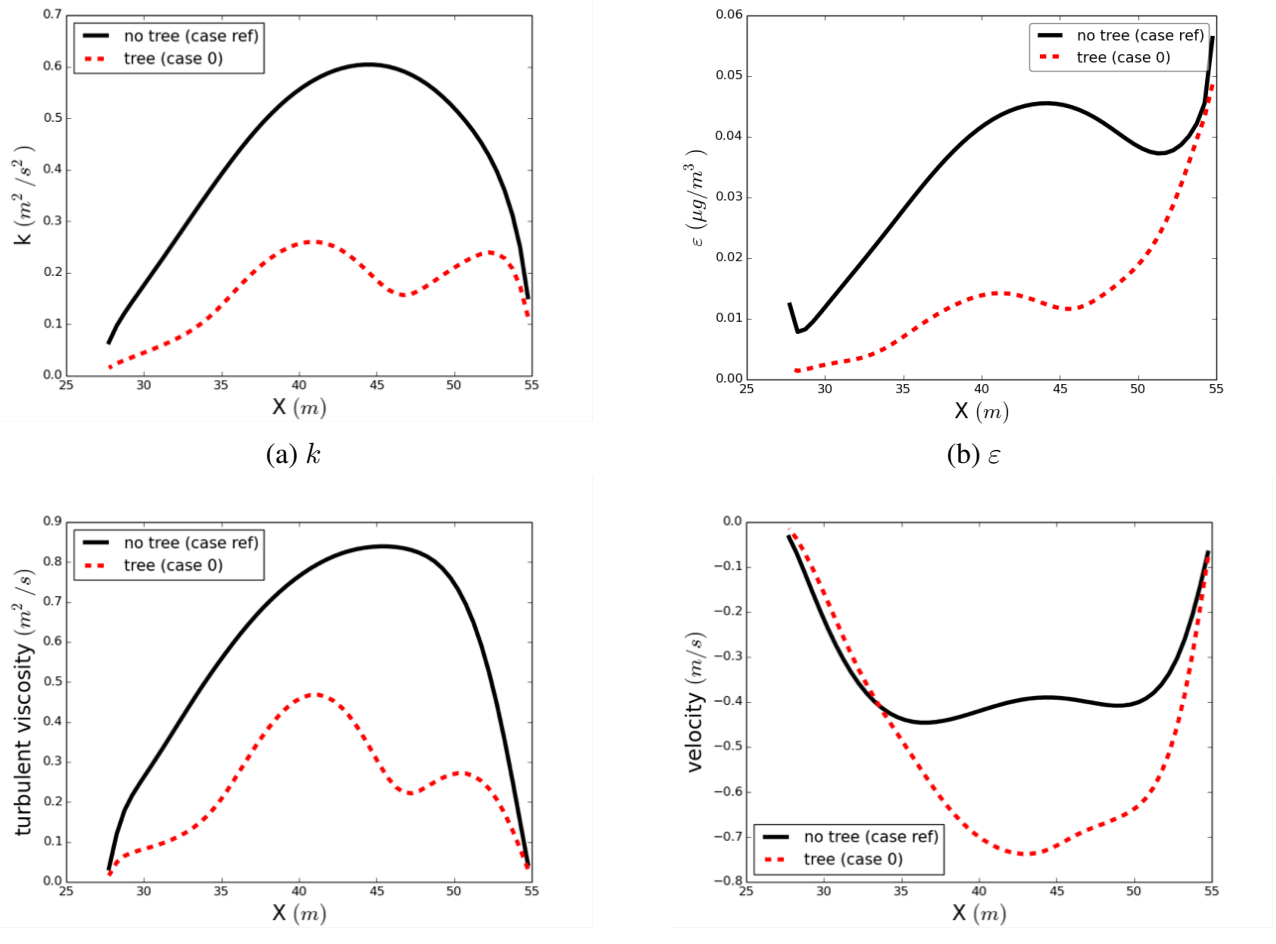

(a) k (b) ε

(c) ν_t (d) U

Fig. 3.8 Horizontal turbulence and horizontal velocity profile in the street. These profiles correspond to a height of 1.5 m in the street at 4 p.m.

CHAPTER 4

Modeling of air quality in the Pierre de Coubertin Stadium

Abstract

Indoor air quality is important for the health of human beings. In this chapiter, the indoor air quality in an enclosed stadium is modeled using a 0D model (H^2I). The model is setup using measurements of aeraulic parameters and concentrations. In order to determine a representative outdoor-to-indoor exchange rate and the filtration rate of the model, a Fourier transformation is performed on the indoor and outdoor measurements of black carbon, which is chosen because of its chemical stability. The model is then applied to estimate indoor concentrations of NO, NO_2 and O_3 using outdoor measurements of O_3 and outdoor estimation of NO and NO_2 concentrations. The temporal variations of the indoor concentrations of O_3 and NOx are well representedcompared to measurements. However, NO concentrations are overestimated and NO_2 and O_3 concentrations are underestimated. Sensitivity tests are conducted to determine the relevant physical parameters of the model that may control the variation of these concentrations. Because of the large volume and small surface/volume fraction in the stadium, the impact of heterogenerous reactions on surfaces is less important in the stadium than in other smaller indoor environments, such as building rooms. VOC concentrations have significant impacts on the concentrations of O_3 and NOx. Their presence favors the conversion from NO to NO_2, thus improving the simulated NO and NO_2 concentrations. Photolysis is another process strongly impacting the pollutant concentrations. This chapter illustrates a methodology to simply model indoor concentrations, and it underlines the importance of characterising VOC concentrations and radiation for an accurate modelling of indoor NO, NO_2 and O_3 concentrations.

4.1 Introduction

Indoor air quality (IAQ) is an important environmental issue. According to Klepeis et al. (2001), people spend an average of about 90% of their time indoors, which makes indoor air quality essential for human health and social productivity. In recent years, with the development of social economy, people's pursuit of sports activities has significantly increased. The IAQ in sports stadiums is thus attracting increasing attention, as poor air quality may also affect the performance of athletes. For example, high levels of air pollution may impair lung function (Zhou et al. 2016) and thus decrease

athletic performance. Amongst the indoor pollutants, there are nitrogen oxides (NOx), ozone (O_3), volatile organic compounds (VOC) and particles of which black carbon (BC) is a compound emitted by combustion processes. The pollutants may originate from outdoor, e.g. if the stadium is located near a busy road or highway, emissions from vehicles can contribute to BC and NOx levels in the air (Bennett et al. 2019). This filtration can occur through cracks and gaps in building envelopes, as well as through ventilation systems that bring in outdoor air. Some pollutants such as VOCs may also originate from indoor. Many cleaning agents contain chemicals that can release VOCs when they evaporate; many building materials, such as carpets, flooring, and insulation, can release VOCs over time, particularly when they are new (Shin and Jo 2013); and people in a stadium can also release VOCs, when they exhale and emit sweat (Liu et al. 2016).

Recently, IAQ models of various complexities have been developed to represent indoor air concentrations. In the simplest approach, the indoor compartment is represented with a box model, taking into account indoor and outdoor exchanges using a filtration factor. For example, Chaloulakou and Mavroidis (2002) evaluated the indoor and outdoor carbon monoxide (CO) concentrations of a building in Athens using a one-compartment IAQ model including interior sources. The model solved the mass-balance equations for pollutant flows without considering chemical reactions. To evaluate the model, hourly-averaged measurements were conducted for two consecutive periods. Although some sharp outdoor changes could not be reproduced, the comparison showed a general good agreement between the simulations and the measurements. In more complex approaches, computational fluid dynamic (CFD) models are used to estimate the indoor-outdoor exchanges and the flow inside the building. Tong et al. (2016) evaluated the impact of traffic-related pollutants on the IAQ in a building with natural ventilation based on a CFD model. The impacts on IAQ of different parameters such as the distance between the roadway and building, the window size and its opening location,were quantified.Similarly, Van Hooff and Blocken (2010) developed a specific coupled approach to represent the urban wind flow and indoor natural ventilation by simultaneously generating the complex geometry of indoor and outdoor environment using a CFD tool with a high-resolution grid. This model was applied to an semi-enclosed stadium to evaluate the role of natural ventilation.

Indoor chemistry has been considered in various IAQ models for a long time (Weschler and Carslaw (2018)). As early as in 1986, Nazaroff and Cass (1986) used a chemically reactive homogeneous system to reproduce the indoor concentrations of NOx and O_3. Heterogeneous reactions on indoor surfaces may also impact the IAQ, as the ratio between the surface and the volume for a indoor space is relatively larger than outdoors.

Stadium air quality has not received yet much attention in the literature, and this study aims at determining the main processes influencing a stadium indoor concentrations. Concentrations of NO_2, O_3 and BC have been measured in a stadium in Paris, and the IAQ box model H^2I (Fiorentino et al. (2020)), which takes into account indoor/outdoor exchanges, deposition, emissions and chemistry, is used for modelling the concentrations. A methodology is defined to determine the outdoor-to-indoor filtration rate from the measurements of BC concentrations, which were conducted in the indoor and outdoor environments of the stadium. BC was chosen to determine the filtration rate because it is inert

and not affected by chemical reactions. The influence of homogeneous chemistry, surface reactions and photolysis on NO_2 and O_3 concentrations is assessed.

4.2 Description of the stadium

In this study, the Pierre de Coubertin stadium (Coubertin) in Paris, France is studied and modeled, as it is one of the stadiums where the Paris Olympics will be held. It is an enclosed stadium, located at the southwest of Paris. As shown in Fig 4.1, it is surrounded by large avenues, suggesting that traffic emissions may largely impact outdoor and hence indoor air quality.

Fig 4.2 shows the top view of the stadium. It contains three halls, several sports rooms, media and office rooms. In this chapter, only the air quality in the grand hall is studied. Fig 4.3 shows the inside view of the grand hall. On both sides of the hall, the bleachers are composed of three tiers. On the front and on the back of the stadium, the bleachers are composed of two tiers.

The hall can hold more than 4000 people for basketball, handball or other sports matches. In order to acquire the geometry data of the grand hall, a 3-D scanner was used (Focus M70 model). The measurements were conducted by collegues in the laboratory CEREA. A cloud of points representing the stadium was obtained from the scans, as shown in Fig 4.4. According to the scan data, the volume and the surface of the grand hall are 23303 m^3 and 13986 m^2.

The supply airflow in the stadium is realized by a group of 4 rooftop air handler systems. The rated airflow of each handler is 25000 $m^3.h^{-1}$. Generally, each air handlers operates at 60% of the rated power, forming an amount of airflow of 60000 $m^3.h^{-1}$.

4.2.1 Measurements of indoor and outdoor air quality in the stadium

Measurement campaigns for indoor and outdoor pollutant concentrations of the Pierre de Coubertin Stadium were carried out between the 25^{th} May and the 20^{th} June 2021 by collegues in the laboratories LISA and CSTB.

Indoor and outdoor concentrations of PM_{10}, $PM_{2.5}$, black carbon (BC), O_3, NOx (nitrogen monoxide NO and nitrogen dioxide NO_2), and VOCs were investigated with different instruments:

- A FIDAS 200 particle size analyzer for PM_{10} and $PM_{2.5}$ concentrations;
- A Magee Scientific Aethalometer AE33 for BC concentrations;
- A AC32e from ENVEA for NOx concentrations;
- A O342e from ENVEA for O_3 concentrations;
- Passive and active samplers for VOC concentrations.

These instruments were installed on a platform in the grand hall for the indoor measurements and on a balcony for the outdoor measurements.

Fig. 4.1 Map of the Pierre de Coubertin Stadium (screenshot from Google map).

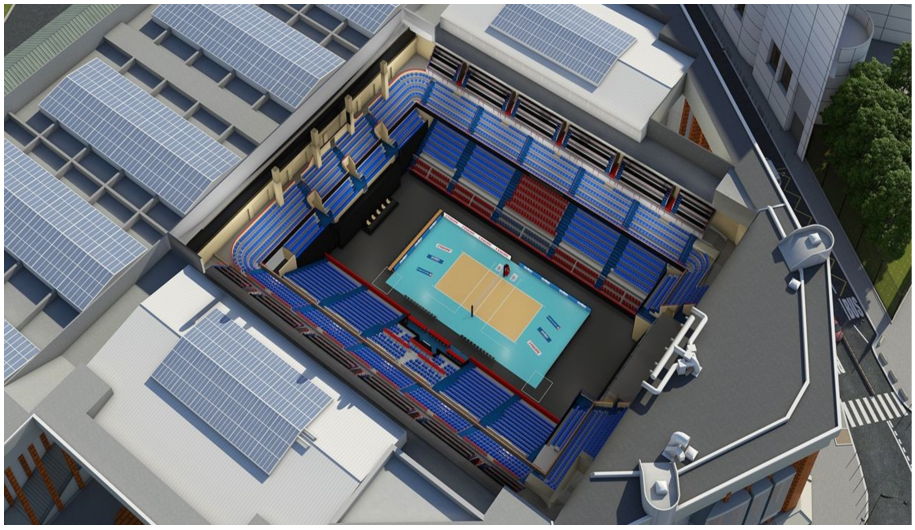

Fig. 4.2 Top view of the Pierre de Coubertin Stadium. Source: Artstation.

(a) Front and side view of the grand hall

(b) Back and side view of the grand hall

Fig. 4.3 The grand hall of Pierre de Coubertin Stadium.

Fig. 4.4 Cloud points of 3-D scan in the grand hall.

Fig 4.5 shows the indoor and outdoor diurnal measurements of O_3, NO_2 and BC concentrations between the 28^{th} May and the 20^{th} June 2021. Measurements of outdoor NO_2 concentrations are not available. Therefore, they are estimated from multi-scale forecast performed by the air-quality agency Airparif using the model CHIMERE (Menut et al. 2013, Mailler et al. 2017) for the regional scale coupled to the ADMS local-scale model (Carruthers et al. 1994, Stocker et al. 2012). The lack of measured outdoor NO_2 concentrations and uncertainties in the modelling of NO_2 concentrations may lead to some errors in the subsequent simulations for related indoor pollutant concentrations.

The measuring instruments have different sampling frequency, from 1 min to 15 min. The time series of measurements in Fig 4.5 are averaged every 30 min. For O_3, generally, the diurnal variation trend of indoor and outdoor concentrations are consistent, with peak concentrations around 4 p.m. and valley concentrations around 8 a.m. The outdoor concentration is higher than the indoor one, by a factor around 2. For BC, the time variation of indoor and outdoor concentrations are also similar, with peak concentrations around 8 a.m. Although there are no significant valley values, the nighttime concentrations are generally lower than daytime concentrations. However, on the 4^{th} June, the BC concentrations are very high appear between 8 p.m. and 9 p.m., which may be explained by the use of fumigants after a handball match in the stadium. For NO_2, according to the outdoor simulations, the peak outdoor concentrations are around 8 a.m., and in the nighttime, the outdoor concentrations are generally lower than in the daytime. While for NO_2 indoor concentrations, the peak starts in the morning around the same time as outdoor concentrations, it lasts 1 to 2 hours longer than for outdoor concentrations. These higher concentrations over a longer period of time may be explained by the lower ventilation of the NOx that penetrate indoor during the traffic peak and bythe formation of NO_2 from chemical reactions inside the stadium.

For VOC concentrations, 6 passive samplers (Radiello® code 145) were installed and exposed for 7 consecutive days over a total period of three weeks between May 27 and June 17 at two sampling points (inside at grand stand P and outside). Besides, active samplers (Tube Tenax TA type Perkin Elmer) were also installed for specific days according to the schedule of matches held in Coubertin: on the 30^{th} May and the 4^{th} June, when two handball matches were held in Coubertin; on the 12^{th} June, the day of the olympic karate qualifying tournament; and also on the 15^{th} June, the day outside the sports tournament as a reference. The Radiello® code 145 cartridges were used to monitor the weekly variation of VOCs over the entire on-site intervention campaign; while Tube Tenax TA was used to monitor the hourly variation of VOCs during specific events or dedicated days, Each sample was updated every 2 hours and was collected at one sampling point. Measurement data of VOCs are presented in Table 4.5 of Appendix 4.7.1.

4.2.2 Other input data necessary for the simulation

4.2.2.1 Outdoor NO concentrations

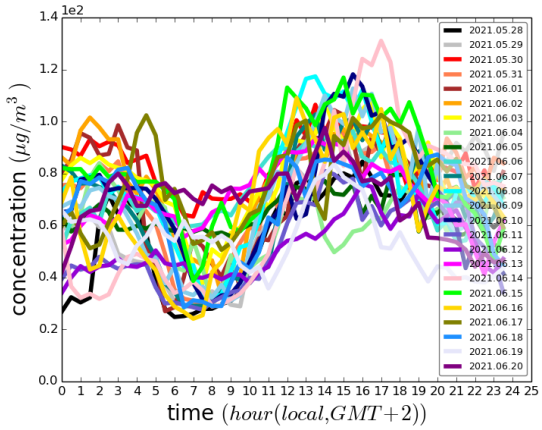

(a) Outdoor O_3

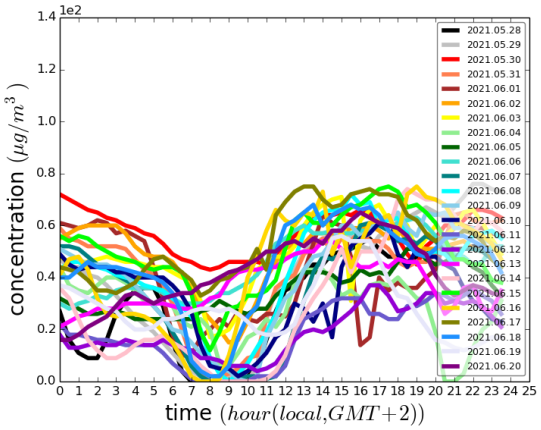

(b) Indoor O_3

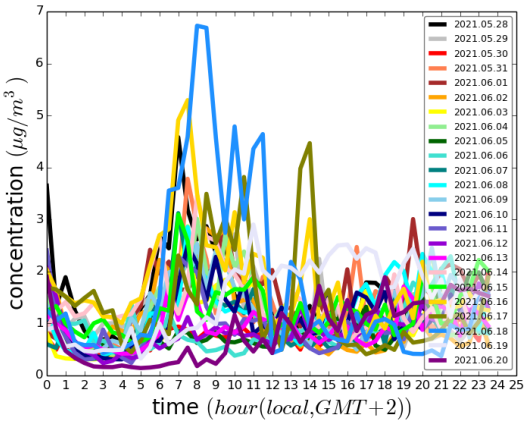

(c) Outdoor BC

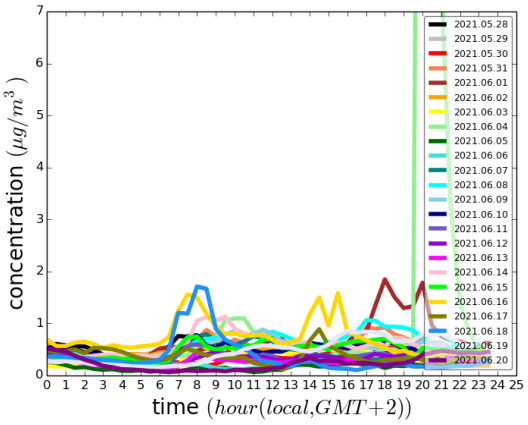

(d) Indoor BC

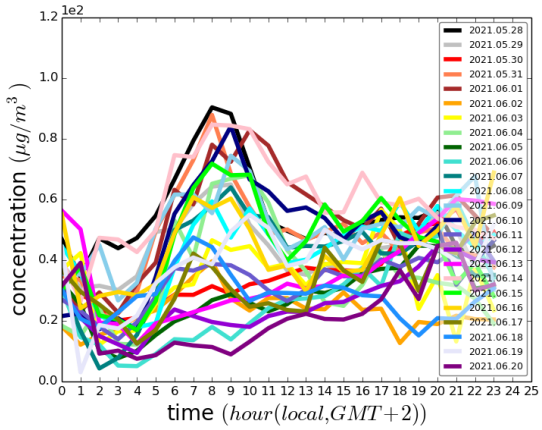

(e) Outdoor NO_2

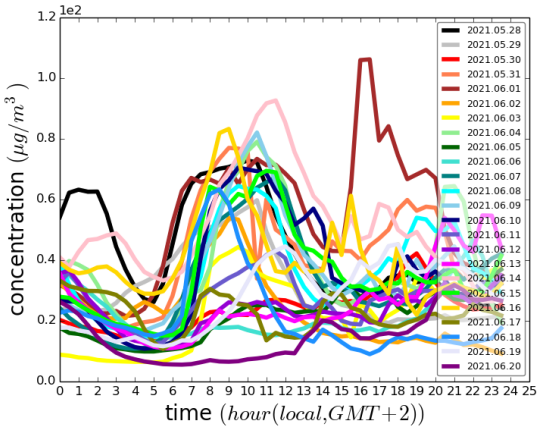

(f) Indoor NO_2

Fig. 4.5 Outdoor and indoor measurements of O_3, BC and NO_2 concentrations. Note that outdoor NO_2 concentrations were not measured, but are estimated from multi-scale air-quality modelling.

Outdoor NO concentrations are not available from measurements, nor from modelling. Therefore, they are estimated from the simulated NO_2 concentrations and a typical NO/NO_2 ratio typically observed in the streets of Paris. To determine this ratio, a station in Paris where NO and NO_2 concentrations are measured is identified. To do so, several measurements of outdoor NO_2 concentrations at different measurement stations operated by Airparif are compared with the simulated NO_2 concentrations outside of Coubertin.

Table 4.6 in the Appendix lists the measurement stations which are less than 10 km away from Coubertin, alongside with their distances to Coubertin. Hourly-averaged NO_2 concentrations measured during the same period in 2020 (28 May to 20 June) are shown in Fig 4.6 and are compared to the average NO_2 concentrations simulated at Coubertin. It can be seen that the measured concentrations at the OPERA stationare of the same order of magnitude as those simulated at Coubertin, and according to table 4.6, the OPERA station is relatively close to Coubertin (about 7 km).

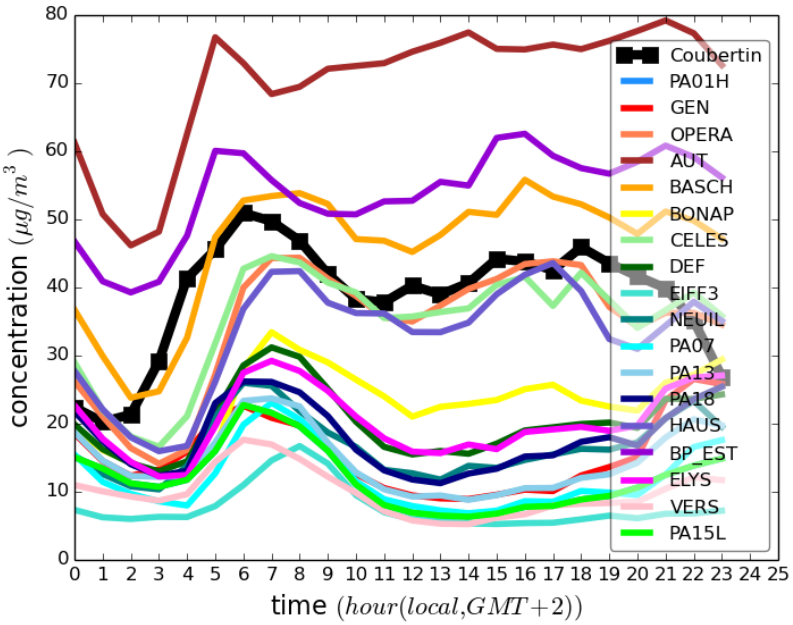

Fig. 4.6 Comparison of the outdoor NO_2 concentrations of Coubertin with measured concentrations in 2020. Coubertin represents the outdoor concentrations simulated at Coubertin, the other legends correspond to the names of the stations listed in Table 4.6.

The NO and NO_2 concentrations measured at the station OPERA are thereafter used to estimate the outdoor NO concentration at Coubertin $C^{out}_{NO,Coubertin}$ through a rule of three:

$$C^{out}_{NO,Coubertin} = \frac{C^{out}_{NO_2,Coubertin}}{C^{out}_{NO_2,OPERA}} \times C^{out}_{NO,OPERA} \tag{4.1}$$

Fig 4.7 shows the hourly variations of the outdoor ratio of NO and NO_2 concentrations (compared in ppb). For NO_2, the ratio varies from 0.4 to 0.75, with an average value of 0.52. For NO, the ratio varies from 0.25 to 0.60, with an average value of 0.48. These ratios correspond well to the

measurements of Rao and George (2014), who measured, in summer in urban areas, NO_2/NOx ratios between 0.20 and 0.76, with an average ratio of 0.54.

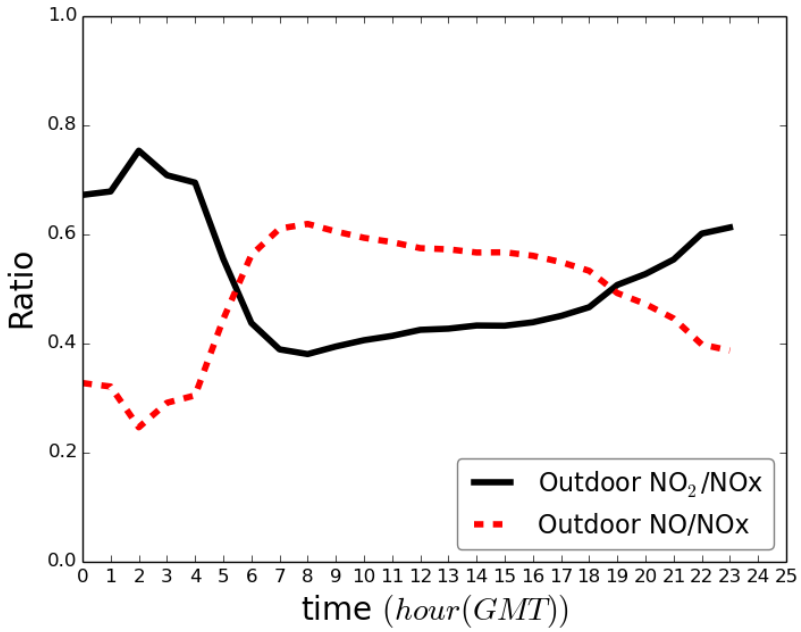

Fig. 4.7 Hourly-variations of outdoor NO_2/NOx and NO/NOx ratios.

4.2.2.2 VOC concentrations

The number of VOC species measured in Coubertin are too limited to study their impact of Coubertin VOCs on indoor air quality.

Comprehensive measurements of indoor VOC concentrations were conducted using a PTR-ToF-MS in an office in Marseille (Fiorentino et al. 2020). The measurement data inside Coubertin is compared to the indoor VOC measurement of Marseille in terms of time variation and order of magnitudes in Fig 4.8, which presents the comparison of 8 VOC species measurements, including acetic acid ($C_2H_4O_2$), 2-butanone (C_4H_8O), benzene (C_6H_6), toluene (C_7H_8), styrene (C_8H_8), benzaldehyde (C_7H_6O), ethyl acetate ($C_4H_8O_2$) and hexanal ($C_6H_{12}O$) in Marseille and in Coubertin. The measurement data of Marseille is hourly-averaged, while the concentrations in Coubertin are averaged over 2 hours. The concentrations of VOCs largely emitted by traffic, such as toluene and benzene are much higher in Coubertin than in Marseille, especially in the morning during the traffic peak. On the opposite, the concentrations of other compounds such as 2-butanone and acetic acid are much higher in Marseille than in Coubertin. Despite the large differences of VOC concentrations in Marseille and Coubertin, the VOC concentrations measured in Marseille are used to estimate the potential role of VOCs on NO_2 and O_3 formation (see section 4.5.4.1), using different rescaling factors.

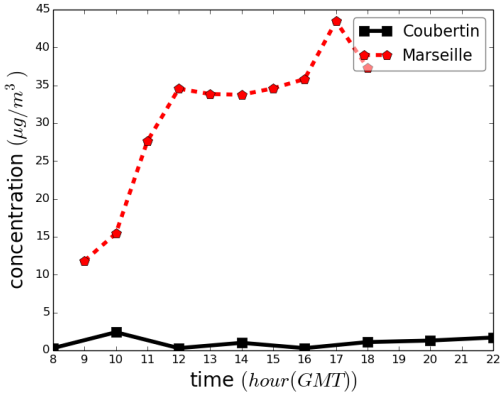

(a) $C_2H_4O_2$

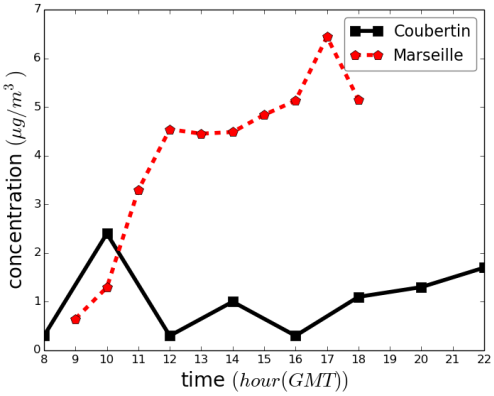

(b) C_4H_8O

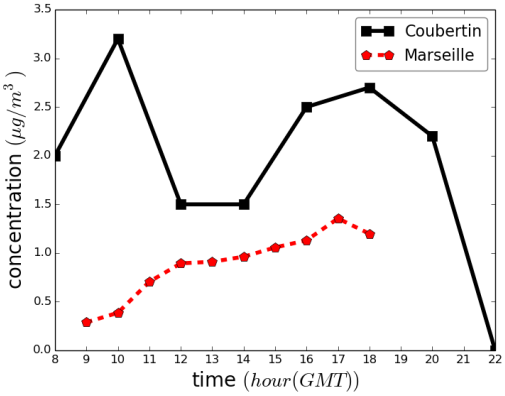

(c) C_6H_6

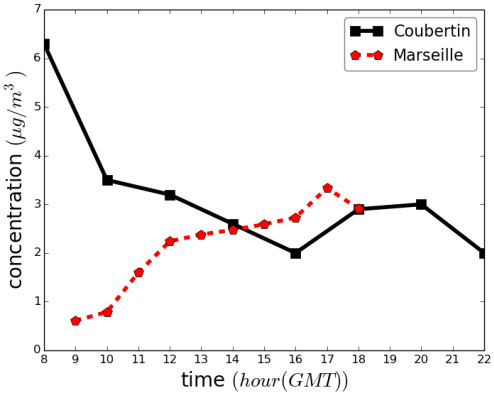

(d) C_7H_8

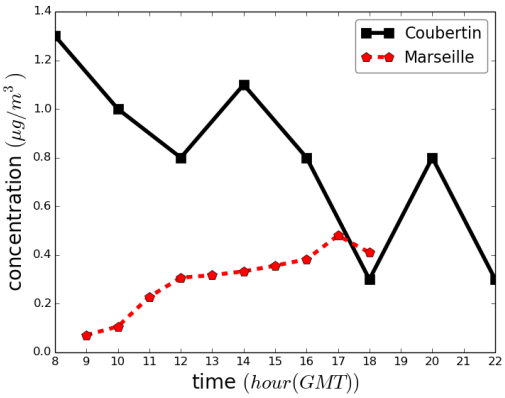

(e) C_8H_8

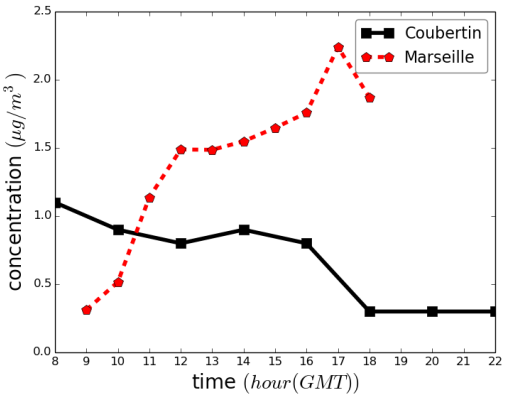

(f) C_7H_6O

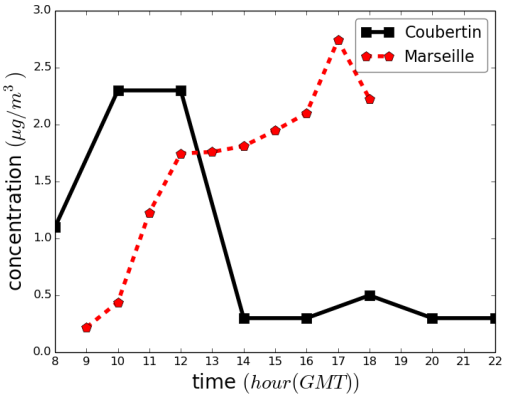

(g) $C_4H_8O_2$

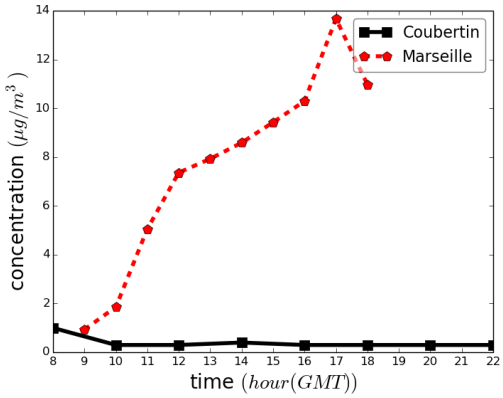

(h) $C_6H_{12}O$

Fig. 4.8 Comparison of indoor VOC measurements in Marseille and in Coubertin.

4.2.2.3 Meteorological conditions

Meteorological conditions including the time series of temperature (K) and relative humidity (%) are observation data coming from international surface observation reports (SYNOP) circulating on the Global Telecommunication System (GTS) of the World Meteorological Organization (WMO). The time series of temperature and humidity varying every three hours from the station Orly were used in the simulation.

4.3 Presentation of the model

4.3.1 H^2I model

In the present study, the 0-D box model homogeneous heterogeneous indoor (H^2I) developped by Fiorentino et al. (2020) is used for simulating the diurnal air quality in Coubertin.

H^2I is a two-box model, which divides a room into two boxes: the lighted part and the shaded part. The lighted part is illuminated by the direct light, such as the solar light, and the shaded part is subject to indirect light. The different intensity of lights leads to the different photolysis reaction rates. Here, only one box is used, as the volumes of the light and the shaded parts are not known.

4.3.1.1 Governing equation

In the model, the indoor concentration is controlled by several processes: the outdoor-to-indoor exchange, the indoor-outdoor leakage, the deposition, the indoor emission and chemical reactions (including photolysis reactions). The governing equation of the concentration C_i^j evolution with time of species i in the box j is shown as follows:

$$\frac{\mathrm{d}C_i^j}{\mathrm{d}t} = k_{AER} f C_i^{out} - k_{AER} C_i^j - k_{DEP,i}^j C_i^j + \sum_p \frac{Q_{pi}^j}{V_{box}^j} + \sum_q \frac{R_{iq}^j}{V_{box}^j} \tag{4.2}$$

where k_{AER} is the outdoor-indoor air exchange rate [s^{-1}]; f is the outdoor-indoor filtration factor, which represents the fraction of air exchange with outdoor; $k_{DEP,i}^j$ is the deposition rate [s^{-1}]; Q_{pi}^j is the emission rate of source p for species i [$\mu g.s^{-1}$]; V_{box}^j is the volume of box j and R_{iq} is the reaction rate between species i and species q [$\mu g.s^{-1}$].

4.3.1.2 Interactions with surfaces

For indoor air quality, surface reactions of compounds that are adsorbed at the surface are important for the formation of secondary pollutants (Weschler 2011), such as HONO. With a faster reaction rate than the equivalent gas-phase reactions, HONO is mainly produced by the hydrolysis of NO_2 on surfaces. The formation of HONO can be presented following Febo and Perrino (1991):
$2\,NO_2 + H_2O \longrightarrow HONO + HNO_3$

In this reaction, although HNO_3 is also produced, it remains at the surface because of the high adsorption ability.

The adsorption/deposition rate of pollutants is modeled by a term involving a transport-limited rate and surface reaction rate as follows:

$$\frac{1}{k^j_{DEP,i}} = \frac{1}{k^j_{tran,i}} + \frac{1}{k^j_{react,i}} \tag{4.3}$$

Where the $k^j_{tran,i}$ is the deposition rate of species i by transport in the room j [s^{-1}] and $k^j_{react,i}$ is the surface reaction rate of species i in the room j [s^{-1}] (Grøntoft and Raychaudhuri 2004).

The $k^j_{tran,i}$ is controlled by the diffusivity D_i of species i [$m.s^{-1}$] and the friction velocity u^* [$m.s^{-1}$] following Lai and Nazaroff (2000):

$$k^j_{tran,i} = v_{trd,i}\frac{S^j_{box}}{V^j_{box}} \tag{4.4}$$

$$v_{trd,i} = v^{ad}_{trd,i}u^* \tag{4.5}$$

$$\frac{1}{v^{ad}_{trd,i}} = \int_{r_0}^{30}(\frac{1}{\frac{\nu_t}{\nu} + \frac{D_i}{\nu}})dy^{ad} \tag{4.6}$$

Where $v_{trd,i}$ is the deposition velocity by transport [$m.s^{-1}$], S^j_{box} is the surface of the room j, $v^{ad}_{trd,i}$ is the dimensionless deposition velocity, y^{ad} is the dimensionless distance from the surface, ν is the kinematic viscosity of air, ν_t is the turbulent viscosity of air, r_0 is the adimensional minimum distance from the surface, in another word, the position where species touch the surface. For gaseous species, the r_0 is taken as 0; for particles, $r_0 = (d_p/2)(u^*/\nu)$, where d_p is the particle diameter.

The $k^j_{react,i}$ is controlled by the uptake coefficient γ_i [-] and the thermal velocity ω_i [$m.s^{-1}$] of species i (Fiorentino et al. 2020). It can be expressed as:

$$k^j_{react,i} = \frac{\gamma_i\omega_i}{4}\frac{S^j_{box}}{V^j_{box}} \tag{4.7}$$

Where ω_i is dependent on the temperature in the room and the molecular weight of species i:

$$\omega_i = \sqrt{2.1171 \times 10^4 \frac{T}{M_i}} \tag{4.8}$$

4.3.1.3 Gas-phase reactions

To solve the gas-phase chemistry, the lumped-species based mechanism RACM2 is used (Goliff et al. 2013). This mechanism is modified by also taking into account surface reactions to adapt for the indoor environment. It contains 117 species and 362 reactions in total. Among this mechanism, 11 heterogeneous reactions are included to solve the surface reactions.

4.3.2 Simplification and modification in Coubertin

In the present study, different parameters of the model are characterized or simplified to adapt to the known characteristics of Coubertin.

Considering the light, the grand hall is well lit by the light of sun through the transparent windows on four walls, as well as the artificial lights inside the hall, to maintain the stability of the light intensity. Therefore, the grand hall is assumed all illuminated by direct lights with homogeneous intensities. However, the characteristics of the light and its intensity are not known. Therefore, sensitivity tests assuming different glazing and light characteristics are conducted in section 4.5.4.2.

Indoor emissions are also neglected, because of lack of information about potential sources, such as building materials, cleaning agents, and emissions from special sport events.

In the current version of the model, the deposition rate is only determined for gaseous species. To model the deposition of BC, the transport-limited rate is modified to take into account the diameter of particles, as detailed in the equation 4.6. For BC, a typical diameter of 100 nm is assumed ((Ning et al. 2013, Reddington et al. 2013)).

4.3.3 Model parameter from CFD modeling

In order to evaluate the deposition velocity for different species, a set of boundary conditions are needed for solving the equation. In the study of Hector AMINO (Galante Amino 2022), the CFD model of the grand hall which is based on the 3D scan is built using the CFD tool Code_Saturne. The ventilation in the stadium is simulated without considering other physical and chemical processes. For acquiring correct boundaries, the simulation using the information provided by the stadium management team about the air handling unit (AHU) is conducted. In this simulation, the blowing and return winds are defined, with the blowing zone set as the inlet boundary condition and the extraction one as an outlet. The friction velocity u^* in Coubertin, which is used used to represent the shear stress in the form of velocity, is defined in the wall function, which is detailed in Appendix 4.7.3. The mean value of u^* acquired from the aeraulic study in Coubertin with CFD modeling is $8.02 \times 10^{-4} m/s$.

4.4 Outdoor to indoor air exchange

In H^2I model, the outdoor-to-indoor exchange rate k_{AER} represents the air renewal rate, which is dependent on the air handler in the hall. The value of the window filtration factor f ranges between 0.1 to 0.9 (Sarwar et al. 2002) and it needs to be determined for the modelling.

As defined in section 4.3.1.1, the filtration factor f represents the fraction of air exchange with outdoor air. Although some outdoor and indoor measurements are accessible, it is hard to determine the window filtration factor as the ratio between indoor and outdoor concentrations vary along the time. Therefore, in order to solve the exchange rate k_{AER} and the filtration coefficient f, the measured outdoor and indoor concentrations are decomposed into a sum of signals using Fourier transform. Each

term in the series has different amplitudes, which represent the "weight" of each signal in forming the total concentration. The objective of this transform is to find the appropriate fraction between indoor and outdoor concentrations and also acquire the exchange rate with these concentrations. The concentration of BC is used for finding the k_{AER} and f because BC is considered as an inert particle and do not participate in the gas-phase reactions nor in the surface reactions.

4.4.1 Discrete Fourier transform

As the time series of concentrations are finite sequences, the discrete Fourier transform (DFT) is used in the study to represent the concentrations. Since there are only a finite number (N) of input signals and a separation T between samples, the DFT considers the input data is periodic, with the period of NT. Therefore, the fundamental frequency of this signal is $\frac{1}{NT}$ Hz. This leads to:

$$F[n] = \sum_{p=0}^{N-1} f[p] e^{j\frac{2\pi n}{NT}pT} \tag{4.9}$$

where F is the Discrete Fourier Transformation of f. Hereafter, ω is represented as $\omega = 0, \frac{2\pi}{NT}, \frac{2\pi}{NT} \times 2, ..., \frac{2\pi}{NT} \times (N-1)$.

In order to acquire a representative air exchange and filtration rate over the period of measurements, the measurements are smoothed by averaging the BC concentrations on an hourly basis.

4.4.2 Analysis of amplitude for each mode

Indoor and outdoor BC concentrations were transferred into the form of a discrete Fourier transform. The amplitude of each mode p (Amp_p) is the square root of the sum of the squares of the real and imaginary parts of the DFT (Naeim 2001). Table 4.1 and table 4.2 present the amplitudes and the fraction of each mode p (Fra_p) for the outdoor and indoor signals respectively. The fraction Fra_p of each mode is obtained from

$$Fra_p = \frac{Amp_p}{\sum_{p=0}^{N-1} Amp_p} \tag{4.10}$$

It can be seen that both for indoor and outdoor concentrations, half of the concentrations are represented by the first mode (mode 0) of the Fourier transform, and about 90% of the concentrations by the first 4 modes (mode 0 - mode 4).

Table 4.1 Outdoor amplitude for each mode.

mode	0	1	2	3	4	5	6	7	8	9	10	11	12
Amp_p	4.60	0.33	0.78	0.40	0.12	0.03	0.12	0.15	0.05	0.06	0.02	0.05	0.08
Fra_p	67.8%	4.8%	11.5%	5.9%	1.8%	0.5%	1.8%	2.2%	0.7%	0.9%	0.2%	0.8%	1.1%

Table 4.2 Indoor amplitude for each mode.

mode	0	1	2	3	4	5	6	7	8	9	10	11	12
Amp_p	1.62	0.15	0.13	0.11	0.06	0.4	0.03	0.04	0.02	0.01	0.01	0.01	0.01
Fra_p	72.0%	6.8%	5.9%	5.0%	2.8%	1.7%	1.2%	1.6%	1.0%	0.5%	0.5%	0.4%	0.5%

4.4.3 Solve the parameters k_{AER} and f

For BC, with the simplifications that are made in the section 4.3.2, the mass conservation of indoor concentration can be expressed as follows:

$$\frac{\partial C_i^{in}}{\partial t} = k_{AER} f C_i^{out} - k_{AER} C_i^{in} - k_{DEP} C_i^{in} \tag{4.11}$$

The deposition rate of BC can be calculated and equals 2.12 h^{-1} (Lai and Nazaroff 2000). Therefore, using the DFT, the equation 4.11 for the p-th mode can be rewritten as:

$$j\omega C_i^{in}(t)_p = k_{AER} f C_i^{out}(t)_p - k_{AER} C_i^{in}(t)_p - k_{DEP} C_i^{in}(t)_p \tag{4.12}$$

When p>0, the p^{th} mode of Fourier series can be expressed as:

$$F[p] = (a_p + jb_p)e^{j\omega t} \tag{4.13}$$

With $\omega = \frac{2\pi}{NT} \times p$ and T is one hour. For the sake of clarity, T is omitted hereafter.

The concentrations can both be expressed using the DFT, with the p^{th} Fourier coefficients a_{p_in}, b_{p_in} for the indoor concentrations, and a_{p_out} and b_{p_out} for the outdoor concentrations. These coefficients are presented in Tables 4.3 and 4.4.

Table 4.3 Outdoor coefficients a_{out} and b_{out} for each mode.

mode	0	1	2	3	4	5	6	7	8	9	10	11	12
a_{p_out}	2.300	-0.311	-0.162	0.365	0.071	-0.026	-0.025	0.147	0.044	0.039	-0.003	0.032	-0.038
b_{p_out}	0	-0.097	0.766	0.155	-0.100	0.019	0.119	-0.001	0.015	0.050	0.016	-0.041	0

Table 4.4 Indoor coefficients a_{in} and b_{in} for each mode.

mode	0	1	2	3	4	5	6	7	8	9	10	11	12
a_{p_in}	0.809	-0.131	-0.023	0.127	-0.023	-0.012	0.023	0.013	-0.011	-0.002	0.004	-0.009	0.006
b_{p_in}	0	0.080	0.129	-0.045	-0.059	0.036	0.015	-0.034	0.020	-0.010	0.011	0.002	0

For each mode, the parameters k_{AER_p} and f_p can be obtained by solving the equations below:

$$\begin{cases} k_{AER\_p} \cdot a_{p\_in} + k_{DEP} \cdot a_{p\_in} - k_{AER\_p} \cdot f_p \cdot a_{p\_out} = \omega b_{p\_in} \\ k_{AER\_p} \cdot f_p \cdot b_{p\_out} - k_{AER\_p} \cdot b_{p\_in} - k_{DEP} \cdot b_{p\_in} = \omega a_{p\_in}, \end{cases} \tag{4.14}$$

leading to

$$\begin{cases} f_p = \dfrac{\omega(a_{p\_in}^2 + b_{p\_in}^2)}{\omega(a_{p\_in} \cdot a_{p\_out} + b_{p\_in} \cdot b_{p\_out}) - k_{DEP}(a_{p\_in} \cdot b_{p\_out} - b_{p\_in} \cdot a_{p\_out})} \\ k_{AER\_p} = \dfrac{\omega \cdot (a_{p\_in} \cdot a_{p\_out} + b_{p\_in} \cdot b_{p\_out})}{a_{p\_in} \cdot b_{p\_out} - a_{p\_out} \cdot b_{p\_in}} - k_{DEP} \end{cases} \tag{4.15}$$

The model parameters k_{AER} and f can be calculated from those for each mode multiplied by the fraction Fra_p:

$$\begin{cases} k_{AER} = \displaystyle\sum_{p=0}^{N-1} k_{AER_p}\ Fra_p \\ f = \displaystyle\sum_{p=0}^{N-1} f_p\ Fra_p \end{cases} \tag{4.16}$$

As shown in Tables 4.1 and 4.2, for the p^{th} mode, the fractions Fra_p for the outdoor (Fra_{p_out}) and indoor (Fra_{p_in}) amplitudes are slightly different. Therefore, two different estimations of the parameters k_{AER} and f may be obtained depending on whether the fractions Fra_p are those from the indoor or outdoor signals.

For black carbon, the k_{AER} and f computed from the indoor amplitude fractions are $k_{AER} = 4.1$ and $f = 0.39$; the k_{AER} and f computed from the outdoor amplitude fractions are $k_{AER} = 7.2$ and $f = 0.44$. Fig 4.9 shows the comparison between the simulated and measured BC concentrations. The simulations using k_{AER} and f from indoor and outdoor amplitudes show slight differences in the performance of peak values and the general accordance in time variation. Considering the performance of the peak, the k_{AER} and f from outdoor amplitudes are chosen in the H^2I model with the values of $k_{AER} = 7.2$ and $f = 0.44$.

4.5 Modeling of O_3 and NOx in the H^2I model

O_3 and NOx are reactive gaseous species. Except for outdoor-to-indoor exchange and filtration, the indoor concentrations of O_3 and NOx also depend on various factors, such as surface removal rate, and gas chemistry in the stadium with an influence of photolysis reactions. The impact of these factors are discussed in the following sections.

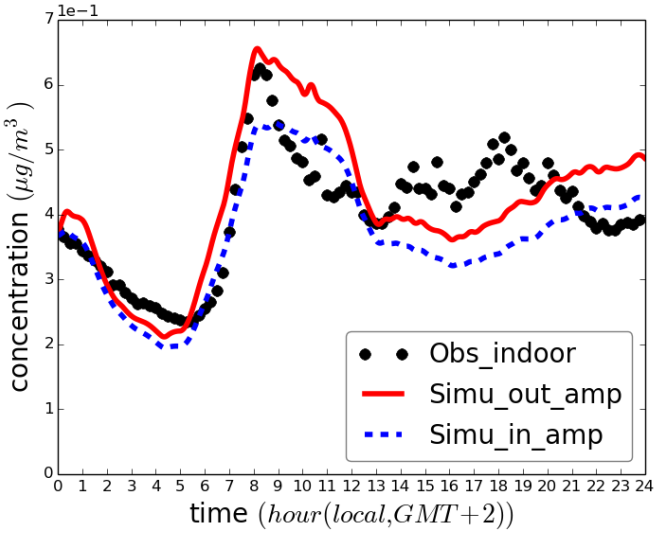

Fig. 4.9 Comparison of observed and simulated BC concentrations using k_{AER} and f from indoor amplitude (blue) and outdoor amplitude (red) of BC measurements.

4.5.1 Time variation of the simulated indoor concentrations

The simulations of the indoor concentrations of O_3, NO and NO_2 are conducted over the whole period of measurement. The comparison between the simulated concentrations and the measurements during the entire period is presented in Fig 4.10 and the hourly averaged concentrations over the period are presented in Fig 4.11. In both figures, the black curve represents the indoor measured concentrations, and the blue curve corresponds to the outdoor measured concentrations multiplied by the filtration factor f. This corresponds to the outdoor concentration after filtration, as represented in the model H^2I. The red curve represents the simulated concentrations using the H^2I model. The simulation does not take into account the concentrations of indoor and outdoor VOC species. The photolysis and the surface reactions are considered. The photolysis coefficients used in the simulation are those estimated for borosilicate windows in H^2I.

In general, for both diurnal concentrations and averaged hourly concentrations, the time variation of the simulated O_3, NO and NO_2 concentrations are in good agreement with the measurements. However, for O_3 and NO_2, the simulated concentrations underestimate the peak values of the measurements, and for NO, the simulated concentrations are overestimated. For O_3, the simulated concentrations are significantly underestimated in the afternoon. The simulated concentrations of NO_2 are also underestimated, but the largest underestimation is in the morning. For NO, the simulated concentrations are overestimated during almost all the day. The comparison of the blue and red curves in Fig 4.10 and Fig 4.11 shows there is a clear separation between the filtrated outdoor concentration (blue) and the indoor simulated (red) one. For O_3, it looks like a simple filtration factor could almost be enough to model the indoor concentration. However, this does not hold for NO and NO_2. The underestimation of O_3 and NO_2 and the overestimation of NO may come from the insufficient conversion between NO and NO_2. As there is no VOC concentrations considered in the simulation, the

chemical regime may not be well represented in the model, where a large quantity of VOC species exist because of the indoor emission from sports equipment and cleaning residues, the outdoor-to-indoor exchange and other processes. In addition, the bias between the simulation and measurements may come from the inaccurate photolysis reaction intensity used in the simulation. Due to the large volume in the stadium, a number of artificial lights are needed to complement the lack of natural light. The detailed light intensity and spectrum are not available in this study. The photolysis reaction rates used in the simulation are thus approximated. This could result in a significant difference from the reality.

In consideration of all of these uncertainties, sensitivity tests are conducted for different processes to study their impact on the concentrations.

4.5.2 Outdoor and indoor NOx concentration ratios

The indoor NOx concentration is lower than outdoor NOx concentration, as shown in Fig 4.12, which compares the hourly-varied indoor/outdoor NOx concentration ratio (IO_NOx) (conducted with NOx concentration in ppb) with the filtration f deduced from the BC concentrations. In the nighttime, IO_NOx is higher than f, whereas in the daytime, IO_NOx is lower than f. The average IO_NOx of the day is 0.456, which matches well with f. Therefore, considering the concentration of NOx, the outdoor NO and NO_2 concentrations deduced are verified to fit the outdoor-to-indoor fraction.

4.5.3 Impact of heterogeneous reactions

In indoor environments, as the volume is limited, heterogeneous reactions on surfaces are more important than in outdoor environments. In order to study the impact of surface reactions in Coubertin, simulations were conducted for a specific day taking or not into account heterogeneous reactions on surfaces, as shown in Fig 4.13, which presents the simulated concentrations of indoor O_3, NO and NO_2 concentrations. Surface reactions have limited impacts on the concentration of O_3, NO and NO_2: the impact is less than 3% for all of these species. The low impact of surface reactions is related to the low friction velocity and the low ratio S/V between the surface and the volume of the room. As the volume of the stadium is larger than other indoor environment, the impact of heterogeneous reactions is much smaller.

4.5.4 Sensitivity tests

4.5.4.1 Impact of VOC concentrations

In this section, the impact of VOC concentrations on the simulated concentrations of O_3, NO and NO_2 are discussed. Lacking comprehensive measurements of indoor and outdoor VOC concentrations in Coubertin, measured VOC concentrations in a room in Marseille are used to estimate the potential impacts of VOC on the concentrations.

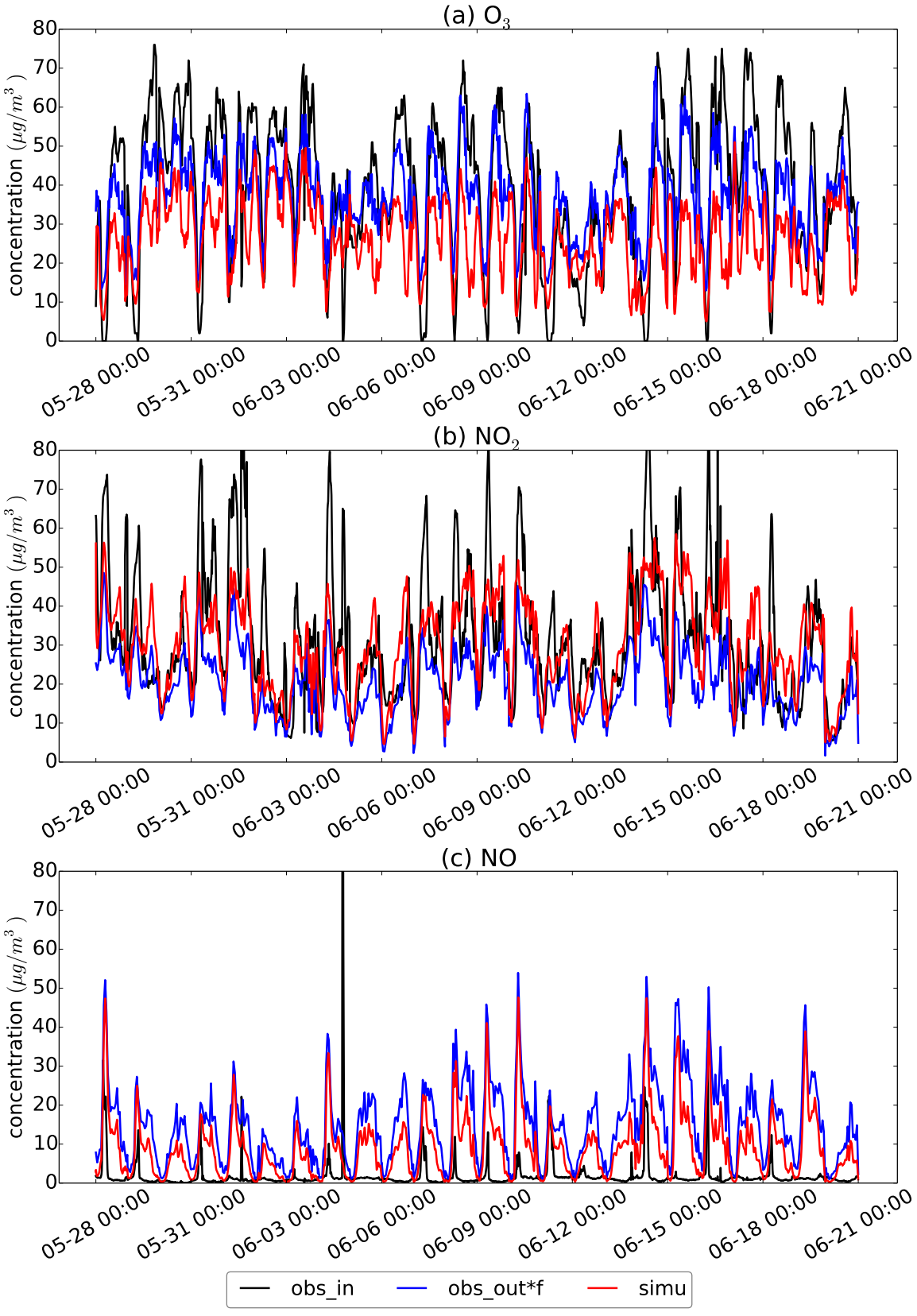

Fig. 4.10 Comparison between the simulated and measured concentrations of O_3, NO and NO_2 during the entire simulated and measured period of measurements.

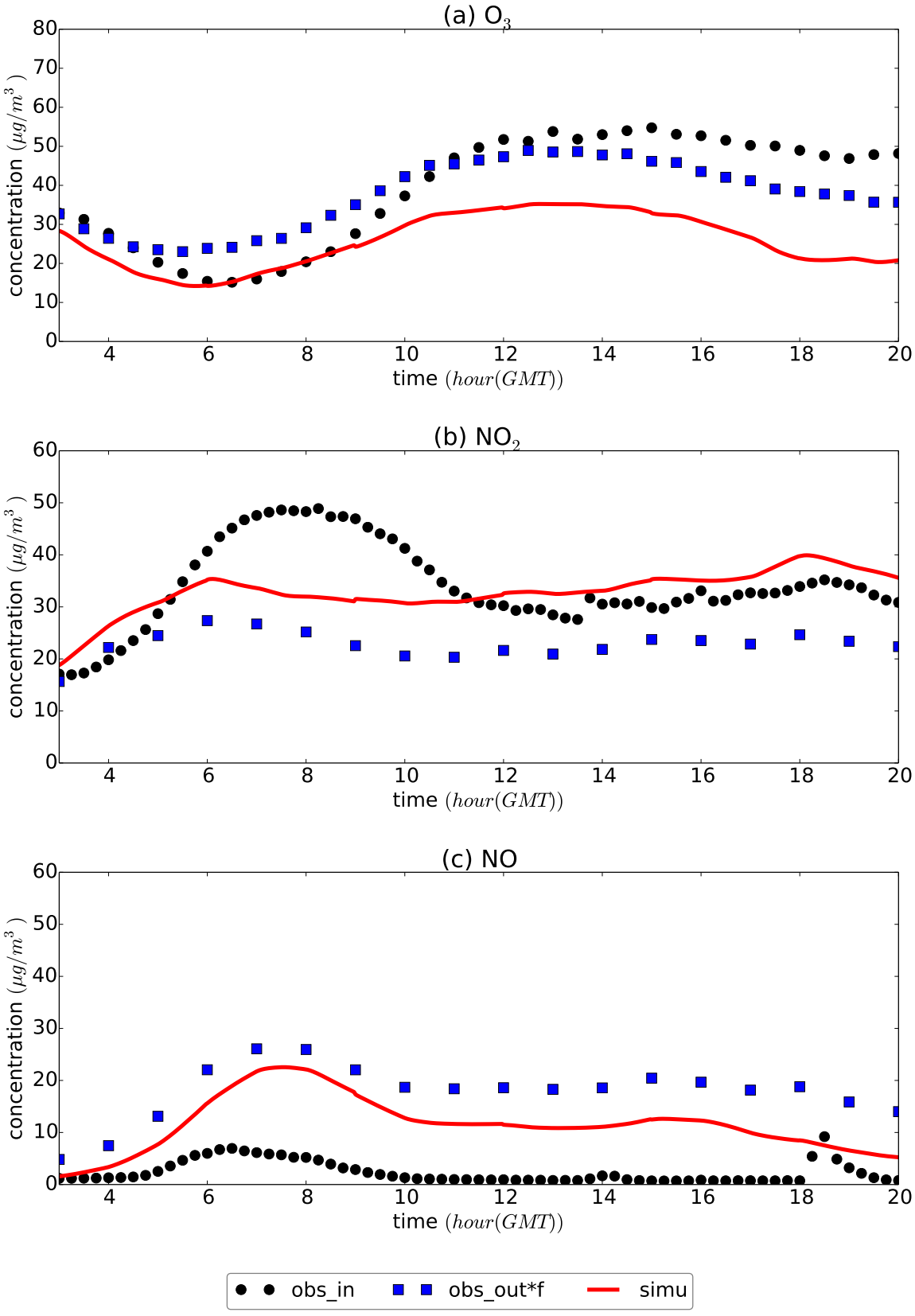

Fig. 4.11 Simulated and measured concentrations of O_3, NO and NO_2. The concentrations are averaged for the same moment in each day of the entire simulated and measured period of measurements.

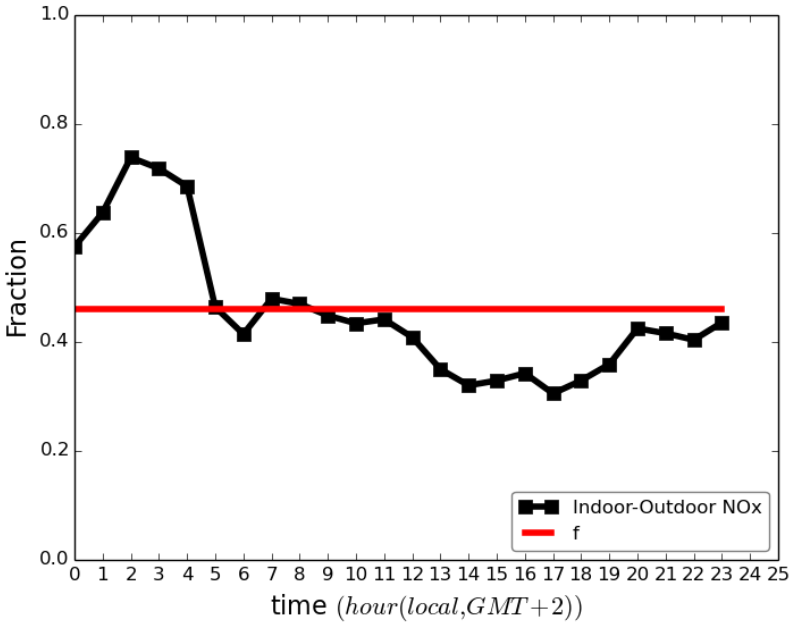

Fig. 4.12 Comparison between hourly indoor/outdoor ratios and the filtration factor f.

In the study of Marseille, 40 VOC species were measured. They were converted into 21 model species and were interpolated every 15 min in the simulation as fixed indoor concentrations. These VOC concentrations are used for the simulation of Coubertin on the 15^{th} of June to study the sensibility of O_3, NO and NO_2 concentrations to VOC concentrations.

The simulations with indoor VOCs last 6 h and 15 min (from 7h45 to 14h) to match with the measurement time of Marseille. The reference simulation is the simulation without VOC species (No VOC), i.e. the simulation presented in previous sections. Compared to the simulation without VOC species, the addition of VOC species leads to an increase of the concentrations of O_3 and NO_2 and a decrease of the concentration of NO, which improves the comparisons to measurements in Coubertin. The impact of VOCs on the concentrations of O_3 and NOx is complex and depends on species. Because of the relatively fast reactions for VOCs/O_3 in indoor atmosphere (Weschler and Shields 1996), the concentrations of O_3 and NOx are impacted with the addition of VOC species.

However, as is shown in Fig 4.8, the comparison between the measurements of Marseille and Coubertin shows significant differences in terms of time variation and order of magnitude of concentrations. Further sensitivity tests are therefore conducted by multiplying the VOC concentrations of Marseille by different factors from 2 to 4. As done previously, these VOC concentrations are used in the H^2I model as indoor measurement records to study the impact on the air quality in Coubertin. Fig 4.14 shows the results of the sensitivity tests, and the comparison with the measurements. The VOC concentrations can improve the simulated results by increasing the concentrations of O_3 and NO_2 and decreasing the concentrations of NO. For NOx, higher are the added VOC concentrations, better are the comparisons to the measurements. The addition of VOCs favors the conversion from NO to NO_2. For O_3, when the addition of VOC concentrations are 2 times the VOCs in Marseille, the

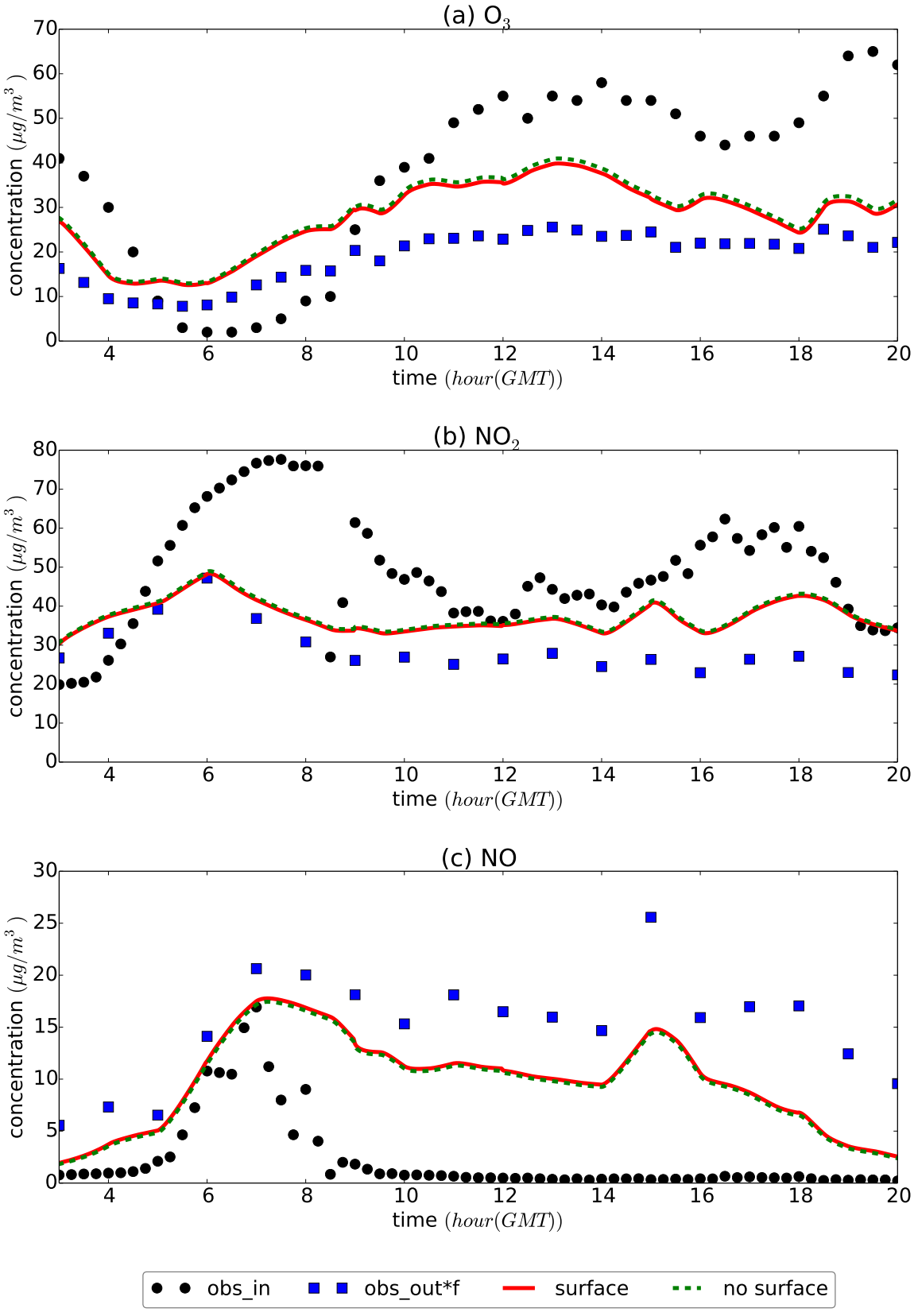

Fig. 4.13 O_3, NO and NO_2 concentrations with and without heterogeneous reactions on surfaces.

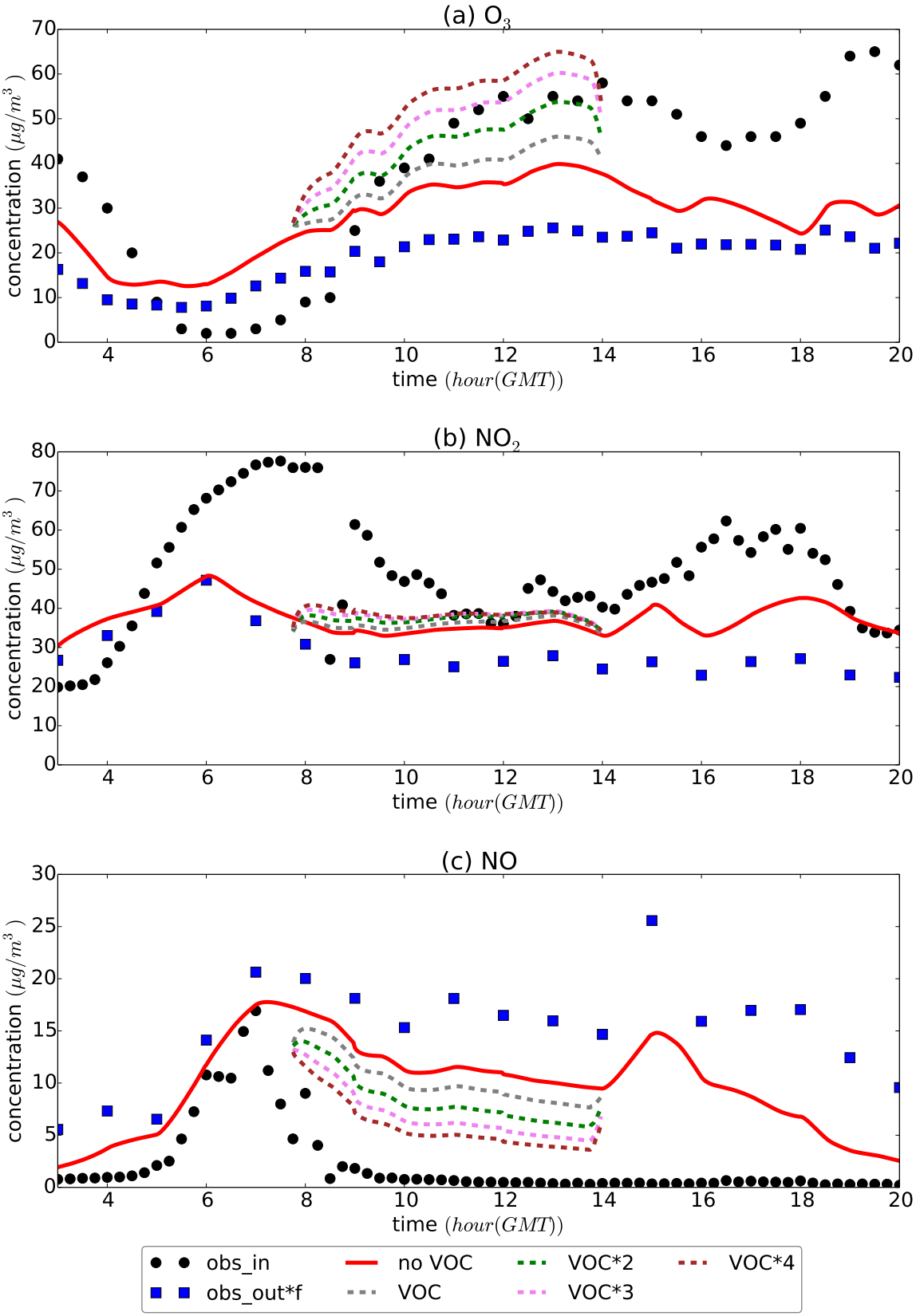

Fig. 4.14 Sensitivity test : impact of VOC concentrations on O_3, NO and NO_2.

simulation reproduces the indoor concentration best compared with the measurements. The sensitivity tests with VOC indoor concentrations show the significant potential impact of the VOCs on O_3, NO and NO_2 concentrations. Future studies can be improved if indoor and outdoor VOC concentrations are available for the input of the study.

4.5.4.2 Impact of photolysis

Lacking measurements for the light intensity and spectrum in the grand hall, the magnitude of photolysis is uncertain in Coubertin. In order to study the impact of photolysis on the concentrations of O_3 and NOx in Coubertin, 3 different set of photolysis rates are used to test the sensitivity of indoor air quality to photolysis reactions. These rates correspond to different light intensities, among which two correspond to indoor environments with UVs-blocking windows and borosilicate windows, and the other corresponds to the outdoor environment.

The sensitivity simulations were conducted for 6 h and 15 min with VOC concentrations from the study in Marseille. The reference case does not take into account VOC concentrations but considers the photolysis rates for borosilicate windows.

Fig 4.15 presents the sensitivity of O_3, NO and NO_2 to photolysis reactions. Generally, the activation of photolysis reactions increase the concentration of O_3 and NO, but decrease the concentration of NO_2. The activation of photolysis leaded to the formation of O_3 due to the decomposition of NO_2. O_3 and NOx concentrations are sensitive to photolysis reactions. For O_3, the increase ranges from 8% to 191% on average, according to different photolysis constant used. The decrease of NO_2 ranges from 5% to 27% and the increase of NO ranges from 15% to 67%.

Therefore, photolysis reactions can be a key factor that impacts the concentration of O_3, NO and NO_2 in the stadium. In the simulation, the photolysis rate corresponding to the wind filtration using UV-blocking windows has a better agreement with measurements, which indicated that the photolysis rate inside the stadium could be low. Either the intensity of indoor light radiation is low or the wavelength range is short. As the light intensity and the light spectrum are not available in the stadium, the quantitative accuracy cannot be determined in our simulations.

4.6 Conclusions

In this chapter, the indoor air quality in an enclosed stadium is studied. Measurements of the geometric parameters and indoor and outdoor air quality are conducted for Pierre de Coubertin stadium by the partners of the project, which offer the input conditions for the modeling of the indoor air quality in the stadium, and provide a credible reference for the model evaluation.

The 0D IAQ model H^2I, which takes into account not only the atmospheric chemistry in gas phase, but also heterogeneous chemistry on surfaces, is used for the modeling of the air quality in the stadium. The model parameters of deposition are determined using the simulation results of the CFD modeling for the same indoor space conducted by our colleagues.

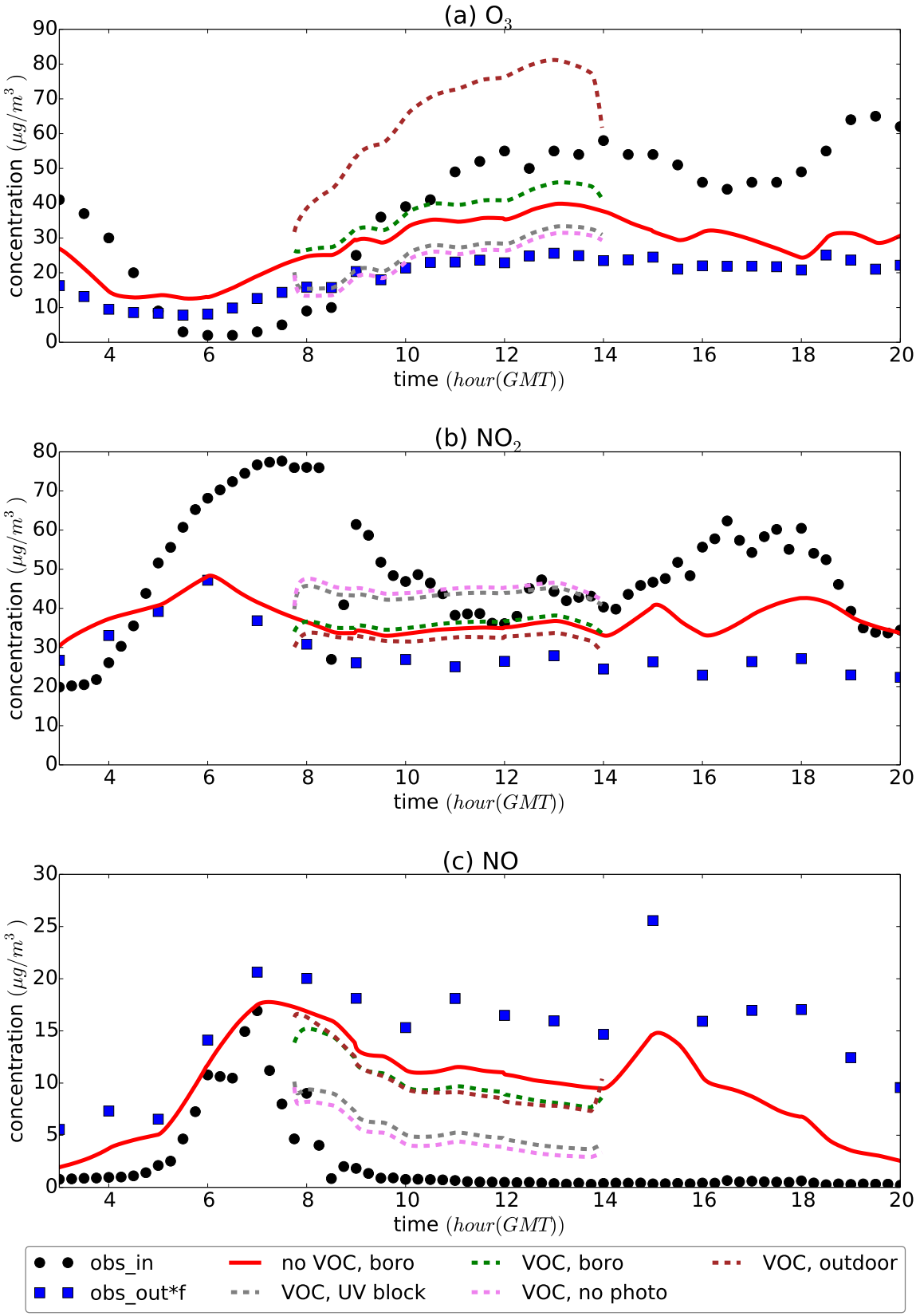

Fig. 4.15 Sensitivity test: impact of photolysis on O_3, NO and NO_2.

The model parameters of ventilation are determined by analyzing the indoor and outdoor concentrations of black carbon. Regarded as an inert matter, only the ventilation and the deposition processes are considered in the modeling of BC. The outdoor to indoor exchange rate k_{AER} and the filtration factor f are determined numerically by the Fourier transformation of the mass conservation equation for the experimental indoor and outdoor concentrations of BC.

These parameters are used in the H^2I model for simulating the indoor concentrations of O_3 and NOx (NO and NO_2) in the stadium. Simulations are performed for 24 days from 28^{th} of May to 20^{th} of June in the year of 2021, when the measurements were also conducted during this period.

The simulated results of the entire period and the daily averaged values show a good agreement in the time variation of the indoor concentrations of O_3 and NOx. However, compared with the measurements, the simulations underestimate the peak values of O_3 and NO_2 but overestimate the concentration of NO. Due to the uncertainties of various factors in the simulation, the inconsistency between the simulation results and the measured values may be explained by the lack of VOC concentrations and the bias of parameters in photochemical reactions. In order to improve the simulation results and study the impact of different processes on the indoor air quality, sensitivity tests are conducted for the surface reactions, photolysis and VOC concentrations. The surface reactions lead to a decrease of O_3 and NO_2 and an increase in NO concentration. Due to the smaller surface/volume ratio in the stadium than in other indoor environment, the impact of surface reactions are limited. Although the indoor VOC concentrations are not precised in the simulation, the addition of VOC species does increase the conversion between NO and NO_2, which results in the increase of NO_2 and O_3, and the reduction in NO concentrations. Higher the VOC concentrations added in the simulation, higher the impact of VOCs acted on O_3 and NOx. The different coefficients in photolysis reactions may also impact significantly the concentration of pollutants in the stadium. Because of the uncertainty in light intensity and spectrum in the stadium, different types of photolysis reactions have been applied in the simulation.

In this study, a simplified 0D IAQ model is used to simulate the air quality in an enclosed stadium. Due to the uncertainty of various parameters and the limitation in 0D model, although the general time variation is well reproduced for different species, the peak values are not simulated well with the model performance. In the future study, more input conditions are needed to make the simulation more accurate. The 0D H^2I model can also be coupled to the 3D CFD model, to take into account the aeraulic impact of the airflow in the 3D space. In addition, different conditions considering or not the public can be modeled to help predicting the air quality in the stadium with sports events.

4.7 Appendix

4.7.1 Measurement data of VOCs in Coubertin

Table 4.5 Measurement VOC concentrations in Coubertin on the 15^{th} June.

species	8-10h	10-12h	12-14h	14-16h	16-18h	18-20h	20-22h	22-24h
Dichloromethane	0.3	0.3	331.2	0.3	0.3	0.3	65.5	0.3
Acetic acid	0.3	2.4	0.3	1	0.3	1.1	1.3	1.7
2-Butanone	4	7.1	4.5	2.8	5.1	5.8	4.6	2.4
Benzene	2	3.2	1.5	1.5	2.5	2.7	2.2	0
Silanediol, dimethyl-	19.6	3.7	21.1	10.8	8.7	18.3	12.4	25.6
Toluene	6.3	3.5	3.2	2.6	2	2.9	3	2
Cyclotrisiloxane, hexamethyl-	153	55.1	41.2	34	36.1	56.8	34.1	87.8
2,4-Dimethyl-1-heptene	4.1	2.5	1.9	1.7	1.7	2.2	1.5	3.9
Oxime-, methoxy-phenyl-	2.6	0.3	3.2	1	0.3	3.7	8.9	5.4
Styrene	1.3	1	0.8	1.1	0.8	0.3	0.8	0.3
Cyclotetrasiloxane, octamethyl-	70.3	10	6.7	6.3	6.7	6.8	5.4	9.2
Benzaldehyde	1.1	0.9	0.8	0.9	0.8	0.3	0.3	0.3
Octanal	1	0.3	0.3	1.9	1.1	1.1	1.3	1.1
2-Propanol, 1-(2-methoxy-1-methylethoxy)- (DPGME)	1	0.3	0.3	0.3	0.3	0.3	0.3	0.3
1-Hexanol, 2-ethyl-	4.7	0.3	0.3	1.1	0.3	0.3	0.6	0.3
Eucalyptol	5.4	0.3	0.3	0	0.3	0.3	0.3	0.3
2-Phenyl-2-propanol	5.8	2.6	2.6	3.3	2.4	2.7	2.1	2.9
Nonanal	4	4	4.2	9	5.2	5	7.1	5.4
Cyclopentasiloxane, decamethyl-	9.1	1.7	1.5	1.1	1.2	1.3	1.8	2.3
Camphre	4.1	0.3	0.3	0.3	0.3	0.3	0.3	0.3
Decanal	2.8	3.3	3.1	4.3	3.4	4	4.1	3.8

Continued on next page

Table 4.5 – continued from previous page

species	8-10h	10-12h	12-14h	14-16h	16-18h	18-20h	20-22h	22-24h
Thiophene, tetrahydro-, 1,1-dioxide	82	69.4	53.1	44	45	53.7	36.6	69.9
Cyclohexasiloxane, dodecamethyl-	2.8	1	0.7	1.1	0	1.1	1.2	1.3
Hexadecamethyl octasiloxane	1.3	1.2	1.4	1.1	0.8	1.9	1.1	1.9
Alcane ramifié C15	3	2.5	3.2	3.7	3.6	4	3.6	5
Pentadecane	1.8	0.9	2.2	2.6	1.3	2.6	2.3	2.1
Hexadecane	1.9	2	1.9	2.2	1.3	0	2.5	2.4
Diethyl Phthalate	42	23.7	15.6	13.4	13.7	15.9	11.3	20.1
Diisobutyl phthalate	22.9	6.1	0.3	0.3	0.3	0.3	0.3	0.3
Dibutyl phthalate	96.9	38.2	14.7	13.7	3.4	6.5	0.3	0.3
Ethyl acétate	1.1	2.3	2.3	0.3	0.3	0.5	0.3	0.3
Ethyl tert-butyl éther	0.3	1	0.3	0.3	0.4	1.2	0.3	2.2
3,5-Dithiahexanol 5,5-dioxide	11.3	3	7.5	15.9	14.5	38	12.5	48
2,2-Diméthylhexane	1.5	1.8	5.1	0.7	0.3	0.4	0.3	0.3
Heptane	1.5	1.1	1.2	1.7	0.3	0.9	0.7	2.2
Hexanal	1	0.3	0.3	0.4	0.3	0.3	0.3	0.3
1-Butoxy-2-propanol	0.3	6.4	5.5	4.2	1.7	0.3	0.3	0.4
2,2,4,6,6-Pentamethylheptane	2.7	2.4	6.4	3.5	1.1	1	0.3	1.7
Dodécane	1.2	1.1	0.7	1	0.3	0.8	0.3	0.6
Tridécane	2.2	1.6	1.9	1.6	0.6	1.3	1.3	2.1
Tétradécane	4.5	3.5	4	3.7	3.2	4.5	4.6	4.7

4.7.2 List of stations

4.7.3 Wall boundary conditions with two friction velocity scales

In order to model the high levels of mixing due to the turbulence in the vicinity of the wall, wall functions are set in the CFD model. A dimensionless analytical velocity value u^+ that represents the realistic non-linear profile of the velocity is proportional to the cell centre to wall dimensionless distance y^+. These two dimensionless parameters depend on the level of turbulent kinetic energy by

Table 4.6 List of stations for the measurement of NOx in 2020 and their distances from Coubertin.

Station	Distance (km)
PA01H	7.16
GEN	10.42
OPERA	6.82
AUT	4.53
BASCH	5.24
BONAP	6.02
CELES	7.86
DEF	6.12
EIFF3	3.8
NEUIL	5.58
PA07	4.62
PA13	7.67
PA18	9.28
HAUS	7.04
BP_EST	4.53
ELYS	5.19
VERS	9.96
PA15L	1.1

the wall shear stress τ_{wall} and the turbulent kinetic energy (two friction velocity scales).

The simplified momentum balance in the first boundary cell is shown as follows:

$$(\mu + \mu_T)\frac{\partial u}{\partial y} = \tau_{wall} \tag{4.17}$$

For high y^+, the friction velocity based on the turbulent kinetic energy in the first cell is presented as follows:

$$u_k = \sqrt{\sqrt{C_\mu}k} \tag{4.18}$$

If y^+ and the intensity of turbulence is low:

$$u_k = \sqrt{g\frac{\nu|\underline{u}^r_{I'}|}{y} + (1-g)\sqrt{C_\mu}k} \tag{4.19}$$

Where g is a blending factor defined as $g = \exp(-\frac{\sqrt{k}y}{11\nu})$ The the friction velocity u^* is defined as:

$$u^* \equiv \frac{\tau_{wall}}{\rho u_k} \tag{4.20}$$

Therefore, equation 4.17 is written as:

$$(1 + \frac{\mu_T}{\mu})\frac{\partial u^+}{\partial y^+_k} = 1 \tag{4.21}$$

Where $u^+ \equiv \frac{|u^r_{I'}|}{u^*}$ and $y^+_k \equiv \frac{yu_k}{\nu}$.

Using the Prandtl mixing lengh theory, the following equation can be obtained:

$$(1 + \kappa y^+_k)\frac{\partial u^+}{\partial y^+_k} = 1 \tag{4.22}$$

Two areas are defined, when $\frac{\mu_T}{\mu} \ll 1$, $\frac{\mu_T}{\mu}$ is neglected in the velocity profile:

$$u^+ = y^+_k \tag{4.23}$$

When $\frac{\mu_T}{\mu} \ll 1$, the velocity profile becomes logarithmic, as:

$$\frac{y^+_k}{u^+} = \frac{y^+_k}{\frac{1}{\kappa}\ln(y^+_k) + C_{log}} \tag{4.24}$$

CHAPTER 5

Conclusions and perspectives

5.1 Conclusions

In this manuscript, indoor and outdoor air qualities in urban areas are modeled with local-scale air quality models. Different physical and chemical processes affecting the transportation and the formation of pollutants are taken into account in the development of numerical tools.

The context of the study is presented in Chapter 1, including the brief introduction of air pollutants and processes, as well as different models that are used in the air quality simulations. Chapter 2, 3, 4 present the modeling of air quality in an urban street canyon and in an enclosed stadium. CFD model is used for simulating the evolution of gaseous and particulate pollutants in the street. Conventional CFD methods in which pollutants are regarded as passive scalars cannot reproduce the interaction between pollutants, leading to the inconsistency with observations. Therefore, a coupled method between the chemical module SSH-aerosol and the CFD model is developed for modeling the street. This allows the activation of gaseous chemistry and aerodynamics, making it possible to reproduce the formation of secondary pollutants. In order to study the impact of trees on the pollutants in the street, tree models are integrated in the model of street, aiming at providing the qualitative evaluation on the tree impact with high efficiency. Aerodynamic impact of trees crowns, which is parameterized according to different tree characteristics, is focused in this study, alongside with the atmospheric dry deposition on leaves surfaces and the impact of tree VOC emissions. Considering indoor air quality, the simulations are conducted through a 0D indoor air quality model which takes heterogeneous chemistry into account. Model parameters of the ventilation are determined with the analysis of Fourier transformation for the indoor and outdoor measured concentrations of black carbon.

The modeling of air quality in the street is realised through the CFD-chemistry coupled model. The grid sensibility and the time step sensibility are analysed to find the most computationally cost-effective method for conducting simulations. The comparison between measured and simulated concentrations of gas species NO_2 and PM_{10} within the street presents a better agreement based on the coupled model than conventional CFD model. However, the black carbon concentration is always underestimated, which may be explained by the underestimation of non-exhaust emissions (tire and road wear). Considering the spatial distribution of pollutants, because of the traffic emissions, the mass and number concentrations of particles are higher in the street than in the background. For all

PM compositions, the particle concentrations are higher in the leeward side of the street than in the windward side at the pedestrian level. Inorganic and organic particles in the street are largely impacted by aerosol dynamics. For inorganic condensables, the increase of their condensation is mainly due to the ammonia emission by traffic. Aerosol dynamics lead to a large increase of ammonium nitrate from precursor gas emitted in the street canyon. The variation of organic aerosols is mainly influenced by the formation of inorganic aerosols and the characteristic of hydrophilic.

The impact of trees on the transportation and formation of pollutants is complex in the street. VOC emissions by trees have a limited impact on condensables, except on extremely-low volatile compounds (ELVOCs) formed from monoterpene autoxidation. Although this increase of ELVOC concentrations may not impact significantly the organic aerosol mass, it could impact the formation of ultrafine particles in the street. As the wind speed above the street strongly impacts the characteristic time of dispersion, low wind speed may lead to more organic condensables produced (by 1% to 7%). The impact of dry deposition deposition depends on pollutants with different solubility and volatility. Deposition is high for HNO_3 with an impact of 6% for urban surfaces and as much as 25% for vegetation. Tree crowns impact pollutant dispersion, causing an accumulation of traffic emissions at the pedestrian level near the leeward side of the street. Therefore, considering the overall impact of trees, concentrations of traffic emitted species (NO, NO_2, CO, NH_3, ISVOCs) increase because of the dominant aerodynamic effects. The presence of trees promotes their accumulation in the street and increase their average concentration. Organic condensables from tree VOC emissions are formed in the street only in the case of low wind speed above the street. For the inorganic condensable HNO_3, the presence of trees leads to a decrease of concentration because of the impact of dry deposition on vegetation. As the limiting factor for the formation of ammonium nitrate in the street is probably NH_3, the inorganic aerosol concentrations could still increase because of the increase of NH_3 concentrations.

The use of the 0D indoor air quality model is also proved to be feasible for simulating the indoor air quality in the stadium. The model parameters determined through the analysis of measured black carbon concentrations present a good agreement in temporal variations with measurements for the simulations of O_3 and NOx, which demonstrates the reasonable choice of the air exchange rate acquired. However, for the order of magnitude of concentrations, the under-estimation of O_3 and NO_2 and the over-estimation of NO cannot be neglected. Various uncertainties for input concentrations in the model may be explained for the bias. Sensitivity tests for different processes are therefore conducted in the simulation to assess whether there is an improvement for approaching the measured concentrations. Because of the large volume in the stadium, the impact of surface reactions is much smaller than in other indoor environments, leading to the variations less than 1% in O_3 and NOx concentrations. The addition of indoor VOC concentrations has a significant impact for improving the simulation results by promoting the conversion from NO to NO_2. Due to the high-NOx chemical regime in the stadium, O_3 concentrations are also increased with the insertion of VOC species. Photolysis rate is another factor which influences substantially the indoor O_3 and NOx concentrations. Sensitivity tests on the photolysis show a non-neglectable impact of window glazing. Photochemical

reactions in the stadium with UV-blocking windows match better with observations.

5.2 Perspectives

This study presents two local scale indoor and outdoor air quality models. The outdoor air quality model is a coupled CFD-chemistry model and the indoor air quality model is a 0D air quality model. To save the computational cost, the outdoor CFD models are built with a simplified 2D geometry, with a perpendicular wind direction. For the indoor air quality modeling, uncertainties of model parameters impact the accuracy of simulated results. In the future study, different possibilities for the model development are discussed in the following sections.

5.2.1 Outdoor air quality model development

For the coupled CFD-chemistry model, first of all, instead of the present 2D geometry, a more realistic 3D geometry should be built as the residence time and reaction rates of pollutants are impacted by urban geometry in more general cases, leading to a shorter time and a higher rate in the 3D street models than in 2D models. Besides of the impact of 3D geometry, different wind directions should also be considered. By comparing the simulation results in different wind directions with measurement, the evaluation of the model performance would be more comprehensive and realiable. In addition, the CFD model might be constructed with more complex street networks, in order to study the interact impact between different streets and to acquire a more representative conclusion for individual districts.

Considering the numerical solution of turbulence and motion of the fluid in CFD models, models based on LES calculation can be developed. Although with higher computational cost, LES models may provide a more accurate performance in simulating flow characteristics, which may result in a better comparison with observations.

For studying the impact of vegetation on the air quality in the street, different vegetation scenarios including a variety of vegetation type and vegetation characteristics, as well as different planting methods can be considered in the study. Sensitivity analysis of these different parameters should be conducted, in order to investigate they influence the impact of vegetation on the local air quality in the street.

5.2.2 Indoor air quality model development

The present H^2I model used in the indoor air quality modeling for an enclosed stadium is an effective simulation tool taking into account various physical and chemical processes. However, the uncertainties of model input conditions lead to the bias between simulated results and measurements.

In the future study, the following parameters can be precised for improving the simulated results. VOC species impact significantly the concentration of other pollutants. While the positive or negative

impacts of VOCs on the increase of O_3 and NOx concentrations depend on different species, as is shown by the sensibility tests, the main composition of VOC species in the stadium and the sources of their emission should be determined. At the same time, photochemical reactions is also an important factor affecting the indoor air quality. Light intensity and light spectrum should be determined in the stadium for acquiring the appropriate photolysis rates in the model. In addition, the outdoor air pollutant composition measurement is not complete, leading to the insufficiency of the outdoor-to-indoor exchange and filtration in species, especially the lack of measurements for some important radicals may result in the inaccuracy in oxidation reactions.

Meanwhile, only black carbon is taken into account as an inert aerosol in the model. Aerosols dynamics are not considered. Since PM is also an essential health menace in indoor environments, the modeling of aerosols should be developed in future models.

REFERENCES

Abhijith, K., Kumar, P., Gallagher, J., McNabola, A., Baldauf, R., Pilla, F., Broderick, B., Di Sabatino, S. and Pulvirenti, B. (2017), 'Air pollution abatement performances of green infrastructure in open road and built-up street canyon environments - A review.', Atmos. Environ. **162**, 71–86.

Anenberg, S. C., Miller, J., Minjares, R., Du, L., Henze, D. K., Lacey, F., Malley, C. S., Emberson, L., Franco, V., Klimont, Z. et al. (2017), 'Impacts and mitigation of excess diesel-related no x emissions in 11 major vehicle markets', Nature **545**(7655), 467–471.

Aranjuelo, I., Erice, G., Nogués, S., Morales, F., Irigoyen, J. J. and Sánchez-Díaz, M. (2008), 'The mechanism (s) involved in the photoprotection of psii at elevated co2 in nodulated alfalfa plants', Environmental and Experimental Botany **64**(3), 295–306.

Archambeau, F., Méchitoua, N. and Sakiz, M. (2004), 'Code Saturne: a finite volume code for the computation of turbulent incompressible flows-Industrial applications', Int. J. Finite Vol. **1**(1).
URL: *https://hal.archives-ouvertes.fr/hal-01115371/document*

Arpaci, V. S. and Larsen, P. S. (1984), Convection heat transfer, Prentice Hall.

Baik, J., Kang, Y. and Kim, J. (2007), 'Modeling reactive pollutant dispersion in an urban street canyon', Atmos. Environ. **41**(5), 934–949.

Baker, J., Walker, H. and Cai, X. (2004), 'A study of the dispersion and transport of reactive pollutants in and above street canyons—a large eddy simulation', Atmos. Environ. **38**(39), 6883–6892.

Baldocchi, D., Hicks, B. and Camara, P. (1987), 'A canopy stomatal resistance model for gaseous deposition to vegetated surfaces', Atmos. Environ. **21**(1), 91–101.

Baraldi, R., Chieco, C., Neri, L., Facini, O., Rapparini, F., Morrone, L., Rotondi, A. and Carriero, G. (2019), 'An integrated study on air mitigation potential of urban vegetation: from a multi-trait approach to modeling', Urban For Urban Green. **41**, 127–138.

Belcher, S. E. (2005), 'Mixing and transport in urban areas', Philosophical Transactions of the Royal Society A: Mathematical, Physical and Engineering Sciences **363**(1837), 2947–2968.

Bennett, J., Davy, P., Trompetter, B., Wang, Y., Pierse, N., Boulic, M., Phipps, R. and Howden-Chapman, P. (2019), 'Sources of indoor air pollution at a new zealand urban primary school; a case study', Atmospheric Pollution Research **10**(2), 435–444.

Bishop, G. A. and Stedman, D. H. (2015), 'Reactive nitrogen species emission trends in three light-/medium-duty united states fleets', Environmental Science and Technology **49**(18), 11234–11240.

Blackman, K., Perret, L. and Savory, E. (2015), 'Effect of upstream flow regime on street canyon flow mean turbulence statistics', Environmental Fluid Mechanics **15**(4), 823–849.

Blocken, B., Tominaga, Y. and Stathopoulos, T. (2013), 'Cfd simulation of micro-scale pollutant dispersion in the built environment', Building and Environment **64**, 225–230.

Brown, S. (1997), National state of the environment report - indoor air quality. soe technical report series, dept. environment, sports territories, canberra, Technical report.

Buccolieri, R., Gromke, C., Di Sabatino, S. and Ruck, B. (2009), 'Aerodynamic effects of trees on pollutant concentration in street canyons.', Sci. Total Environ. **407**(19), 5247–5256.

Cabaraban, M., Kroll, C., Hirabayashi, S. and Nowak, D. (2013), 'Modeling of air pollutant removal by dry deposition to urban trees using a WRF/CMAQ/i-Tree Eco coupled system', Environ. Pollut. **176**, 123–133.

Calfapietra, C., Fares, S., Manes, F., Morani, A., Sgrigna, G. and Loreto, F. (2013), 'Role of biogenic volatile organic compounds (BVOC) emitted by urban trees on ozone concentration in cities: a review. ', Environ. Pollut. **183**, 71–80.

Carruthers, D., Holroyd, R., Hunt, J., Weng, W., Robins, A., Apsley, D., Thompson, D. and Smith, F. (1994), 'Uk-adms: A new approach to modelling dispersion in the earth's atmospheric boundary layer', Journal of wind engineering and industrial aerodynamics **52**, 139–153.

Carslaw, D. C. and Beevers, S. D. (2005), 'Estimations of road vehicle primary no2 exhaust emission fractions using monitoring data in london', Atmospheric Environment **39**(1), 167–177.

Castelli, S. T., Armand, P., Tinarelli, G., Duchenne, C. and Nibart, M. (2018), 'Validation of a lagrangian particle dispersion model with wind tunnel and field experiments in urban environment', Atmospheric environment **193**, 273–289.

Chaloulakou, A. and Mavroidis, I. (2002), 'Comparison of indoor and outdoor concentrations of co at a public school. evaluation of an indoor air quality model', Atmospheric Environment **36**(11), 1769–1781.

Chang, J. C. and Hanna, S. R. (2004), 'Air quality model performance evaluation', Meteorology and Atmospheric Physics **87**(1-3), 167–196.

Chen, H., Kwong, J. C., Copes, R., Tu, K., Villeneuve, P. J., Van Donkelaar, A., Hystad, P., Martin, R. V., Murray, B. J., Jessiman, B. et al. (2017), 'Living near major roads and the incidence of dementia, Parkinson's disease, and multiple sclerosis: a population-based cohort study', The Lancet. **389**(10070), 718–726.

Cheng, R. J., Hwu, J. R., Kim, J. T. and Leu, S.-M. (1987), 'Deterioration of marble structures the role of acid rain', Analytical Chemistry **59**(2), 104A–106A.

Cheng, Y., Lee, S., Gu, Z., Ho, K., Zhang, Y., Huang, Y., Chow, J. C., Watson, J. G., Cao, J. and Zhang, R. (2015), 'Pm2. 5 and pm10-2.5 chemical composition and source apportionment near a hong kong roadway', Particuology **18**, 96–104.

Chérin, N., Roustan, Y., Musson-Genon, L. and Seigneur, C. (2015), 'Modelling atmospheric dry deposition in urban areas using an urban canopy approach.', Geosci. Model Dev. **8**(3), 893–910.

Chrit, M., Sartelet, K., Sciare, J., Pey, J., Marchand, N., Couvidat, F., Sellegri, K. and Beekmann, M. (2017), 'Modelling organic aerosol concentrations and properties during ChArMEx summer campaigns of 2012 and 2013 in the western Mediterranean region', Atmos. Chem. Phys. **17**, 12509–12531.

Churkina, G., Grote, R., Butler, T. and Lawrence, M. (2015), 'Natural selection? Picking the right trees for urban greening.', Environ. Sci. Policy. **47**, 12–17.

Churkina, G., Kuik, F., Bonn, B., Lauer, A., Grote, R., Tomiak, K. and Butler, T. (2017), 'Effect of VOC emissions from vegetation on air quality in berlin during a heatwave.', Environ. Sci. Technol. **51**, 61206130.

Cline, W. R. (1991), 'Scientific basis for the greenhouse effect', The Economic Journal **101**(407), 904–919.

Crowder, T. M., Rosati, J. A., Schroeter, J. D., Hickey, A. J. and Martonen, T. B. (2002), 'Fundamental effects of particle morphology on lung delivery: predictions of stokes' law and the particular relevance to dry powder inhaler formulation and development', Pharmaceutical research **19**, 239–245.

Currie, B. and Bass, B. (2008), 'Estimates of air pollution mitigation with green plants and green roofs using the UFORE model', Urban. Ecosyst. **11**(4), 409–422.

Curtius, J. (2009), Nucleation of atmospheric particles, in 'EPJ Web of Conferences', Vol. 1, EDP Sciences, pp. 199–209.

Dai-Zhang, W., Xin, J., Yong-Rong, B., Ren-Kou, X. and Ji-Zheng, H. (2003), 'The impacts of acidic deposition on ecoenvironment', Chinese Journal of Eco-Agriculture **11**(1), 107–109.

Danel, V. (2019), 'Airborne particulate matter and their health effects', Available at `https://www.encyclopedie-environnement.org/en/health/airborne-particulate-health-effects/` (2019/08/16).

Dargay, J., Gately, D. and Sommer, M. (2007), 'Vehicle ownership and income growth, worldwide: 1960-2030', The energy journal **28**(4).

Dentener, F., Drevet, J., Lamarque, J.-F., Bey, I., Eickhout, B., Fiore, A. M., Hauglustaine, D., Horowitz, L. W., Krol, M., Kulshrestha, U. et al. (2006), 'Nitrogen and sulfur deposition on regional and global scales: A multimodel evaluation', Global biogeochemical cycles **20**(4).

Di Sabatino, S., Buccolieri, R., Pulvirenti, B. and Britter, R. (2007), 'Simulations of pollutant dispersion within idealised urban-type geometries with cfd and integral models', Atmospheric environment **41**(37), 8316–8329.

Dodman, D. (2009), 'Urban density and climate change', Analytical review of the interaction between urban growth trends and environmental changes (1).

Du, Y., Xu, X., Chu, M., Guo, Y. and Wang, J. (2016), 'Air particulate matter and cardiovascular disease: the epidemiological, biomedical and clinical evidence', Journal of thoracic disease **8**(1), E8.

Ehn, M., Thornton, J., Kleist, E., Sipilä, M., Junninen, H., Pullinen, I., Springer, M., Rubach, F., Tillmann, R., Lee, B., Lopez-Hilfiker, F., Andres, S., Acir, I., Rissanen, M., Jokinen, T., Schobesberger, S., Kangasluoma, J., Kontkanen, J., Nieminen, T., Kurtén, T., Nielsen, L. B., Jørgensen, S., Kjaergaard, H., Canagaratna, M., Dal Maso, M., Berndt, T., Petäjä, T., Wahner, A., Kerminen, V., Kulmala, M., Worsnop, D. R., Wildt, J. and Mentel, T. (2014), 'A large source of low-volatility secondary organic aerosol."', Nature. **506**, 476–479.

EMEP/EEA (2019), 'Emep/eea air pollutant emission inventory guidebook 2019, eea report no 13/2019, european en- vironment', Available at `https://www.eea.europa.eu/publications/emep-eea-guidebook-2019` (last access: 14 March 2022).

Erisman, J., Van Pul, A. and Wyers, P. (1994), 'Parametrization of surface resistance for the quantification of atmospheric deposition of acidifying pollutants and ozone.', Atmos. Environ. **28**(16), 2595–2607.

Escobedo, F., Kroeger, T. and Wagner, J. (2011), 'Urban forests and pollution mitigation: Analyzing ecosystem services and disservices', Environ. Pollut. **159**(8-9), 2078–2087.

Farmer, D. K., Boedicker, E. K. and DeBolt, H. M. (2021), 'Dry deposition of atmospheric aerosols: approaches, observations, and mechanisms', Annual review of physical chemistry **72**, 375–397.

Febo, A. and Perrino, C. (1991), 'Prediction and experimental evidence for high air concentration of nitrous acid in indoor environments', Atmospheric Environment. Part A. General Topics **25**(5-6), 1055–1061.

Fenger, J. (1999), 'Urban air quality', Atmospheric environment **33**(29), 4877–4900.

Ferrero, E., Alessandrini, S., Anderson, B., Tomasi, E., Jimenez, P. and Meech, S. (2019), 'Lagrangian simulation of smoke plume from fire and validation using ground-based lidar and aircraft measurements', Atmospheric Environment **213**, 659–674.

Fesquet, C., Dupont, S., Drobinski, P., Dubos, T. and Barthlott, C. (2009), 'Impact of terrain heterogeneity on coherent structure properties: numerical approach.', Bound.-Lay. Meteorol. **133**(1), 71–92.

Finkelstein, M. and Jerrett, M. (2007), 'A study of the relationships between Parkinson's disease and markers of traffic-derived and environmental manganese air pollution in two Canadian cities', Environ. Res. **104**(3), 420–432.

Fiorentino, E.-A., Wortham, H. and Sartelet, K. (2020), 'Combining homogeneous and heterogeneous chemistry to model inorganic compounds concentrations in indoor environments: the H 2 I model (v1. 0)', Geoscientific Model Development Discussions pp. 1–60.

Forouzanfar, M., Afshin, A., Alexander, L., Anderson, H., Bhutta, Z., Biryukov, S., Brauer, M., Burnett, R. and Cercy, K. (2016), 'Global, regional, and national comparative risk assessment of 79 behavioural, environmental and occupational, and metabolic risks or clusters of risks, 1990-2013;2015: a systematic analysis for the Global Burden of Disease Study 2015.', The Lancet. **388**(10053), 1659–1724.

Foyer, C. H. and Harbinson, J. (2019), Oxygen metabolism and the regulation of photosynthetic electron transport, in 'Causes of photooxidative stress and amelioration of defense systems in plants', CRC press, pp. 1–42.

Friedlander, S. K. (1973), 'Chemical element balances and identification of air pollution sources', Environmental science and technology **7**(3), 235–240.

Fu, K. and Liang, D. (2016), 'The conservative characteristic fd methods for atmospheric aerosol transport problems', Journal of Computational Physics **305**, 494–520.

Fuchs, N. (1965), 'The mechanics of aerosols', Quarterly Journal of the Royal Meteorological Society **91**(388), 249–249.

Fuller, R., Landrigan, P. J., Balakrishnan, K., Bathan, G., Bose-O'Reilly, S., Brauer, M., Caravanos, J., Chiles, T., Cohen, A., Corra, L. et al. (2022), 'Pollution and health: a progress update', The Lancet Planetary Health .

Galante Amino, H. (2022), Developpent of a CFD time scheme for indoor airflow applications, Theses, École des Ponts ParisTech.
URL: *https://pastel.archives-ouvertes.fr/tel-04004367*

Gao, S., Kurppa, M., Chan, C. K. and Ngan, K. (2022), 'Dispersion of cooking-generated aerosols from an urban street canyon', Atmospheric Chemistry and Physics **22**(4), 2703–2726.

García, C., Martín, F., De Tiedra, P. and Cambronero, L. G. (2007), 'Pitting corrosion behaviour of pm austenitic stainless steels sintered in nitrogen–hydrogen atmosphere', Corrosion Science **49**(4), 1718–1736.

Gariazzo, C., Papaleo, V., Pelliccioni, A., Calori, G., Radice, P. and Tinarelli, G. (2007), 'Application of a lagrangian particle model to assess the impact of harbour, industrial and urban activities on air quality in the taranto area, italy', Atmospheric Environment **41**(30), 6432–6444.

Garmory, A., Kim, I., Britter, R. and Mastorakos, E. (2009), 'Simulations of the dispersion of reactive pollutants in a street canyon, considering different chemical mechanisms and micromixing', Atmos. Environ. **43**(31), 4670–4680.

Garrett, T. J., Radke, L. F. and Hobbs, P. V. (2002), 'Aerosol effects on cloud emissivity and surface longwave heating in the arctic', Journal of the Atmospheric Sciences **59**(3), 769–778.

Goliff, W. S., Stockwell, W. R. and Lawson, C. V. (2013), 'The regional atmospheric chemistry mechanism, version 2', Atmospheric Environment **68**, 174–185.

Gottlicher, S., Gager, M., Mandl, N. and Mareckova, K. (2010), European Union Emission Inventory Report 1990–2008 under the UNECE Convention on Long-range Transboundary Air Pollution (LRTAP), Technical report, European Environment Agency.

Gouesbet, G. and Berlemont, A. (1999), 'Eulerian and lagrangian approaches for predicting the behaviour of discrete particles in turbulent flows', Progress in Energy and Combustion Science **25**(2), 133–159.

Grawe, D., Cai, X. and Harrison, R. (2007), 'Large eddy simulation of shading effects on NO_2 and O_3 concentrations within an idealised street canyon', Atmos. Environ. **41**(34), 7304–7314.

Greaver, T. L., Sullivan, T. J., Herrick, J. D., Barber, M. C., Baron, J. S., Cosby, B. J., Deerhake, M. E., Dennis, R. L., Dubois, J.-J. B., Goodale, C. L. et al. (2012), 'Ecological effects of nitrogen and sulfur air pollution in the us: what do we know?', Frontiers in Ecology and the Environment **10**(7), 365–372.

Gromke, C. and Ruck, B. (2007), 'Influence of trees on the dispersion of pollutants in an urban street canyon—experimental investigation of the flow and concentration field.', Atmos. Environ. **41**(16), 3287–3302.

Grøntoft, T. and Raychaudhuri, M. R. (2004), 'Compilation of tables of surface deposition velocities for o3, no2 and so2 to a range of indoor surfaces', Atmospheric Environment **38**(4), 533–544.

Guenther, A. B., Zimmerman, P. R., Harley, P. C., Monson, R. K. and Fall, R. (1993), 'Isoprene and monoterpene emission rate variability: model evaluations and sensitivity analyses', J. Geophys. Res-Atmos. **98**(D7), 12609–12617.

Guenther, A., Geron, C., Pierce, T., Lamb, B., Harley, P. and Fall, R. (2000), 'Natural emissions of non-methane volatile organic compounds, carbon monoxide, and oxides of nitrogen from North America', Atmos. Environ. **34**(12-14), 2205–2230.

Guenther, A., Hewitt, C., Erickson, D., Fall, R., Geron, C., Graedel, T., Harley, P., Klinger, L., Lerdau, M., McKay, W. et al. (1995), 'A global model of natural volatile organic compound emissions', J. Geophys. Res. **100**(D5), 8873–8892.

Guenther, A., Karl, T., Harley, P., Wiedinmyer, C., Palmer, P. and Geron, C. (2006), 'Estimates of global terrestrial isoprene emissions using MEGAN (Model of Emissions of Gases and Aerosols from Nature)', Atmos. Chem. Phys. **11**(6), 2181–3210.

Guimet, V. and Laurence, D. (2002), A linearised turbulent production in the k-ε model for engineering applications, in 'Engineering Turbulence Modelling and Experiments 5', pp. 157–166.

Han, L., Zhou, W., Li, W., Meshesha, D. T., Li, L. and Zheng, M. (2015), 'Meteorological and urban landscape factors on severe air pollution in beijing', Journal of the Air and Waste Management Association **65**(7), 782–787.

Hanna, S. R., Hansen, O. R. and Dharmavaram, S. (2004), 'Flacs cfd air quality model performance evaluation with kit fox, must, prairie grass, and emu observations', Atmospheric Environment **38**(28), 4675–4687.

Harten, A. (1984), 'On a class of high resolution total-variation-stable finite-difference schemes', SIAM Journal on Numerical Analysis **21**(1), 1–23.

He, J., Yu, Y., Liu, N. and Zhao, S. (2013), 'Numerical model-based relationship between meteorological conditions and air quality and its implication for urban air quality management', International Journal of Environment and Pollution **53**(3-4), 265–286.

He, J., Yu, Y., Xie, Y., Mao, H., Wu, L., Liu, N. and Zhao, S. (2016), 'Numerical model-based artificial neural network model and its application for quantifying impact factors of urban air quality', Water, Air, and Soil Pollution **227**, 1–16.

Hicks, B., Baldocchi, D., Meyers, T., Hosker, R. and Matt, D. (1987), 'A preliminary multiple resistance routine for deriving dry deposition velocities from measured quantities.', Water. Air. Soil. Poll. **36**(3-4), 311–330.

Hirabayashi, S., Kroll, C. and Nowak, D. (2012), 'Development of a distributed air pollutant dry deposition modeling framework.', Environ. Pollut. **171**, 9–17.

Holton, J. R. (2004), 'An introduction to dynamic meteorology. forth edition', Department of Atmo .

Jacobson, M. Z. and Turco, R. P. (1995), 'Simulating condensational growth, evaporation, and coagulation of aerosols using a combined moving and stationary size grid', Aerosol science and technology **22**(1), 73–92.

Jones, A. M., Yin, J. and Harrison, R. M. (2008), 'The weekday–weekend difference and the estimation of the non-vehicle contributions to the urban increment of airborne particulate matter', Atmospheric Environment **42**(19), 4467–4479.

Kalogridis, A. (2014), Caractérisation des composés organiques volatils en région méditerranéenne, PhD thesis, Paris 11.

Karagulian, F., Belis, C. A., Dora, C. F. C., Prüss-Ustün, A. M., Bonjour, S., Adair-Rohani, H. and Amann, M. (2015), 'Contributions to cities' ambient particulate matter (pm): A systematic review of local source contributions at global level', Atmospheric environment **120**, 475–483.

Katul, G., Mahrt, L., Poggi, D. and Sanz, C. (2004), 'One- and two-equation models for canopy turbulence.', Bound.-Lay. Meteorol. **113**(1), 81–109.

Kikumoto, H. and Ooka, R. (2012), 'A numerical study of air pollutant dispersion with bimolecular chemical reactions in an urban street canyon using large-eddy simulation', Atmos. Environ. **54**, 456–464.

Kim, M. J. (2019), 'Sensitivity of nitrate aerosol production to vehicular emissions in an urban street', Atmosphere **10**(4), 212.

Kim, M. J., Park, R. J., Kim, J.-J., Park, S. H., Chang, L.-S., Lee, D.-G. and Choi, J.-Y. (2019), 'Computational fluid dynamics simulation of reactive fine particulate matter in a street canyon', Atmospheric environment **209**, 54–66.

Kim, Y., Lugon, L., Maison, A., Sarica, T., Roustan, Y., Valari, M., Zhang, Y., André, M. and Sartelet, K. (2022), 'MUNICH v2.0: a street-network model coupled with SSH-aerosol (v1.2) for multi-pollutant modelling', Geosci. Model Dev. **15**(19), 7371–7396.

Kim, Y., Sartelet, K. and Seigneur, C. (2011), 'Formation of secondary aerosols: impact of the gas-phase chemical mechanism', Atmos. Chem. Phys. **11**, 583–598.

Kim, Y., Wu, Y., Seigneur, C. and Roustan, Y. (2018a), 'Multi-scale modeling of urban air pollution: development and application of a Street-in-Grid model (v1. 0) by coupling MUNICH (v1. 0) and Polair3D (v1. 8.1).', Geosci. Model Dev. **11**(2), 611.

Kim, Y., Wu, Y., Seigneur, C. and Roustan, Y. (2018b), 'Multi-scale modeling of urban air pollution: development and application of a street-in-grid model (v1. 0) by coupling¡? xmltex\break?¿ munich (v1. 0) and polair3d (v1. 8.1)', Geoscientific Model Development **11**(2), 611–629.

Kinosian, J. (1982), 'Ozone-precursor relationships from EKMA diagrams', Environ. Sci. Technol. **16**(12), 880–883.

Klepeis, N. E., Nelson, W. C., Ott, W. R., Robinson, J. P., Tsang, A. M., Switzer, P., Behar, J. V., Hern, S. C. and Engelmann, W. H. (2001), 'The national human activity pattern survey (nhaps): a resource for assessing exposure to environmental pollutants', Journal of Exposure Science and Environmental Epidemiology **11**(3), 231–252.

Kumar, P., Fennell, P., Langley, D. and Britter, R. (2008), 'Pseudo-simultaneous measurements for the vertical variation of coarse, fine and ultrafine particles in an urban street canyon', Atmospheric Environment **42**(18), 4304–4319.

Kurppa, M., Hellsten, A., Roldin, P., Kokkola, H., Tonttila, J., Auvinen, M., Kent, C., Kumar, P., Maronga, B. and Järvi, L. (2018), 'Implementation of the sectional aerosol module salsa2. 0 into the palm model system 6.0: Model development and first evaluation', Geoscientific Model Development .

Kwak, K. and Baik, J. (2012), 'A CFD modeling study of the impacts of NO_x and VOC emissions on reactive pollutant dispersion in and above a street canyon.', Atmos. Environ. **46**, 71–80.

Kwak, K. and Baik, J. (2014), 'Diurnal variation of NOx and ozone exchange between a street canyon and the overlying air', Atmos. Environ. **86**, 120–128.

Kwak, K., Baik, J. and Lee, K. (2013), 'Dispersion and photochemical evolution of reactive pollutants in street canyons', Atmos. Environ. **70**, 98–107.

Lai, A. C. and Nazaroff, W. W. (2000), 'Modeling indoor particle deposition from turbulent flow onto smooth surfaces', Journal of aerosol science **31**(4), 463–476.

Landrigan, P., Fuller, R., Acosta, N., Adeyi, O., Arnold, R., Baldé, A., Bertollini, R., Bose-O'Reilly, S., Boufford, J., Breysse, P. et al. (2018), 'The Lancet Commission on pollution and health.', The Lancet. **391**(10119), 462–512.

Li, R., Zhou, R. and Zhang, J. (2018), 'Function of pm2. 5 in the pathogenesis of lung cancer and chronic airway inflammatory diseases', Oncology letters **15**(5), 7506–7514.

Lin, C., Wang, Y., Ooka, R., Flageul, C., Kim, Y., Kikumoto, H., Wang, Z. and Sartelet, K. (2022), 'Modelling of street-scale pollutant dispersion by coupled simulation of chemical reaction, aerosol dynamics, and CFD', Atmos. Chem. Phys. Discuss. pp. 1–32.

Lin, W., Xu, X., Ge, B. and Liu, X. (2011), 'Gaseous pollutants in beijing urban area during the heating period 2007–2008: variability, sources, meteorological, and chemical impacts', Atmospheric Chemistry and Physics **11**(15), 8157–8170.

Liu, C. and Leung, D. (2008), 'Numerical study on the ozone formation inside street canyons using a chemistry box model', J. Environ. Sci. **20**(7), 832–837.

Liu, K., Hua, S. and Song, L. (2022), 'Pm2. 5 exposure and asthma development: the key role of oxidative stress', Oxidative Medicine and Cellular Longevity **2022**.

Liu, S., Li, R., Wild, R., Warneke, C., De Gouw, J., Brown, S., Miller, S., Luongo, J., Jimenez, J. and Ziemann, P. (2016), 'Contribution of human-related sources to indoor volatile organic compounds in a university classroom', Indoor Air **26**(6), 925–938.

Lo, K. and Ngan, K. (2015), 'Characterising the pollutant ventilation characteristics of street canyons using the tracer age and age spectrum', Atmospheric Environment **122**, 611–621.

Lo, K. and Ngan, K. (2017), 'Characterizing ventilation and exposure in street canyons using lagrangian particles', Journal of Applied Meteorology and Climatology **56**(5), 1177–1194.

Loomis, D., Grosse, Y., Lauby-Secretan, B., El Ghissassi, F., Bouvard, V., Benbrahim-Tallaa, L., Guha, N., Baan, R., Mattock, H. and Straif, K. (2013), 'The carcinogenicity of outdoor air pollution', Lancet Oncology **14**(13), 1262.

Lovett, G. M., Tear, T. H., Evers, D. C., Findlay, S. E., Cosby, B. J., Dunscomb, J. K., Driscoll, C. T. and Weathers, K. C. (2009), 'Effects of air pollution on ecosystems and biological diversity in the eastern united states', Annals of the New York Academy of Sciences **1162**(1), 99–135.

Lugon, L., Kim, Y., Vigneron, J., Chrétien, O., André, M., André, J., Moukhtar, S., Redaelli, M. and Sartelet, K. (2022), 'Effect of vehicle fleet composition and mobility on outdoor population exposure: A street resolution analysis in Paris', Atmos. Pol. Res. **13**(5), 101365.

Lugon, L., Sartelet, K., Kim, Y., Vigneron, J. and Chrétien, O. (2020a), 'Nonstationary modeling of no 2, no and no x in paris using the street-in-grid model: coupling local and regional scales with a two-way dynamic approach', Atmospheric Chemistry and Physics **20**(13), 7717–7740.

Lugon, L., Sartelet, K., Kim, Y., Vigneron, J. and Chrétien, O. (2020b), 'Nonstationary modeling of NO_2, NO and NO_x in Paris using the Street-in-Grid model: coupling local and regional scales with a two-way dynamic approach.', Atmos. Chem. Phys. **20**(13), 7717–7740.

Lugon, L., Sartelet, K., Kim, Y., Vigneron, J. and Chrétien, O. (2021b), 'Simulation of primary and secondary particles in the streets of paris using munich', Faraday Discussions **226**, 432–456.

Lugon, L., Vigneron, J., Debert, C., Chrétien, O. and Sartelet, K. (2021a), 'Black carbon modeling in urban areas: investigating the influence of resuspension and non-exhaust emissions in streets using the street-in-grid model for inert particles (sing-inert)', Geoscientific Model Development **14**(11), 7001–7019.

Mailler, S., Menut, L., Khvorostyanov, D., Valari, M., Couvidat, F., Siour, G., Turquety, S., Briant, R., Tuccella, P., Bessagnet, B., Colette, A., Létinois, L., Markakis, K. and Meleux, F. (2017),

'CHIMERE-2017: from urban to hemispheric chemistry-transport modeling', Geosci. Model Dev. **10**, 2397–2423.

Maison, A., Flageul, C., Carissimo, B., Tuzet, A., Wang, Y. and Sartelet, K. (2022), 'Parameterizing the aerodynamic effect of trees in street canyons for the street-network model MUNICH using the CFD model Code_Saturne.', Atmos. Chem. Phys. **22**, 9369–9388.

Maison, A., Flageul, C., Carissimo, B., Wang, Y., Tuzet, A. and Sartelet, K. (2022), 'Parameterizing the aerodynamic effect of trees in street canyons for the street network model munich using the cfd model code_saturne', Atmospheric Chemistry and Physics **22**(14), 9369–9388.

Mallet, V., Quélo, D., Sportisse, B., Ahmed de Biasi, M., Debry, E., Korsakissok, I., Wu, L., Roustan, Y., Sartelet, K., Tombette, M. et al. (2007), 'The air quality modeling system polyphemus', Atmospheric Chemistry and Physics **7**(20), 5479–5487.

Markku, K. (2015), 'China's choking cocktail', Nature. **526**, 497–499.

Menut, L., Bessagnet, B., Khvorostyanov, D., Beekmann, M., Blond, N., Colette, A., Coll, I., Curci, G., Foret, G., Hodzic, A. et al. (2013), 'Chimere 2013: a model for regional atmospheric composition modelling', Geoscientific model development **6**(4), 981–1028.

Milliez, M. and Carissimo, B. (2007), 'Numerical simulations of pollutant dispersion in an idealized urban area, for different meteorological conditions', Bound.-Lay. Meteorol. **122**(2), 321–342.

Milner, J., Shrubsole, C., Das, P., Jones, B., Ridley, I., Chalabi, Z., Hamilton, I., Armstrong, B., Davies, M. and Wilkinson, P. (2014), 'Home energy efficiency and radon related risk of lung cancer: modelling study', Bmj **348**.

Muilwijk, C., Schrijvers, P., Wuerz, S. and Kenjereš, S. (2016), 'Simulations of photochemical smog formation in complex urban areas', Atmospheric Environment **147**, 470–484.

Naeim, F. (2001), 'Earthquake excitation and response of buildings', Encyclopedia of Vibration pp. 439–461.

Nazaroff, W. W. and Cass, G. R. (1986), 'Mathematical modeling of chemically reactive pollutants in indoor air', Environmental Science and Technology **20**(9), 924–934.

Nero, A. V. (1988), 'Controlling indoor air pollution', Scientific American **258**(5), 42–49.

Ning, Z., Chan, K. L., Wong, K., Westerdahl, D., Močnik, G., Zhou, J. and Cheung, C. S. (2013), 'Black carbon mass size distributions of diesel exhaust and urban aerosols measured using differential mobility analyzer in tandem with aethalometer', Atmospheric Environment **80**, 31–40.

Niroomand, N., Bach, C. and Elser, M. (2021), 'Vehicle dimensions based passenger car classification using fuzzy and non-fuzzy clustering methods', Transp. Res. Rec. **2675**(10), 184–194.

Nowak, D. (1996), 'Estimating leaf area and leaf biomass of open-grown deciduous urban trees.', Forest Sci. **42**(4), 504–507.

Nowak, D., Crane, D. and Stevens, J. (2006), 'Air pollution removal by urban trees and shrubs in the United States', Urban For Urban Green. **4**(3-4), 115–123.

Nowak, D., Hirabayashi, S., Bodine, A. and Hoehn, R. (2013), 'Modeled $PM_{2.5}$ removal by trees in ten US cities and associated health effects', Environ. Pollut. **178**, 395–402.

OpenFOAM (2022), 'Openfoam user guide', Available at `https://www.openfoam.com/` (2022/12/01).

Organization, W. H. et al. (2018), Air pollution and child health: prescribing clean air: summary, Technical report, World Health Organization.

Osseiran, N. and Lindmeier, C. (2018), '9 out of 10 people worldwide breathe polluted air, but more countries are taking action', Available at `https://www.who.int/news/item/02-05-2018-9-out-of-10-people-worldwide-breathe-polluted-air-but-more-countries-are-taking-action` (2018/05/02).

Owen, S., Boissard, C. and Hewitt, C. (2001), 'Volatile organic compounds (VOCs) emitted from 40 Mediterranean plant species:: VOC speciation and extrapolation to habitat scale', Atmos. Environ. **35**(32), 5393–3409.

Parente, A., Gorlé, C., Van Beeck, J. and Benocci, C. (2011), 'Improved k–ε model and wall function formulation for the rans simulation of abl flows', Journal of wind engineering and industrial aerodynamics **99**(4), 267–278.

Parungo, F., Nagamoto, C. and Maddl, R. (1987), 'A study of the mechanisms of acid rain formation', Journal of Atmospheric Sciences **44**(21), 3162–3174.

Philip, S., Martin, R. V., van Donkelaar, A., Lo, J. W.-H., Wang, Y., Chen, D., Zhang, L., Kasibhatla, P. S., Wang, S., Zhang, Q. et al. (2014), 'Global chemical composition of ambient fine particulate matter for exposure assessment', Environmental science and technology **48**(22), 13060–13068.

Pugh, T., MacKenzie, A., Whyatt, J. and Hewitt, C. (2012), 'Effectiveness of green infrastructure for improvement of air quality in urban street canyons', Environ. Sci. Technol. **46**(14), 7692–7699.

Qian, Y., Chakraborty, T., Li, J., Li, D., He, C., Sarangi, C., Chen, F., Yang, X. and Leung, L. R. (2022), 'Urbanization impact on regional climate and extreme weather: Current understanding, uncertainties, and future research directions', Advances in Atmospheric Sciences **39**(6), 819–860.

Qiao, X., Xiao, W., Jaffe, D., Kota, S. H., Ying, Q. and Tang, Y. (2015), 'Atmospheric wet deposition of sulfur and nitrogen in jiuzhaigou national nature reserve, sichuan province, china', Science of the Total Environment **511**, 28–36.

Rai, P. K. (2016), 'Impacts of particulate matter pollution on plants: Implications for environmental biomonitoring', Ecotoxicology and environmental safety **129**, 120–136.

Rao, M. and George, L. A. (2014), Using the no2/nox ratio to understand the spatial heterogeneity of secondary pollutant formation capacity in urban atmospheres, in 'AGU Fall Meeting Abstracts', Vol. 2014, pp. A33F–3265.

Reddington, C. L., McMeeking, G., Mann, G. W., Coe, H., Frontoso, M. G., Liu, D., Flynn, M., Spracklen, D. V. and Carslaw, K. S. (2013), 'The mass and number size distributions of black carbon aerosol over Europe', Atmospheric Chemistry and Physics **13**(9), 4917–4939.

Ren, Y., Ge, Y., Ma, D., Song, X., Shi, Y., Pan, K., Qu, Z., Guo, P., Han, W. and Chang, J. (2017), 'Enhancing plant diversity and mitigating BVOC emissions of urban green spaces through the introduction of ornamental tree species', Urban For Urban Green. **27**, 305–313.

Sanz, C. (2003), 'A note on k-ε modelling of vegetation canopy air-flows.', Bound.-Lay. Meteorol. **108**(1), 191–197.

Sartelet, K., Couvidat, F., Seigneur, C. and Roustan, Y. (2012), 'Impact of biogenic emissions on air quality over Europe and North America.', Atmos. Environ. **53**, 131–141.

Sartelet, K., Couvidat, F., Wang, Z., Flageul, C. and Kim, Y. (2020), 'Ssh-aerosol v1. 1: A modular box model to simulate the evolution of primary and secondary aerosols', Atmosphere **11**(5), 525.

Sartelet, K., Debry, E., Fahey, K., Roustan, Y., Tombette, M. and Sportisse, B. (2007), 'Simulation of aerosols and gas-phase species over europe with the polyphemus system: Part i—model-to-data comparison for 2001', Atmospheric Environment **41**(29), 6116–6131.

Sartelet, K., Kim, Y., Couvidat, F., Merkel, M., Petäjä, T., Sciare, J. and Wiedensohler, A. (2022), 'Influence of emission size distribution and nucleation on number concentrations over greater paris', Atmospheric Chemistry and Physics **22**(13), 8579–8596.

Sartelet, K., Zhu, S., Moukhtar, S., André, M., André, J., Gros, V., Favez, O., Brasseur, A. and Redaelli, M. (2018), 'Emission of intermediate, semi and low volatile organic compounds from traffic and their impact on secondary organic aerosol concentrations over greater paris', Atmospheric Environment **180**, 126–137.

Sarwar, G., Corsi, R., Kimura, Y., Allen, D. and Weschler, C. J. (2002), 'Hydroxyl radicals in indoor environments', Atmospheric Environment **36**(24), 3973–3988.

Satish, U., Mendell, M. J., Shekhar, K., Hotchi, T., Sullivan, D., Streufert, S. and Fisk, W. J. (2012), 'Is co2 an indoor pollutant? direct effects of low-to-moderate co2 concentrations on human decision-making performance', Environmental health perspectives **120**(12), 1671–1677.

Schmidt, M. J., Pankavich, S. D., Navarre-Sitchler, A. and Benson, D. A. (2019), 'A lagrangian method for reactive transport with solid/aqueous chemical phase interaction', Journal of Computational Physics: X **2**, 100021.

Schuster, P. F., Reddy, M. M. and Sherwood, S. I. (1994), 'Effects of acid rain and sulfur dioxide on marble dissolution', Materials performance **33**(1), 76–80.

Seigneur, C. (2019), Air pollution: concepts, theory, and applications.

Seinfeld, J. H. and Pandis, S. N. (2016), Atmospheric chemistry and physics: from air pollution to climate change, John Wiley and Sons.

Selmi, W., Weber, C., Rivière, E., Blond, N., Mehdi, L. and Nowak, D. (2016), 'Air pollution removal by trees in public green spaces in Strasbourg city, France.', Urban For Urban Green. **17**, 192–201.

Sesana, E., Gagnon, A. S., Ciantelli, C., Cassar, J. and Hughes, J. J. (2021), 'Climate change impacts on cultural heritage: A literature review', Wiley Interdisciplinary Reviews: Climate Change **12**(4), e710.

Sharma, N., Gulia, S., Dhyani, R. and Singh, A. (2013), 'Performance evaluation of caline 4 dispersion model for an urban highway corridor in delhi'.

Shin, S.-H. and Jo, W.-K. (2013), 'Longitudinal variations in indoor voc concentrations after moving into new apartments and indoor source characterization', Environmental Science and Pollution Research **20**, 3696–3707.

Sini, J., Anquetin, S. and Mestayer, P. (1996), 'Pollutant dispersion and thermal effects in urban street canyons', Atmos. Environ. **30**(15), 2659–2677.

Slinn, W. (1982), 'Predictions for particle deposition to vegetative canopies', Atmospheric Environment (1967) **16**(7), 1785–1794.

Solazzo, E., Cai, X. and Vardoulakis, S. (2008), 'Modelling wind flow and vehicle-induced turbulence in urban streets', Atmos. Environ. **42**(20), 4918–4931.

Song, C., Huang, G., Zhang, B., Yin, B. and Lu, H. (2019), 'Modeling air pollution transmission behavior as complex network and mining key monitoring station', IEEE Access **7**, 121245–121254.

Soulhac, L., Salizzoni, P., Cierco, F.-X. and Perkins, R. (2011), 'The model sirane for atmospheric urban pollutant dispersion; part i, presentation of the model', Atmospheric environment **45**(39), 7379–7395.

Speizer, F., Ferris, B., Bishop, Y. and Spengler, J. (1980), 'Respiratory disease rates and pulmonary function in children associated with NO2 exposure.', Am. Rev. Respir. Dis. **121**(1), 3–10.

Sportisse, B. (2000), 'An analysis of operator splitting techniques in the stiff case', Journal of computational physics **161**(1), 140–168.

Srikanth, P., Sudharsanam, S. and Steinberg, R. (2008), 'Bio-aerosols in indoor environment: composition, health effects and analysis', Indian journal of medical microbiology **26**(4), 302–312.

Srivastava, A. and Rao, B. P. S. (2011), 'Urban air pollution modeling', Air Quality-Models and Applications **364**.

Stocker, J., Hood, C., Carruthers, D. and McHugh, C. (2012), 'Adms-urban: developments in modelling dispersion from the city scale to the local scale', International Journal of Environment and Pollution **50**(1-4), 308–316.

Stockie, J. M. (2011), 'The mathematics of atmospheric dispersion modeling', Siam Review **53**(2), 349–372.

Suarez-Bertoa, R. and Astorga, C. (2018), 'Impact of cold temperature on euro 6 passenger car emissions', Environmental pollution **234**, 318–329.

Suarez-Bertoa, R., Mendoza-Villafuerte, P., Riccobono, F., Vojtisek, M., Pechout, M., Perujo, A. and Astorga, C. (2017), 'On-road measurement of nh3 emissions from gasoline and diesel passenger cars during real world driving conditions', Atmospheric Environment **166**, 488–497.

Sun, K., Tao, L., Miller, D. J., Pan, D., Golston, L. M., Zondlo, M. A., Griffin, R. J., Wallace, H. W., Leong, Y. J., Yang, M. M. et al. (2017), 'Vehicle emissions as an important urban ammonia source in the united states and china', Environmental Science and Technology **51**(4), 2472–2481.

Sung, J. C., Pulliam, B. L. and Edwards, D. A. (2007), 'Nanoparticles for drug delivery to the lungs', Trends in biotechnology **25**(12), 563–570.

Tao, A., Liang, Q., Kuai, P. and Ding, T. (2021), 'The influence of urban sprawl on air pollution and the mediating effect of vehicle ownership', Processes **9**(8), 1261.

Tecer, L. H., Alagha, O., Karaca, F., Tuncel, G. and Eldes, N. (2008), 'Particulate matter (pm2. 5, pm10-2.5, and pm10) and children's hospital admissions for asthma and respiratory diseases: a bidirectional case-crossover study', Journal of Toxicology and Environmental Health, Part A **71**(8), 512–520.

Thorpe, A. and Harrison, R. (2008), 'Sources and properties of non-exhaust particulate matter from road traffic: a review', Sci. Total Environ. **400**(1-3), 270–282.

Tominaga, Y. and Stathopoulos, T. (2007), 'Turbulent schmidt numbers for cfd analysis with various types of flowfield', Atmospheric Environment **41**(37), 8091–8099.

Tominaga, Y. and Stathopoulos, T. (2013), 'Cfd simulation of near-field pollutant dispersion in the urban environment: A review of current modeling techniques', Atmospheric Environment **79**, 716–730.

Tong, Z., Chen, Y., Malkawi, A., Adamkiewicz, G. and Spengler, J. D. (2016), 'Quantifying the impact of traffic-related air pollution on the indoor air quality of a naturally ventilated building', Environment international **89**, 138–146.

UN-Habitat (2022), World Cities Report 2022: Envisaging the Future of Cities, 978-92-1-133395-4, United Nations Human Settlements Programme, P.O. Box 30030, Nairobi, Kenya.

Uzu, G., Sobanska, S., Sarret, G., Sauvain, J.-J., Pradere, P. and Dumat, C. (2011), 'Characterization of lead-recycling facility emissions at various workplaces: major insights for sanitary risks assessment', Journal of Hazardous Materials **186**(2-3), 1018–1027.

Van Hooff, T. and Blocken, B. (2010), 'Coupled urban wind flow and indoor natural ventilation modelling on a high-resolution grid: A case study for the amsterdam arena stadium', Environmental Modelling and Software **25**(1), 51–65.

Vardoulakis, S., Fisher, B., Pericleous, K. and Gonzalez-Flesca, N. (2003), 'Modelling air quality in street canyons: a review.', Atmos. Environ. **37**(2), 155–182.

Ville de Paris (2020), 'Les arbres', Open Data Base .

Vincent, D. (2019), 'Airborne particulate matter and their health effects', Encyclopédie de l'environnement pp. 1–11.

Vos, P., Maiheu, B., Vankerkom, J. and Janssen, S. (2013), 'Improving local air quality in cities: to tree or not to tree?', Environ. Pollut. **183**, 113–122.

Wang, J., Hu, Z., Chen, Y., Chen, Z. and Xu, S. (2013), 'Contamination characteristics and possible sources of pm10 and pm2. 5 in different functional areas of shanghai, china', Atmospheric Environment **68**, 221–229.

Wang, Z., Bai, Y. and Zhang, S. (2003), 'A biogenic volatile organic compounds emission inventory for Beijing.', Atmos. Environ. **37**(27), 3771–3782.

Weinmayr, G., Romeo, E., De Sario, M., Weiland, S. and Forastiere, F. (2010), 'Short-term effects of PM_{10} and NO_2 on respiratory health among children with asthma or asthma-like symptoms: a systematic review and meta-analysis.', Env. Health Persp. **118**(4), 449–457.

Wen, D., Lin, J., Zhang, L., Vet, R. and Moran, M. (2013), 'Modeling atmospheric ammonia and ammonium using a stochastic lagrangian air quality model (stilt-chem v0. 7)', Geoscientific Model Development **6**(2), 327–344.

Weschler, C. (2011), 'Chemistry in indoor environments: 20 years of research', Indoor Air **21**(3), 205–218.

Weschler, C. J. and Carslaw, N. (2018), 'Indoor chemistry', Environmental Science and Technology **52**(5), 2419–2428.

Weschler, C. J. and Shields, H. C. (1996), 'Production of the hydroxyl radical in indoor air', Environmental science and technology **30**(11), 3250–3258.

Wesely, M. (1989), 'Parameterization of surface resistances to gaseous dry deposition in regional-scale numerical models.', Atmos. Environ. **23**(6), 1293–1304.

Wesely, M. (2007), 'Parameterization of surface resistances to gaseous dry deposition in regional-scale numerical models', Atmospheric Environment **41**, 52–63.

WHO (2021), WHO global air quality guidelines: particulate matter (PM2.5 and PM10), O_3, NO_2, SO_2 and CO, World Health Organization.

Wickramasinghe, N., Hoyle, F. and Rabilizirov, R. (1989), 'Extraterrestrial particles and the greenhouse effect', Earth Moon and Planets **46**, 297–300.

Wiernga, J. (1993), 'Representative roughness parameters for homogeneous terrain', Bound.-Lay. Meteorol. **63**(4), 323–363.

Wu, L., Hang, J., Wang, X., Shao, M. and Gong, C. (2021), 'Apfoam 1.0: integrated computational fluid dynamics simulation of o 3–no x–volatile organic compound chemistry and pollutant dispersion in a typical street canyon', Geoscientific Model Development **14**(7), 4655–4681.

Yakhot, V., Orszag, S., Thangam, S., Gatski, T. and Speziale, C. (1992), 'Development of turbulence models for shear flows by a double expansion technique', Physics of Fluids A: Fluid Dynamics **4**(7), 1510–1520.

Yarwood, G., Rao, S., Yocke, M. and Whitten, G. (2005), 'Updates to the carbon bond chemical mechanism: Cb05, rep. rt-0400675'.

Yassin, M. F. (2013), 'Numerical modeling on air quality in an urban environment with changes of the aspect ratio and wind direction', Environmental Science and Pollution Research **20**, 3975–3988.

Yee, H. C. (1987), 'Construction of explicit and implicit symmetric tvd schemes and their applications', Journal of Computational physics **68**(1), 151–179.

Yuchi, W., Sbihi, H., Davies, H., Tamburic, L. and Brauer, M. (2020), 'Road proximity, air pollution, noise, green space and neurologic disease incidence: a population-based cohort study', Environ. Health. **19**(1), 1–15.

Zabalza, J., Ogulei, D., Elustondo, D., Santamaría, J., Alastuey, A., Querol, X. and Hopke, P. (2007), 'Study of urban atmospheric pollution in navarre (northern spain)', Environmental monitoring and assessment **134**, 137–151.

Zaidi, H., Dupont, E., Milliez, M., Musson-Genon, L. and Carissimo, B. (2013), 'Numerical simulations of the microscale heterogeneities of turbulence observed on a complex site.', Bound.-Lay. Meteorol. **147**(2), 237–259.

Zhang, K., Chen, G., Zhang, Y., Liu, S., Wang, X., Wang, B. and Hang, J. (2020), 'Integrated impacts of turbulent mixing and nox-o3 photochemistry on reactive pollutant dispersion and intake fraction in shallow and deep street canyons', Science of the Total Environment **712**, 135553.

Zhang, L., Brook, J. R. and Vet, R. (2003a), 'A revised parameterization for gaseous dry deposition in air-quality models', Atmospheric Chemistry and Physics **3**(6), 2067–2082.

Zhang, L., Brook, J. R. and Vet, R. (2003b), 'A revised parameterization for gaseous dry deposition in air-quality models', Atmospheric Chemistry and Physics **3**(6), 2067–2082.

Zhang, L., Gong, S., Padro, J. and Barrie, L. (2001), 'A size-segregated particle dry deposition scheme for an atmospheric aerosol module', Atmospheric environment **35**(3), 549–560.

Zhang, L., Moran, M. D., Makar, P. A., Brook, J. R. and Gong, S. (2002a), 'Modelling gaseous dry deposition in aurams: a unified regional air-quality modelling system', Atmospheric Environment **36**(3), 537–560.

Zhang, L., Moran, M., Makar, P., Brook, J. and Gong, S. (2002b), 'Modelling gaseous dry deposition in AURAMS: a unified regional air-quality modelling system.', Atmos. Environ. **36**(3), 537–560.

Zheng, S., Pozzer, A., Cao, C. and Lelieveld, J. (2015), 'Long-term (2001–2012) concentrations of fine particulate matter (pm 2.5) and the impact on human health in beijing, china', Atmospheric Chemistry and Physics **15**(10), 5715–5725.

Zhong, J., Cai, X. and Bloss, W. (2014), 'Modelling segregation effects of heterogeneous emissions on ozone levels in idealised urban street canyons: Using photochemical box models', Environ. Pollut. **188**, 132–143.

Zhou, Y., Liu, Y., Song, Y., Xie, J., Cui, X., Zhang, B., Shi, T., Yuan, J. and Chen, W. (2016), 'Short-term Effects of Outdoor Air Pollution on Lung Function among Female Non-smokers in China', Scientific Reports **6**, 34947.

Zifa, W., Chengming, P., Jiang, Z. et al. (2008), 'Iap progress in atmospheric environment modeling research', Chinese J Atmos Sci **32**(4), 987–995.

LIST OF PUBLICATIONS

Articles:

1. Lin C, Wang Y, Ooka R, Flageul C, Kim Y, Kikumoto H, Wang Z, and Sartelet K. Modeling of street-scale pollutant dispersion by coupled simulation of chemical reaction, aerosol dynamics, and CFD. Atmospheric Chemistry and Physics, 2023, 23(2), pp.1421-1436. DOI: 10.5194/acp-23-1421-2023.

2. Wang Y, Flageul C, Maison A, Carissimo B, and Sartelet K. Impact of trees on gas concentrations and condensables in a 2-D street canyon using CFD coupled to chemistry modeling. Environmental Pollution, 2023, 323: 121210. DOI: 10.1016/j.envpol.2023.121210.

3. Maison A, Flageul C, Carissimo B, Wang Y, Tuzet A, and Sartelet K. Parameterizing the aerodynamic effect of trees in street canyons for the street network model MUNICH using the CFD model Code_Saturne. Atmospheric Chemistry and Physics, 2022, 22(14), pp.9369-9388. DOI: 10.5194/acp-22-9369-2022.

Conferences:

1. 26th Annual George Mason University Conference on Atmospheric Transport and Dispersion Modeling. Presentation of the work: impact of trees on air quality in the street canyon

2. 21st International Conference On Harmonisation Within Atmospheric Dispersion Modelling For Regulatory Purposes. Abstract accepted and published online, with the site address presented: https://harmo.org/Conferences/Proceedings/_Aveiro/publishedSections/00511_163_h21-102-yunyi-wang.pdf